

AD-A039 812

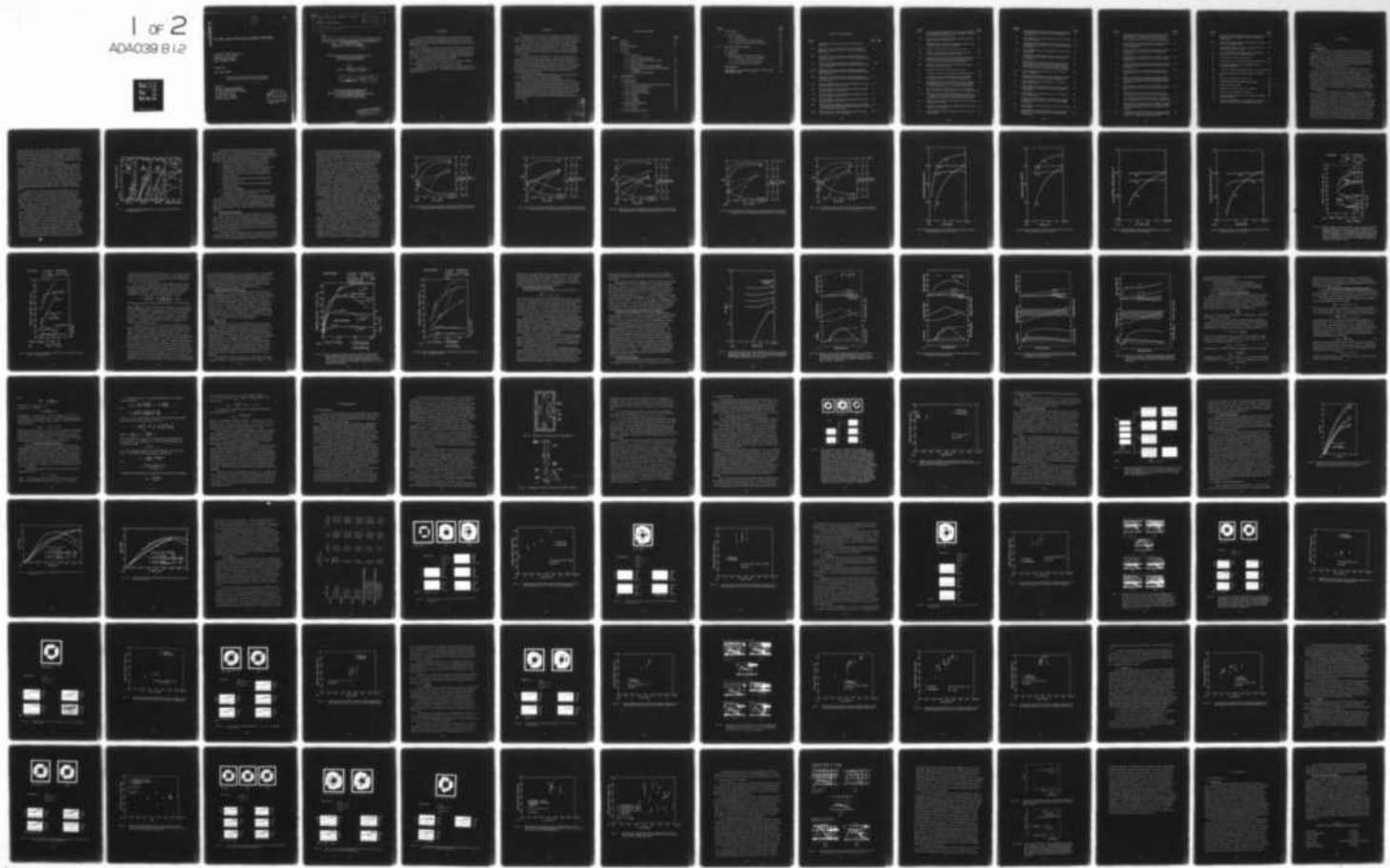
AVCO EVERETT RESEARCH LAB INC EVERETT MASS
HIGH SPECIFIC ENERGY PULSED ELECTRIC DISCHARGE LASER RESEARCH (U)
DEC 75 D H DOUGLAS-HAMILTON, R M FEINBERG

F/G 20/5
DAAH01-75-C-0503

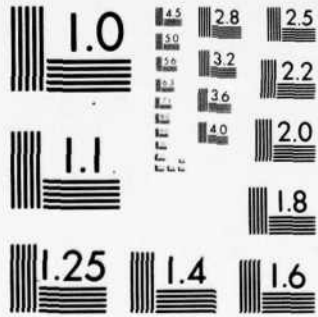
UNCLASSIFIED

NL

1 of 2
AD-A039 812



039 8



MICROCOPY RESOLUTION TEST CHART
NATIONAL BUREAU OF STANDARDS-1963-A

ADA 039812

①

J

HIGH SPECIFIC ENERGY PULSED ELECTRIC DISCHARGE LASER RESEARCH

Avco Everett Research Laboratory, Inc.
a Subsidiary of Avco Corporation
2385 Revere Beach Parkway
Everett, Massachusetts 02149

December 1975

Final Technical Report

APPROVED FOR PUBLIC RELEASE; DISTRIBUTION UNLIMITED

Prepared for
PHYSICAL SCIENCES DIRECTORATE
U.S. Army Missile Research, Development
and Engineering Laboratory
U.S. Army Missile Command
Redstone Arsenal, Al. 35809

DDC
RECEIVED
MAY 23 1977
A

⑩ D.H. / Douglas-Hamilton, J.P. / Raas
R.M. / Feinberg, O.K. / Zappa
R.S. / Howdet,

⑥
HIGH SPECIFIC ENERGY PULSED ELECTRIC DISCHARGE
LASER RESEARCH.

⑨ FINAL TECHNICAL REPORT.

AVCO EVERETT RESEARCH LABORATORY, INC.
a Subsidiary of Avco Corporation
Everett, Massachusetts 02149

⑮

Contract No. DAAH01-75-C-0503 *new*

⑪ December 1975

⑫ 132 p.

PHYSICAL SCIENCES DIRECTORATE
U. S. ARMY MISSILE RESEARCH,
DEVELOPMENT AND ENGINEERING LABORATORY
U. S. ARMY MISSILE COMMAND
Redstone Arsenal, Alabama 35809

DISTRIBUTION STATEMENT I
Approved for public release;
Distribution Unlimited

048450

7/B

FOREWORD

Avco Everett Research Laboratory, Inc. (AERL) of 2385 Revere Beach Parkway, Everett, Massachusetts prepared this report on High Specific Energy Pulsed Electric Discharge Laser Research under Contract DAAH01-75-C-0503.

The program was sponsored by the Physical Sciences Directorate and the Program Monitor was Mr. Charles Cason, Physical Sciences Directorate, U. S. Army Missile Research, Development and Engineering Laboratory, U. S. Army Missile Command, Redstone Arsenal, Alabama. Mr. R. M. Feinberg was the AERL Program Manager.

Principal coauthors of this report were D. H. Douglas-Hamilton, R. M. Feinberg, R. S. Lowder, J. P. Roos and O. L. Zappa.

Publication of this report does not constitute Army approval of the reports findings or conclusions. It is published only for the exchange and stimulation of ideas.

ABSTRACT

Theoretical and experimental investigations are presented of laser kinetics related to the use of combustion product gases in CO_2 laser systems. Several processes for producing the laser gas are also considered.

The sensitivity of laser performance to gas composition and to level of impurities is considered theoretically. The role of CO and the appropriate fractions of H_2 and H_2O are examined. Maximum allowable amounts of impurities (O_2 , hydrocarbons, water vapor and particulates) are determined.

The laser output was measured for a variety of gases related to possible combustion product gas mixtures. Some actual combustion product mixtures were tested as well. The measured laser performance generally agreed well with prediction, with the exception of CO-containing gases where a 15 - 25 percent discrepancy for 12 percent CO was found. No unexpected problems due to impurities were found when using the actual combustion product gas.

The generation method and gas properties of the combustion product gas generated at Avco-Lycoming are presented.

Various gas turbine cycles for generating the laser gas were studied. Three gas production systems are considered, open- and closed-cycle operation using stored gas (the gas being generated prior to a laser run) and open-cycle operation using on-line gas generation (the laser gas being generated during the laser run). The gas storage, open-cycle system has the disadvantage of a limited duty cycle (here taken to be 50:1), but is otherwise found to be far superior in terms of weight and volume, as well as cost.

File Section	<input checked="" type="checkbox"/>
Ext Section	<input type="checkbox"/>
Publication	<input type="checkbox"/>
BY	
DISTRIBUTION AVAILABILITY CODES	
Dist. Avail. and/or SPECIAL	
A	

TABLE OF CONTENTS

<u>Section</u>		<u>Page</u>
	Foreword	ii
	Abstract	iii
	List of Illustrations	vi
1.0	KINETICS	1
1.1	Theory	1
1.1.1	Introduction	
1.1.2	Effect of Carbon Monoxide	4
1.1.3	Effect of Hydrogen and Water Vapor	18
1.1.4	Effect of H ₂ O	18
1.1.5	Effect of Hydrocarbons and Oxygen	21
1.1.6	Predicted Laser Performance with E-Beam Variations	22
1.1.7	Acceptable Level of Smoke	22
2.0	EXPERIMENTAL	33
2.1	Introduction	33
2.2	Measurements	37
2.2.1	Laser Performance Using He:N ₂ :CO ₂ (3:2:1)	37
2.2.2	P-Line Measurements	40
2.2.3	Gain Measurements	42
2.3	Laser Output Measurements	42
2.3.1	Group I	46
2.3.2	Group II	52
2.3.3	Group III	62
2.4	Combustion Product Gas	69
2.4.1	Group IV	69
2.4.2	Group V	71
2.5	Summary and Conclusions	79

<u>Section</u>	<u>Page</u>
3.0 GAS SYSTEM	84
3.1 Gas Production	84
3.1.1 Introduction	84
3.1.2 Gas Generation and Processing	85
3.1.3 Combustion Laser Gas Composition	90
4.0 GAS PRODUCTION SYSTEMS	95
4.1 Introduction	95
4.2 Summary	96
4.3 Field Application of Each Cycle System	99
4.3.1 Stored Gas, Closed-Cycle System	99
4.3.2 Stored Gas, Open-Cycle System	103
4.3.3 On-Line, Open-Cycle System	106
REFERENCES	111
APPENDIX A - THE STABLE VESSEL - A NEW TYPE PRESSURE VESSEL	112

LIST OF ILLUSTRATIONS

<u>Figure</u>		<u>Page</u>
1	Equilibrium Combustion Products for Hydrocarbon Air Flame	3
2(a)	Fractional Energy Pumped into Vibrational Modes by Electrons, as Function of E/N, in the Gas N ₂ :CO ₂ :H ₂ (8.2:1:0:0.09)	6
2(b)	Fractional Energy Pumped into Vibrational Modes by Electrons, as Function of E/N, in the Gas N ₂ :CO ₂ :CO:H ₂ (8.2:1:0.6:0.18)	7
2(c)	Fractional Energy Pumped into Vibrational Modes by Electrons, as Function of E/N, in the Gas N ₂ :CO ₂ :CO:H ₂ (8.2:1:1.2:0.18)	8
2(d)	Fractional Energy Pumped into Vibrational Modes by Electrons, as Function of E/N, in the Gas N ₂ :CO ₂ :CO:H ₂ (16.4:1:0.36:0)	9
2(e)	Fractional Energy Pumped into Vibrational Modes by Electrons, as Function of E/N, in the Gas N ₂ :CO ₂ :CO:H ₂ (4.1:1:0:0.09)	10
3(a)	Electron Impact Vibrational Excitation Rates in the Gas N ₂ :CO ₂ :CO:H ₂ (8.2:1:0.6:0.18)	11
3(b)	Electron Impact Vibrational Excitation Rates in the Gas N ₂ :CO ₂ :CO:H ₂ (8.2:1:1.2:0.18)	12
3(c)	Electron Impact Vibrational Excitation Rates in the Gas N ₂ :CO ₂ :CO:H ₂ (16.4:1:0:0.36)	13
3(d)	Electron Impact Vibrational Excitation Rates in the Gas N ₂ :CO ₂ :CO:H ₂ (4.1:1:0:0.09)	14
4(a)	Effect on Specific Output and Pulse Duration of Altering [CO ₂] and [CO] Relative to the Standard Fraction [CO ₂] 0 for the Standard Gas Mixture	15
4(b)	Effect on Specific Output and Pulse Duration of [CO ₂] and [CO] at n _e = 3 x 10 ¹³ and 10 ¹⁴	16

<u>Figure</u>		<u>Page</u>
5(a)	Effect on Specific Output and Pulse Duration of Altering the Deactivating Components $[H_2]$ and $[H_2O]$, Relative to the Standard Fraction of CO_2	19
5(b)	Effect on Specific Output and Pulse Duration of Deactivants for $n_e = 3 \times 10^{13}$ and 10^{14}	20
6	Attachment Coefficient β for the Standard Gas to which a Fraction ψ_{O_2} of O_2 has been added.	23
7(a)	Kinetics of CO_2 Laser for Ramped Power Input	24
7(b)	Kinetics of CO_2 Laser for Ramped Power Input with 6-Percent CO Present in the Gas Mixture	25
8(a)	Kinetics of CO_2 Laser System Using Sinusoidal Power Input, for Example by Varying the Electron Beam so as to Produce the Sustainer Current Indicated	26
8(b)	Kinetics of CO_2 Laser Using Sinusoidal Power Input with 6-Percent CO Present	27
9	Schematic of Cold Cavity Flow and Geometry	35
10	Schematic of Optical Arrangement and Mask Location	35
11	Burn Patterns and Laser Output for the Gas Mixture $He:N_2:CO_2:CO:H_2$ (3:2:1:0:0) at Low Temperature	38
12	Experimental and Predicted Values of Specific Output Plotted Against Electric Field Per Unit Density (E/N) for $He:N_2:CO_2:CO:H_2$ (3:2:1:0:0) at Low Temperature	39
13	Spectrum Analyzer Measurements of Laser Output at $T_{go} = 215^\circ K$, for a Pulse Duration of 5, 10, 25 and $50 \mu sec$	41
14	Measured and Predicted Small Signal Gains $g(cm^{-1})$ as a Function of Time During the Discharge for $He:N_2:CO_2$ at Initial Gas Temperature and at Room Temperature	43
15	Measured and Predicted Small Signal Gains for $N_2:CO_2:CO:H_2$ (8:33:1:0:0.19)	44
16	Measured and Predicted Small Signal Gains for $N_2:CO_2:CO:H_2$ (7:8:1:0.57:0.19)	45
17	Laser Output for $N_2:CO_2:CO:H_2$ (3.67:1:0:0.19) at Low Temperature	48

<u>Figure</u>		<u>Page</u>
18	Experimental and Predicted Values of Specific Output vs E/N for N ₂ :CO ₂ :CO:H ₂ (3.67:1:0:0.19) at Low Temperature	49
19	Laser Output for N ₂ :CO ₂ :CO:H ₂ (7.76:1:0.571:0.095) at Low Temperature	50
20	Experimental and Predicted Values of Specific Output vs E/N for N ₂ :CO ₂ :CO:H ₂ (7.76:1:0.571:0.095) at Low Temperature	51
21	Laser Output for N ₂ :CO ₂ :CO:H ₂ (8.22:1:0:0.19) at Low Temperature	53
22	Experimental and Predicted Values of Specific Output vs E/N for N ₂ :CO ₂ :CO:H ₂ (8.33:1:0:0.19) at Low Temperature	54
23	Measured and Predicted Flux Onset Times and Flux Time Histories for Representative Cases of the Gas Mixtures N ₂ :CO ₂ :CO:H ₂ (3.67:1:0:0.095), (7.76:1:0.571:0.059), and (8.33:1:0:0.19) at Low Temperature	55
24	Laser Output for N ₂ :CO ₂ :CO:H ₂ (8.33:1:0:0.19) at Room Temperature	56
25	Experimental and Predicted Values of Specific Output vs E/N for N ₂ :CO ₂ :CO:H ₂ at Room Temperature	57
26	Laser Output for N ₂ :CO ₂ :CO:H ₂ (16.4:1:0:0.36) at Room Temperature	58
27	Experimental and Predicted Values of Specific Output vs E/N for N ₂ :CO ₂ :CO:H ₂ (16.4:1:0:0.36) at Room Temperature	59
28	Laser Output for N ₂ :CO ₂ :CO:H ₂ (7.2:1:1.14:0.19) at Room Temperature	60
29	Experimental and Predicted Values of Specific Output vs E/N for N ₂ :CO ₂ :CO:H ₂ (7.2:1:1.14:0.19) at Room Temperature	61
30	Laser Output for H ₂ :CO ₂ :CO:H ₂ (8.33:1:0:0.19) at Low Temperature	63
31	Experimental and Predicted Values of Specific Output vs E/N for N ₂ :CO ₂ :CO:H ₂ (8.33:1:0:0.19) at Room Temperature	64

<u>Figure</u>		<u>Page</u>
32	Measured and Predicted Flux Onset Times and Flux Time Histories for Representative Cases of the Gas Mixtures $N_2: CO_2: CO: H_2$ (8.33: 1: 0: 0.19), (16.4: 1: 0.36), and (7.19: 1: 1.40: 0.19) at Room Temperature	65
33	Experimental and Predicted Values of Specific Output vs E/N for $N_2: CO_2: CO: H_2$ (8.33: 1: 0: 0.095) at Room Temperature	66
34	Experimental and Predicted Values of Specific Output vs E/N for $N_2: CO_2: H_2$ (8.33: 1: 0: 0.19) at Room Temperature	67
35	Experimental and Predicted Values of Specific Output vs E/N for $N_2: CO_2: CO: H_2$ (8.33: 1: 0: 0.314) at Room Temperature	68
36	Experimental and Predicted Values of Specific Output vs E/N for $H_2: CO_2: CO: H_2$ (16.4: 1: 0: 0.36) at Room Temperature	70
37	Laser Output for Actual Combustion Product Gas $N_2: CO_2: CO: H_2$ (6.2: 1: 0.2: 0.11) at Room Temperature	72
38	Experiment and Predicted Values of Specific Output vs E/N for Actual and Simulated Combustion Product Gas $N_2: CO_2: CO: H_2$ (6.2: 1: 0.2: 0.11) at Room Temperature	73
39	Laser Output for Simulated Combustion Product Gas $N_2: CO_2: CO: H_2$ (6.2: 1: 0.2: 0.11) at Room Temperature	74
40	Laser Output for Actual Combustion Product Gas $N_2: CO_2: CO: H_2$ (6.2: 1: 0.2: 0.11) at low Temperature	75
41	Laser Output for Simulated Combustion Product Gas $N_2: CO_2: CO: H_2$ (6.2: 1: 0.2: 0.11) at Low Temperature	76
42	Experimental and Predicted Values of Specific Output vs E/N for Actual and Simulated Combustion Product Gas $N_2: CO_2: CO: H_2$ (6.2: 1: 0.2: 0.11) at Low Temperature	77
43	Experimental and Predicted Values of Specific Output vs E/N for Combustion Product Gas $N_2: CO_2: CO: H_2$ (6.2: 1: 0.2: 0.098) at T_{g_0} 215°K and 300°K	78

<u>Figure</u>		<u>Page</u>
44	Measured and Predicted Onset Times and Flux Time Histories for Representative Cases of Combustion Product Gas	80
45a	Variation in Output Relative to Prediction as a Function of CO ₂ and CO content	82
45b	Plot of Specific Output vs Gas Composition for Constant E/N, T _{g0} and n _e values	82
46	Lycoming Gas Generator Schematic of Combustor, Water-Cooled Tube and Sampling Probe	87
47	Gas Generator for Avco Everett Lab	88
48	Combustion Gas Composition Variation with Fuel Flow	93
49	Simplified Schematics of Gas Turbine Type Gas Generation Systems	97
50	Variation in Total Gas Systems Weight, 25 lb/sec FSS	100
51	Variation in Operational System Volume, 25 lb/sec FSS	101
52	Schematic-Stored Gas, Closed Cycle	102
53	Schematic-Stored Gas, Open-Cycle System	105
54	Stored Gas, Open Cycle	108
55	Schematic, On-Line, Open-Cycle System	109
A1	Pressure Vessel Stability Criterion	114
A2	Dimension Identification for Derivation of Tie-Plate Force Formulas	115
A3	Dimension Identification for Derivation of Tie-Plate and Vessel Wall Thickness, Weight and Volume	115

1.0 KINETICS

1.1 THEORY

1.1.1 Introduction

The most efficient room-temperature laser that has been produced to date is the CO₂ laser, more specifically the electron-beam sustainer excited CO₂ laser. Electrical efficiencies above 20 percent are obtained routinely in the laboratory, and considerably higher efficiencies are possible. The large-scale high pressure discharges produced using external ionization lend themselves to constructing extremely large laser devices, a possibility of considerable military interest.

One of the most curious, or at least convenient, facts about the CO₂ laser is the facility with which the upper excited state of the CO₂ molecule can transfer vibrational energy with the N₂ molecule. This immediately leads to the use of N₂ as a medium for pumping the CO₂ molecule, since N₂ possesses an unusually high cross-section for electron impact vibrational excitation, and can consequently extract energy from the discharge electron gas and rapidly transfer it to the laser upper level in CO₂. Kinetically three to five N₂ molecules per CO₂ molecule provide optimum transfer pumping.

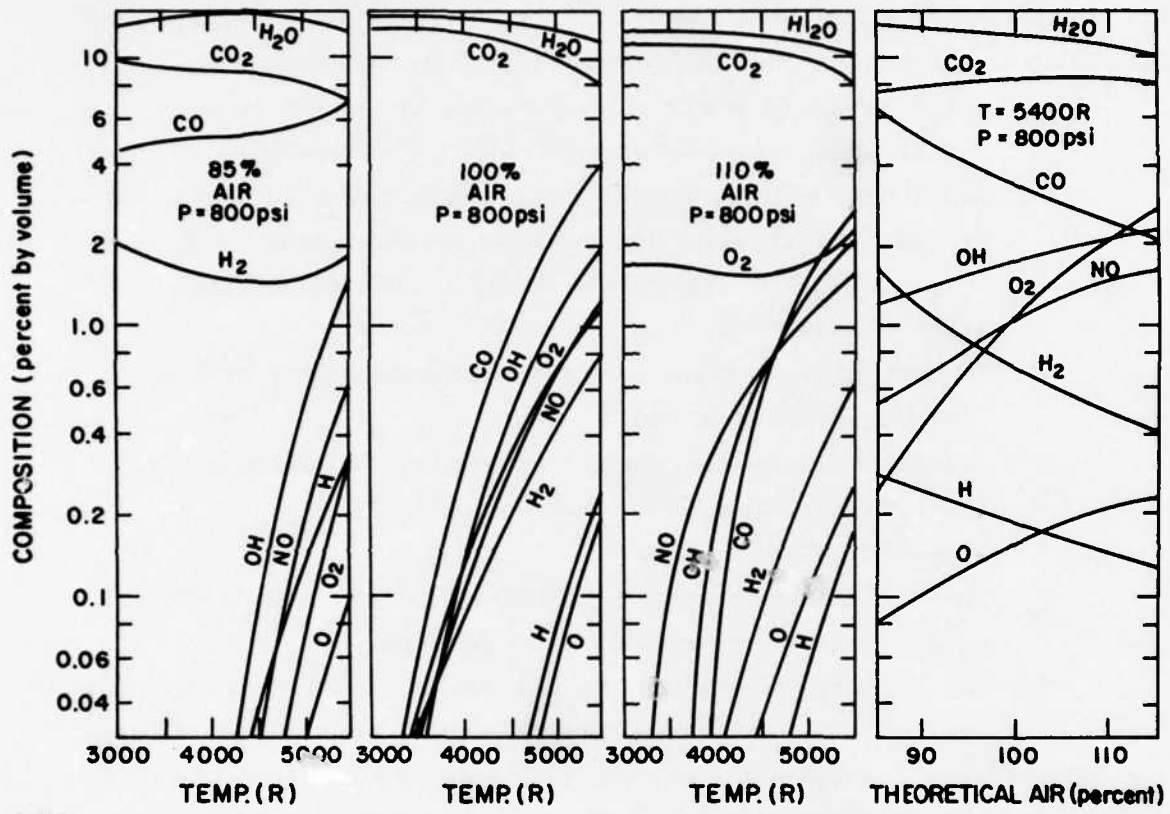
Since N₂ represents some 80 percent of the Earth's atmosphere, and since the balance is essentially O₂, the suggestion of an "air breathing" laser in which some compound is oxidized to produce a mixture of CO₂ and N₂ has long been considered. The third component needed is a molecule capable of transferring CO₂ bending vibration to translational motion, and a natural candidate for this is the H₂O produced in hydrocarbon combustion. Unfortunately, however, the presence of H₂O precludes the use of the low initial temperatures which improve laser specific output and efficiency, since fog formation increases cavity light scattering to the point where the laser will not operate. In addition, the molar fraction of H to C in hydrocarbons is between 2 and 1, thus producing at least half molecule H₂O for

each CO_2 molecule. Such a high ratio results in crippling deactivation of the CO_2 laser upper level, and for these reasons H_2O is an unsuitable component of the gas and must be extracted. The suggested solution to this problem is to use the H_2 molecule, produced by direct combustion as a result of fuel rich hydrocarbon burning, as the lower state deactivant. This was done successfully in experiments described below.

The CO_2 laser operates on the transition between the asymmetric molecular vibrational mode, labeled ν_3 (upper state), and the symmetric molecular vibrational mode, labeled ν_1 , which is the lower state. Efficient laser operation requires pumping of the upper state, which may be accomplished by electron excitation or by collisional transfer from a suitable vibrationally excited molecular species, among which are N_2 and CO . Deactivation of the lower state is also necessary, and is facilitated by the natural rapid transfer of energy between ν_1 and ν_2 (the bending mode), followed by the rapid transfer of energy between ν_2 and the translational mode.

Although in the conventional CO_2 laser the transfer from ν_2 to translational is for the most part facilitated by collisions with He, it is possible to use H_2 or H_2O for this purpose instead, and in fact H_2 has been shown to deactivate $\text{CO}_2\nu_2$ very rapidly and in accordance with theory.¹ Water, on the other hand, cannot be used at the low temperatures at which specific output is maximized² since it forms an opaque fog effectively preventing laser oscillation. This will be further discussed below.

The equilibrium products of combustion of hydrocarbons under various conditions of fuel richness and flame temperature are shown in Fig. 1.³ Detailed calculations² of optimum gas composition for the case of an H_2 -deactivated CO_2 laser system have shown that the best H_2 content is near 2 percent by volume. It is immediately apparent that, in the case of fuel-rich combustion of JP-4 in air (and very similar results obtain for other hydrocarbon fuels), using 85-percent air, the H_2 content is near optimum over the flame temperature range $1500 < T < 3000^\circ\text{K}$. After removal of the H_2O , it is therefore expected that a suitable gas for laser action will result from the simple combustion of JP-4 in air. As has been shown in preliminary experiments, this gas does provide lasing action.⁴



61398

Fig. 1 Equilibrium Combustion Products for Hydrocarbon Air Flame.
(Taken from Ref. 3)

The present program has been designed to test more completely the potentialities of the combustion-type gas mixture as a laser medium. In order to do this, certain questions must be dealt with theoretically and the conclusions reached tested experimentally (so far as possible). Information on the following points appears particularly important.

- a. Effect of CO on upper-state pumping and lower-state deactivation, especially at reduced temperatures.
- b. Sensitivity of laser output to concentration of H₂ and value at which upper-state deactivation becomes important.
- c. Effect of H₂O on output, due to fog scattering and upper-state deactivation.
- d. Degree to which laser output will be independent of CO₂ fraction (relative to N₂).
- e. Effect of uncombined O₂ and hydrocarbons on discharge and laser kinetics.
- f. Effect of pulse shaping.
- g. Level of dust concentration in laser gas at which laser operation may be expected to be reduced.

We will examine these points by choosing a standard gas mixture on the basis of combustion kinetics, and by varying the concentrations of the various species separately around their standard values. The theoretical predictions of the effect on laser output will be made using the AERL Kinetics Handbook,² and certain cases will also be tested experimentally.

1. 1. 2 Effect of Carbon Monoxide

The presence of CO in the combustion product gas is virtually unavoidable, if the gas is to be produced by burning in a fuel-rich environment. It is evident from Fig. 1 that the reducing gases CO and H₂ will be present under a wide variety of conditions in the approximate ratio 4:1. Unless the H₂ required for CO₂v₂ deactivation is to be added to the laser gas subsequently, generation of 2-percent H₂ is accompanied by the generation of 4- to 8-percent CO.

This species has two important effects, both of which are aspects of the same phenomenon. The high molecular vibrational excitation cross-section for electron collisions peaks at low electron energy, near 1 eV.

This results in CO vibrational excitation being the major energy loss process for slow electrons, so that a large fraction of the energy deposited in the electrons by the discharge field is immediately transferred from the electrons to the CO molecules. It is removed from the latter by two competing processes, V-V transfer to $\text{CO}_2^v_3$ and N_2 , and V-T deactivation of CO^* by H_2 . Figure 2(a) shows the fractional energy distribution from electrons into the various modes for the gas mixture $\text{N}_2:\text{CO}_2:\text{H}_2:\text{CO}$ (8:2:1:0.09:0) as a function of E/N , together with the drift velocity V_D , mean electron energy T_e and ionization rate I . Figure 2(b) shows the same distribution for the mixture (8.2:1:0.18:0.6), in which 6-percent CO has been added. Changing the H_2 concentration has negligible effect. Increasing the CO concentration causes a major change, since we observe that 30 to 40 percent of the electron energy is now transferred directly into CO^* , due to the high CO vibrational excitation cross section at low electron energies. Figure 2(c) shows the effect of 12-percent CO; more than 50 percent of the energy goes directly to CO^* . Similarly, the effect of changing the CO_2 fraction is shown in Figs. 2(d) and 2(e). The corresponding electron vibrational pumping rates are shown in Figs. 3(a) to 3(d).

Removal of higher-energy electrons by excitation of CO also results in a lower mean electron temperature in the discharge. Consequently, the ionization rate by electron collision is reduced and arcing is inhibited. The mean electron temperature at any given value of E/N is thus reduced by the addition of a small percentage of CO to the gas, and in comparing the laser efficiency and specific output for different gas mixtures one has to specify whether they are compared at constant T_e or constant E/N .

Such a comparison is given in Figs. 4(a) and 4(b), in which the effect of CO is shown in comparison with that of CO_2 . The standard fraction of CO_2 in the combustion product mixture is 10-percent. The result of adding CO to the standard mixture is shown by the lines emanating from the point corresponding to standard CO_2 concentration, as denoted by an asterisk. These calculations have been performed both for the cases of constant E/N , taking $E/N = 2.35 \times 10^{-16}$, and for constant electron temperature, taking $T_e = 1$ eV. Since in the case of constant electron temperature the value of E/N will increase with increasing CO fraction, the

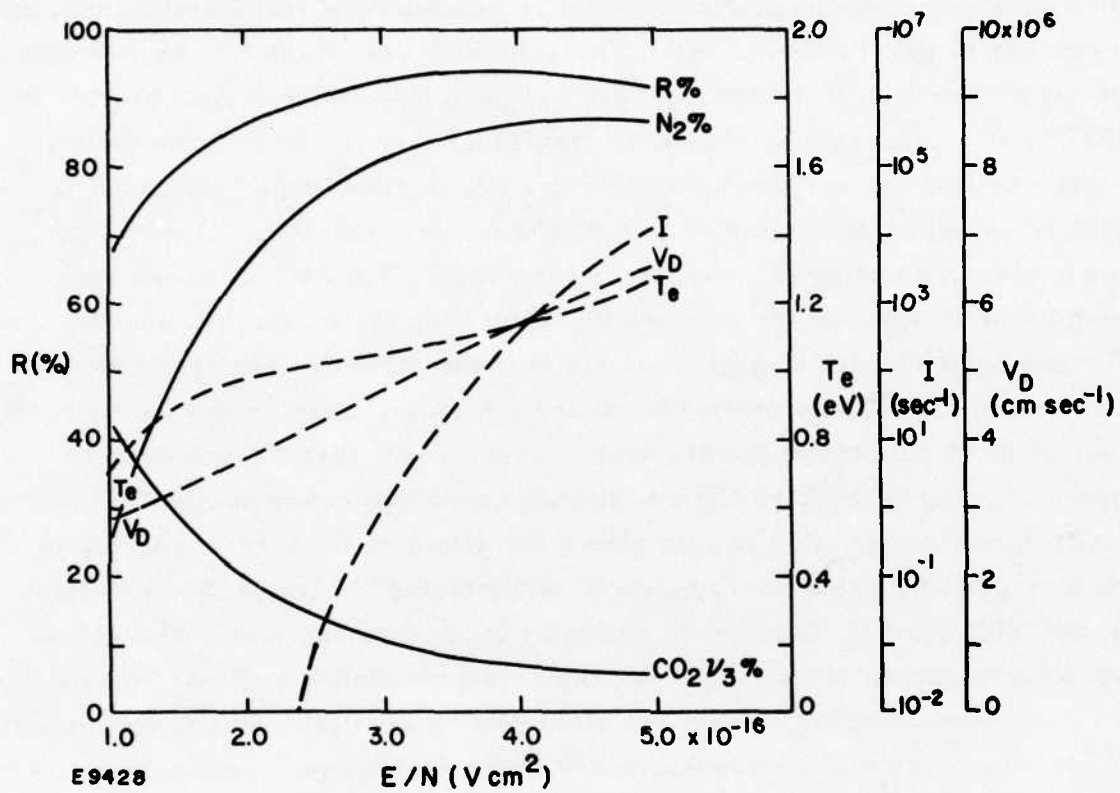


Fig. 2(a) Fractional Energy Pumped into Vibrational Modes by Electrons, as Function of E/N , in the Gas $N_2:CO_2:CO:H_2$ (8. 2: 1: 0: 0. 09).

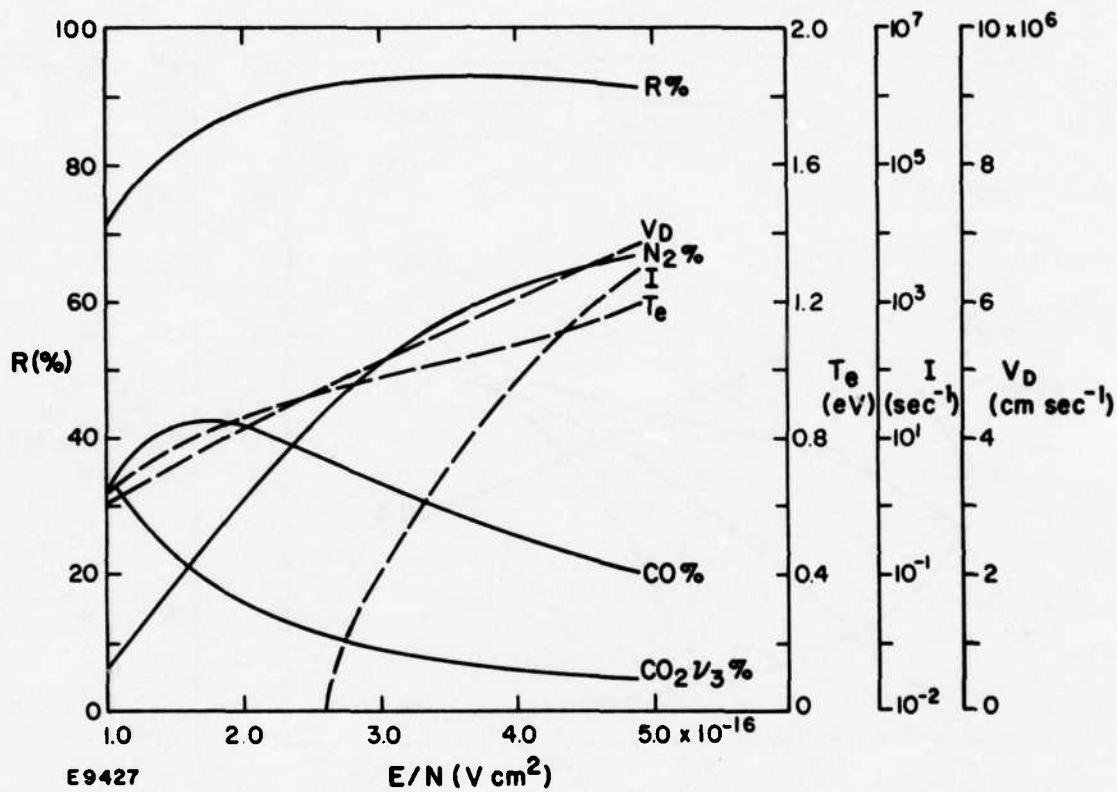


Fig. 2(b) Fractional Energy Pumped into Vibrational Modes by Electrons, as Function of E/N , in the Gas $N_2:CO_2:CO:H_2$ (8.2:1:0.6:0.18).

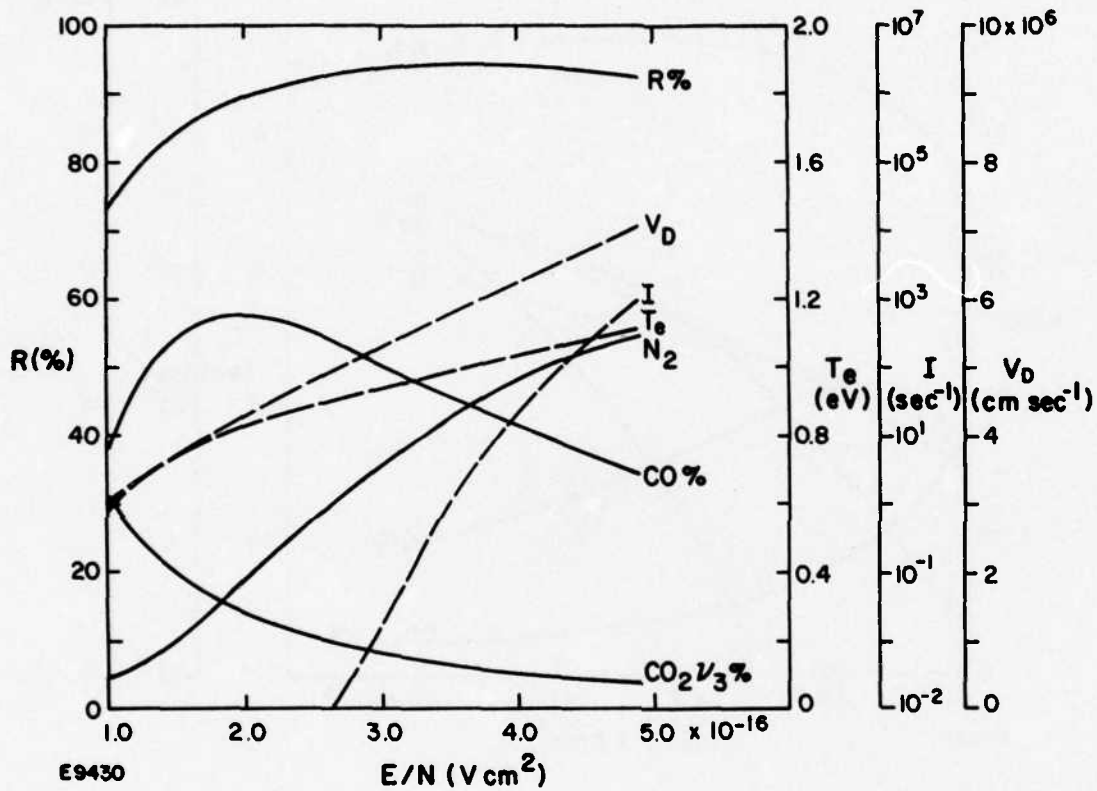


Fig. 2(c) Fractional Energy Pumped into Vibrational Modes by Electrons, as Function of E/N , in the Gas $\text{N}_2:\text{CO}_2:\text{CO}:\text{H}_2$ (8. 2: 1: 1. 2: 0. 18).

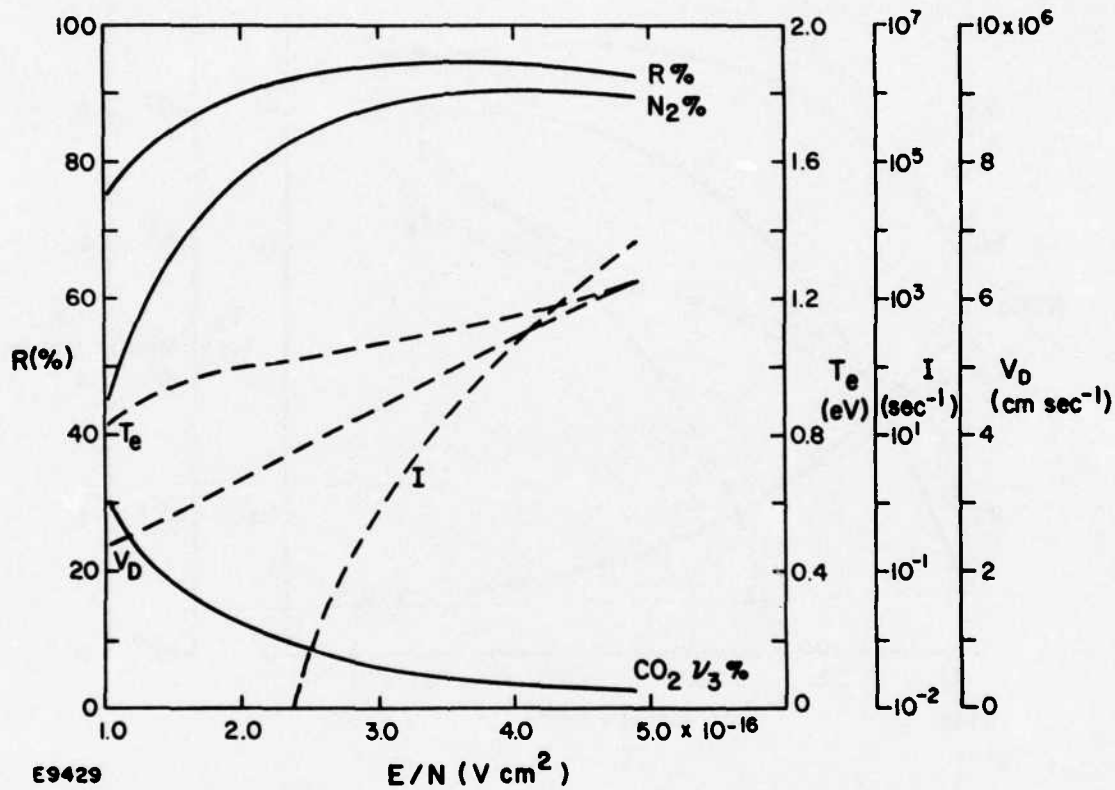


Fig. 2(d) Fractional Energy Pumped into Vibrational Modes by Electrons, as Function of E/N , in the gas $N_2:CO_2:CO:H_2$ (16.4:1:0.36:0).

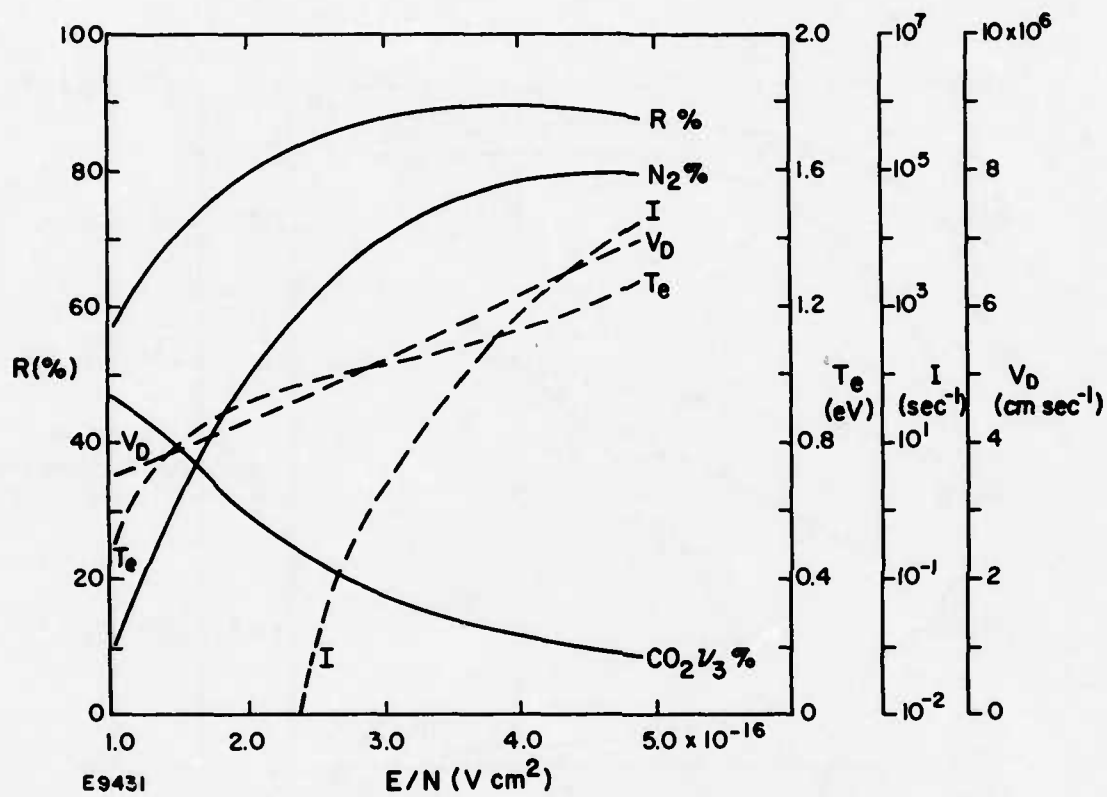


Fig. 2(e) Fractional Energy Pumped into Vibrational Modes by Electrons, as Function of E/N , in the Gas $N_2:CO_2:CO:H_2$ (4. 1: 1: 0: 0.09).

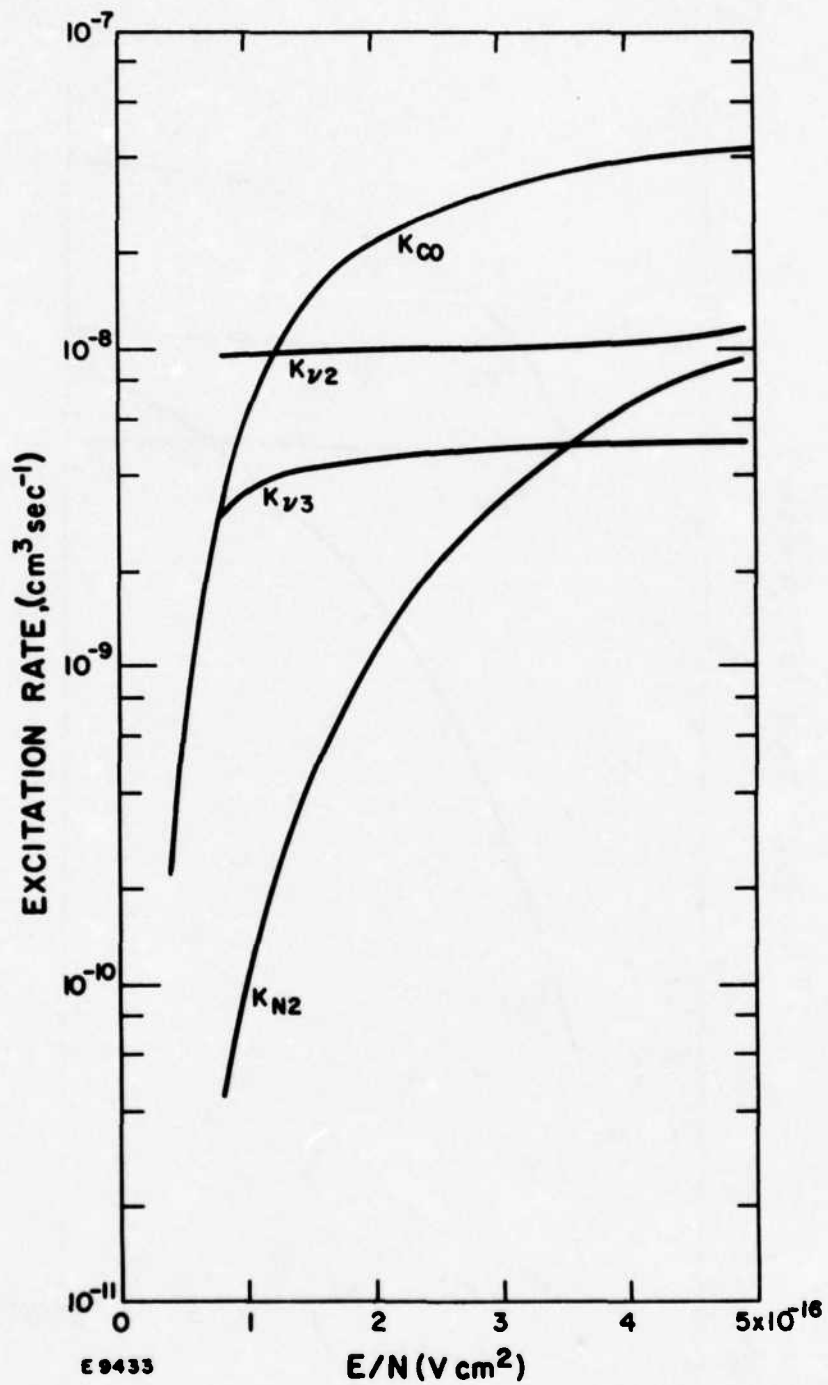


Fig. 3(a) Electron Impact Vibrational Excitation Rates in the Gas
 $N_2: CO_2: CO: H_2$ (8. 2: 1: 0. 6: 0. 18).

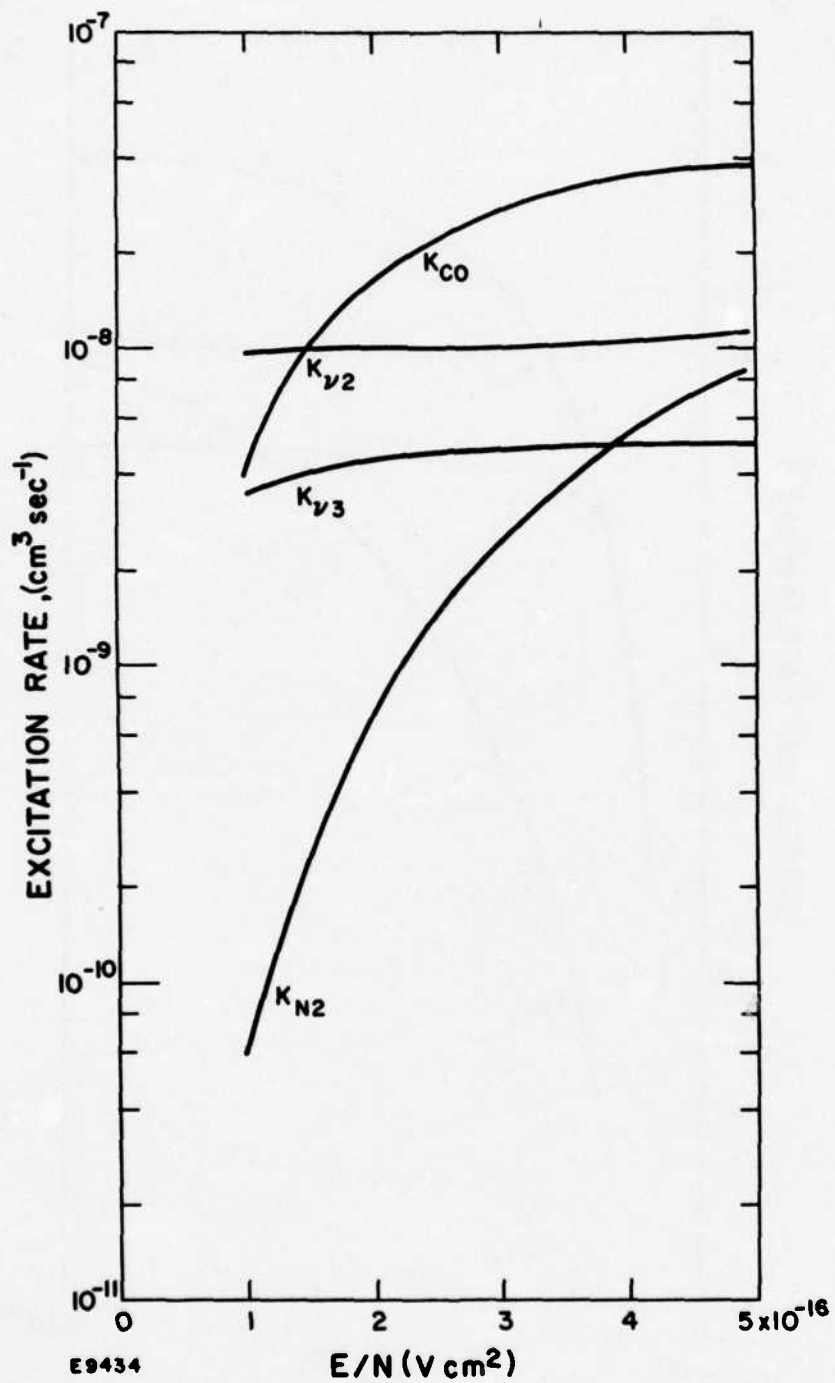


Fig. 3(b) Electron Impact Vibration Excitation Rates in the Gas
 $N_2: CO_2: CO: H_2$ (8. 2: 1: 1. 2: 0. 18).

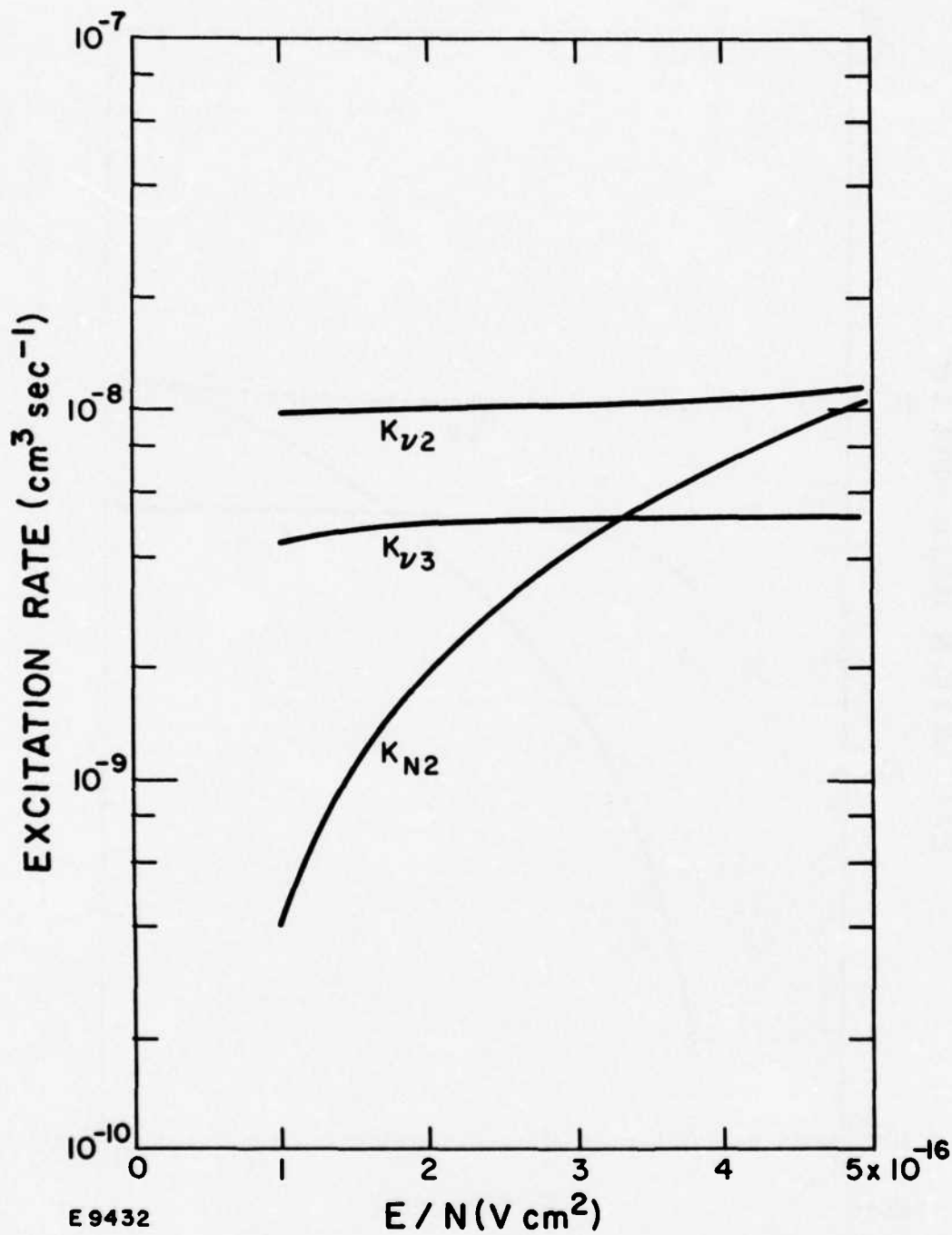


Fig. 3(c) Electron Impact Vibrational Excitation Rates in the Gas
 $N_2:CO_2:CO:H_2$ (16.4:1:0:0.36).

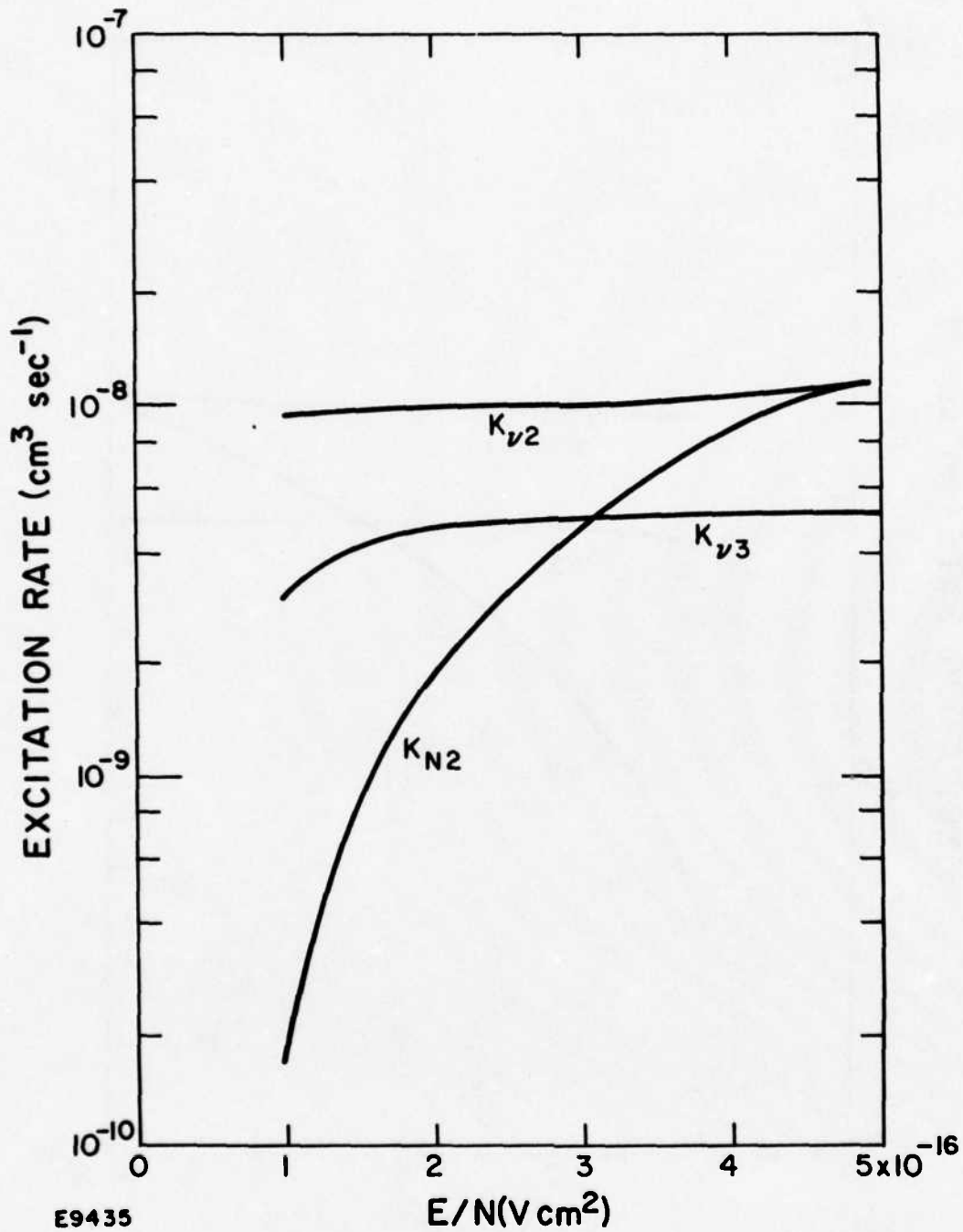


Fig. 3(d) Electron Impact Vibrational Excitation Rates in the Gas
 $N_2:CO_2:CO:H_2$ (4. 1: 1: 0: 0.09).

ACTIVANTS

$T_{g_0} = 200^\circ\text{K}$

STANDARD GAS

$P = 1 \text{ ATM}$

$\text{N}_2 : \text{CO}_2 : \text{H}_2$

$g_c = 0.5\%/\text{CM}$

8:2 : 1 : 0.18*

$T_e = 1 \text{ eV}$

EFFECT OF CO

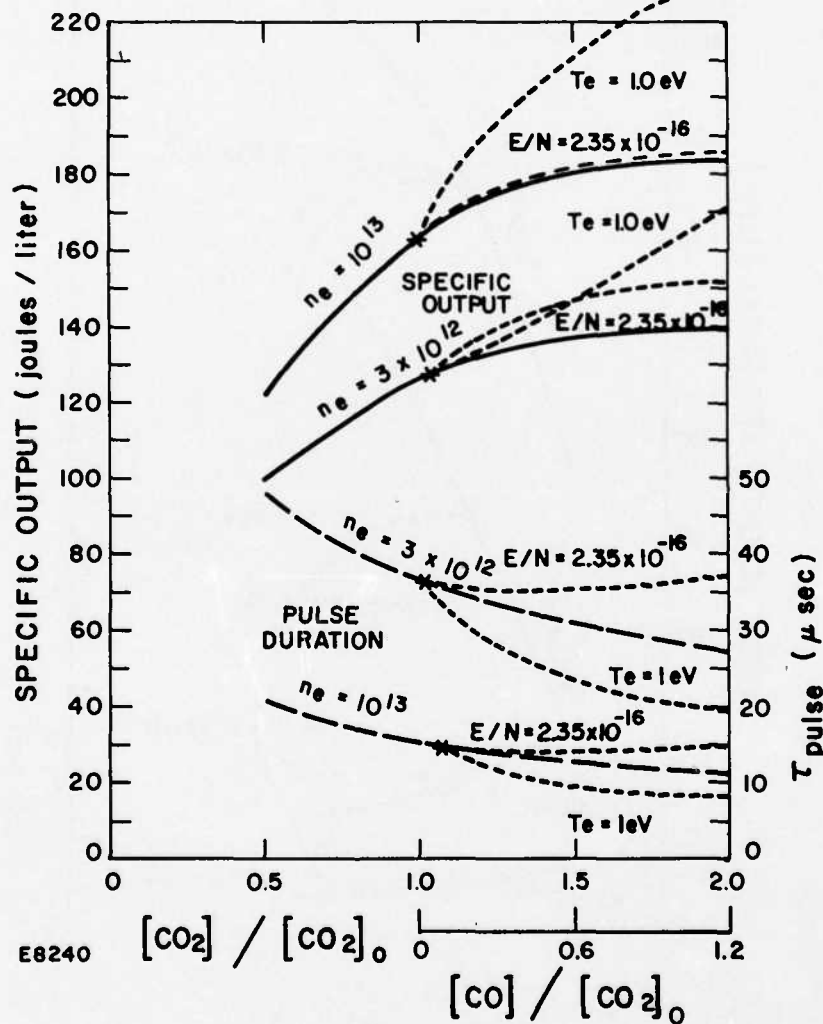


Fig. 4(a) Effect on Specific Output and Pulse Duration of Altering $[\text{CO}_2]$ and $[\text{CO}]$ Relative to the Standard Fraction $[\text{CO}_2]_0$ for the Standard Gas Mixture. Electron density 3×10^{12} and 10^{13} and electron temperature 1 eV have been maintained as shown, and for gases containing CO an additional line is indicated for the case of constant $E/N = 2.35 \times 10^{-16}$. Standard gas mixture is shown by an asterisk, and CO containing mixtures branch out as dotted lines from that point.

ACTIVANTS

$T_{g_0} = 200^\circ\text{K}$

STANDARD GAS

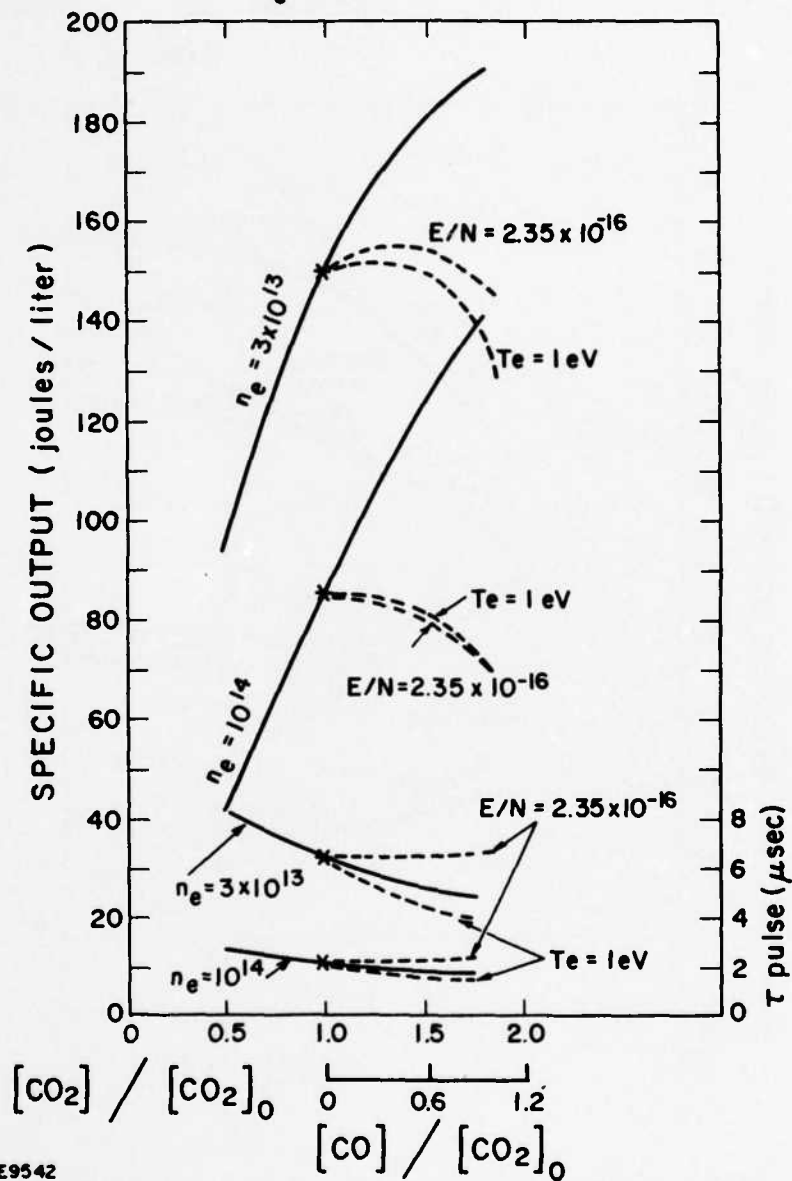
$P = 1\text{ ATM}$

$\text{N}_2 : \text{CO}_2 : \text{H}_2$

$q_c = 0.5\%/\text{CM}$

8.2 : 1 : 0.18*

$T_e = 1\text{ eV}$



E9542

Fig. 4(b) Effect on Specific Output and Pulse Duration of $[\text{CO}_2]$ and $[\text{CO}]$ at $n_e = 3 \times 10^{13}$ and 10^{14} .

output for this case increases as [CO] increases. In the opposite case of constant E/N, the behavior is more similar to that of increasing the CO₂ fraction. However, the net effect of the presence of CO in these gases appears to be theoretically favorable.

The V-T (or V-R) deactivation of vibrationally excited CO by H₂ is extremely rapid,⁵ reaching values near $\tau_d \approx 10^{-4}$ atm-sec at 300°K. We estimate the importance of this deactivation route in the collisional deactivation of CO₂ (001). Using the notation of the AERL Kinetics Handbook² we may write the ratio of the deactivation rates as:

$$R = \left(\frac{\psi_{\text{CO}} \psi_{\text{H}_2}}{\tau_{\text{cod}}} \cdot \frac{b_2}{1 - b_2} \right) / \left(\psi_c \sum_i \frac{\psi_i}{\tau_{\text{li}}} \cdot \frac{r}{1 - r} \right),$$

in which ψ_{CO} , ψ_{H_2} and ψ_c represent molar fractions of CO, H₂ and CO₂, $\frac{r}{1 - r}$ and $\frac{b_2}{1 - b_2}$ are CO₂(001) and CO(1) molar fractions, and τ_{cod} and τ_{li} are the characteristic deactivation times for CO(1) by H₂ and for CO₂(001) by species i, respectively. Inserting typical values of the gas mixture and inversion parameters yields $R \approx 10^{-3}$, so that only a very small fraction of the net upper-state vibrational energy will be deactivated by this route. The rapidity of deactivation of CO by H₂ is offset by the relative scarcity of these species.

In general most V-V and V-T transfer rates for 200°K gas temperature must be extrapolated from the curves for measurements down to 300°K. (Fortunately, the kinetics is quite insensitive to the rates below 300°K, since the related inefficiencies of the lasing process are quite small compared with the inefficiencies suffered later in the pulse when the gas temperature is 400°K, or higher, and a more accurate knowledge of the V-V and V-T rates as required.) However, vibrational energy transfer from excited CO to N₂ and CO₂ has been studied in the excellent work of Starr and Hancock, who measured the transfer rates down to temperatures of 150°K. We note that even relatively large changes in the transfer rates will not greatly affect the final laser output, since the only important route by which CO can be deactivated is through transfer to N₂ and CO₂. The spontaneous decay time of excited CO is several orders of magnitude longer, and the V-T and V-R direct deactivation of CO appears much less important

than the collisional deactivation of CO_2 , as discussed above. We therefore expect that the peculiar pumping system existing when CO is present, in which 6-percent CO takes 40 percent of the discharge energy (see Fig. 2(b)), should not reduce the laser efficiency or output. At very high electron densities the pumping rate becomes comparable with the CO- CO_2 transfer time leading to decreased output, as shown in Fig. 4(b).

1.1.3 Effect of Hydrogen and Water Vapor

The efficient V-T or V-R deactivation of $\text{CO}_2 \nu_2$ by H_2 is accompanied by slightly less efficient deactivation of $\text{CO}_2 \nu_3$, due to the greater energy of the latter excited state. Consequently, there are upper and lower bounds on the permissible H_2 fraction. This is indicated in Figs. 5(a) and 5(b), in which laser output in a typical configuration is calculated as a function of $[\text{H}_2]$, relative to the standard gas mixture. It is evident that between ~ 1- and ~ 3-percent H_2 gives a flat maximum in the output for electron density of 3×10^{12} , while for higher n_e , and consequently higher pumping rate, the maximum is at higher $[\text{H}_2]$, as would be expected. We conclude that over the range of pulse durations of interest, 10 to 20 μsec , we need $n_e \sim 10^{13}$ and $1\% < [\text{H}_2] < 3\%$, approximately.

1.1.4 Effect of H_2O

Water vapor is a more effective deactivator of $\text{CO}_2 \nu_2$ and $\text{CO}_2 \nu_3$ than H_2 . It also has the property of absorbing electrons by dissociative attachment, which is an undesirable feature for the discharge since it can lead to the attachment instability.⁶ The effect on the laser kinetics of adding H_2O to the discharge is also shown in Figs. 5(a) and 5(b), relative to the standard gas. As expected, in the high-pumping case, for which the standard value of $[\text{H}_2]$ is slightly below optimal, the addition of ~ 0.2-percent water vapor causes an increase in output, and further addition results in output decrease. For the low-pumping case, where the value of $[\text{H}_2]$ is near optimum, the addition of H_2O merely increases $\text{CO}_2 \nu_3$ deactivation and reduces output. We conclude that the presence of 1/2-percent H_2O in the gas mixture will reduce laser output by 1 percent, typically.

The other effect produced by water vapor is the generation of fog in the laser medium. Using the criterion derived below Section 1.1.7(b)

DEACTIVANT

$T_{g_0} = 200^\circ\text{K}$ STANDARD GAS
 $P = 1 \text{ ATM}$ $\text{N}_2 : \text{CO}_2 : \text{H}_2$
 $q_c = 0.5\%/\text{CM}$ 8:2 : 1 : 0.18*
 EFFECT OF H_2O

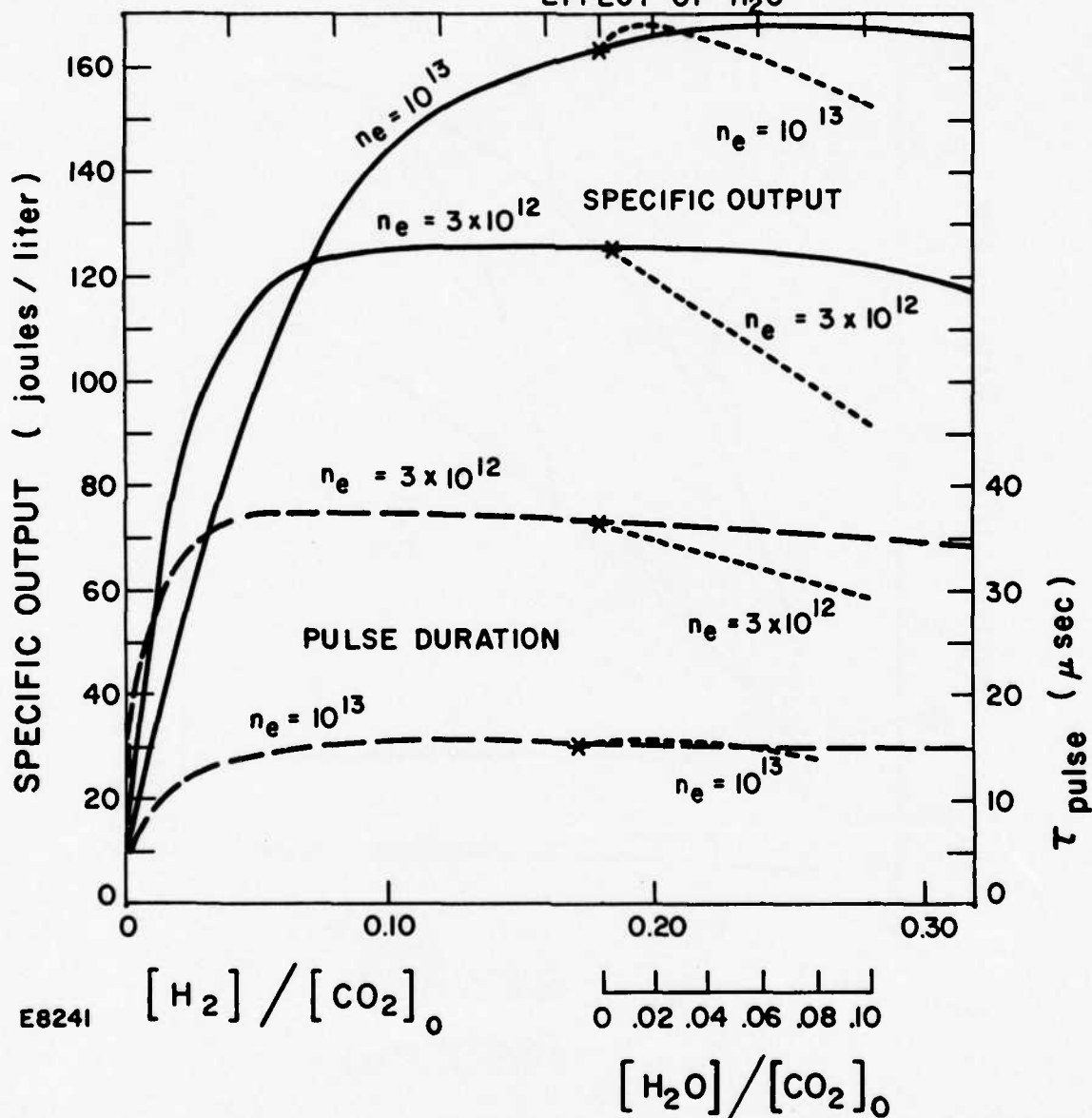


Fig. 5(a) Effect on Specific Output and Pulse Duration of Altering the Deactivating Components $[\text{H}_2]$ and $[\text{H}_2\text{O}]$, Relative to the Standard Fraction of CO_2 . The standard gas mixture is shown as an asterisk, and the effect of adding $[\text{H}_2\text{O}]$ branches out from that point, shown as a dotted line. Values for $n_e = 3 \times 10^{12}$ and 10^{13} are indicated.

DEACTIVANTS

$T_{g_0} = 200^\circ\text{K}$ STANDARD GAS
 $P = 1 \text{ ATM}$ $\text{N}_2 \cdot \text{CO}_2 \cdot \text{H}_2$
 $g_c = 0.5\%/\text{CM}$ $8.2 \cdot 1 \cdot 0.18^*$
 $T_e = 1\text{eV}$

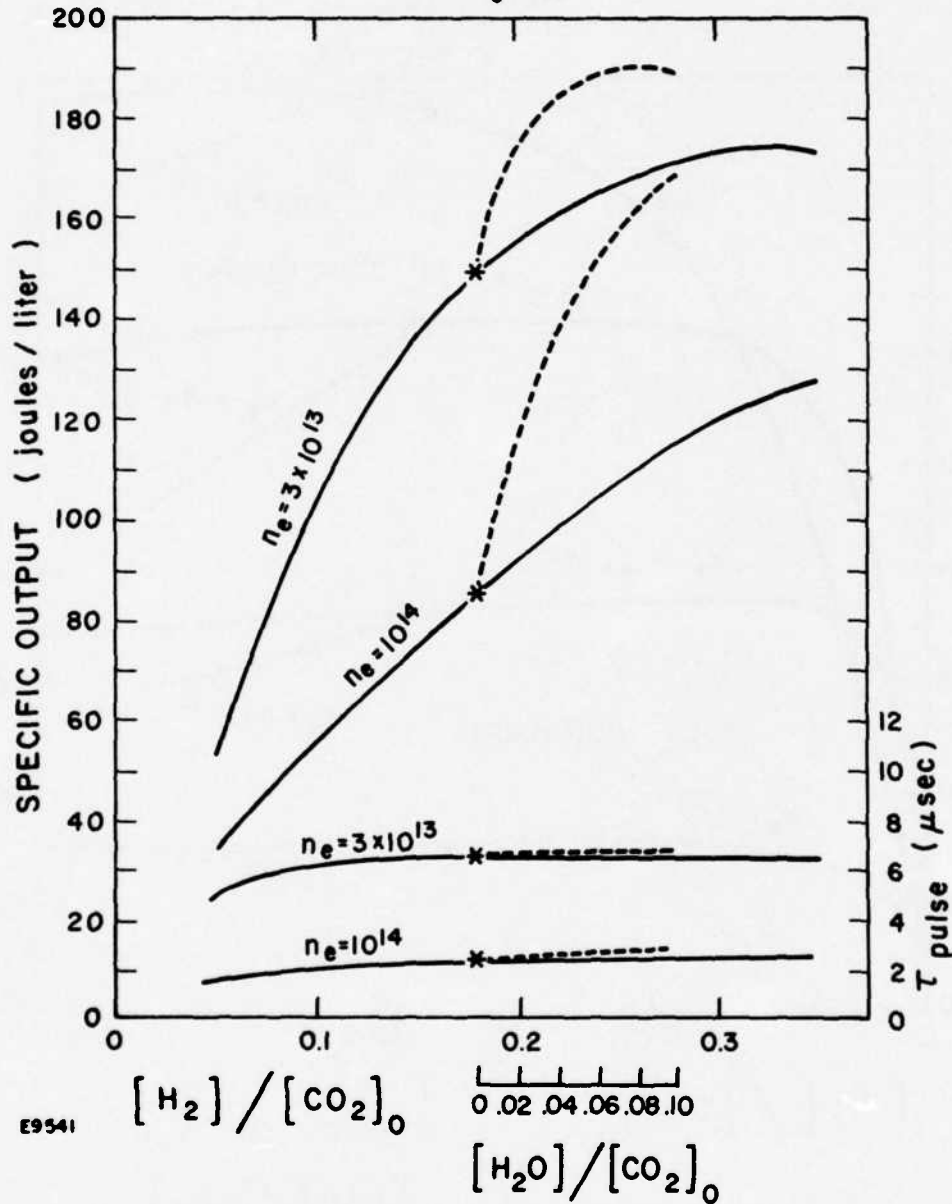


Fig. 5(b) Effect on Specific Output and Pulse Duration of Deactivants for $n_e = 3 \times 10^{13}$ and 10^{14} .

for the Mie scattering of light by water droplets of radius r , for which the combined Mie scattering and absorption efficiency is $Q \cong 10^4 r$, we find that the output flux would be decreased by 1 percent for a water-vapor content of approximately 0.3 percent. Thus this number is close to that predicted by the upper-state deactivation criterion.

1.1.5 Effect of Hydrocarbons and Oxygen

The electron density n_e is governed by the equation (See Ref. 2)

$$\frac{dn_e}{dt} = S - \alpha n_e^2 - \beta n_e$$

where S is rate of secondary electron formation by the E-beam, α is the ion-electron recombination rate and β is the molecule-electron attachment coefficient. The source function S is proportional to the high energy E-beam current density. S decreases somewhat across the cavity, going away from the E-beam foil. Due to scattering of the E-beam in the foil and in the gas, the amount of spreading depending on the foil material and thickness, in the E-beam voltage and on the aspect ratio of the cavity.

The presence of these hydrocarbons and oxygen may affect the electron economy of the gas mixture. In particular, low ionization-potential hydrocarbon fragments may take up the discharge positive charge by rapid charge-transfer. If the dissociative recombination coefficient α then greatly exceeds that for the normal discharges the electron density will decrease, since $n_e = \sqrt{S/\alpha}$. However, this has not been observed in experimental results to date and is not expected to be a problem.

Similarly, electron-neutral attachment by hydrocarbon fragments should not occur to an important extent. The electron affinities of hydrocarbons are generally low and the electron attachment rates may be neglected, except in the case of certain aromatic benzene ring compounds which are not anticipated in the present case.

Collisional V-T deactivation of $\text{CO}_2\nu_3$ and the other equivalent upper state excited molecules is more probable in collision with the large molecules with many degrees of freedom typified by hydrocarbons. However, it is unlikely that the deactivation efficiency for collisions with $\text{CO}_2\nu_3$ will exceed that for H_2O , for which we observed above that a concentration of 0.5 percent was acceptable. Since less than 0.5-percent

hydrocarbons should exist in an efficiently burnt mixture, we consider it most unlikely that these species will adversely affect the saturation flux of the laser.

The O_2 molecule will have negligible effect on the gas kinetics taking place in the discharge, since its collisional V-V deactivation coefficient with $CO_2\nu_3$ is quite low. Its electron affinity is not low, and electrons will be lost from the discharge by electron attachment to the O_2 molecules. The effect produced by O_2 is shown in Fig. 6, in which the presence of O_2 becomes important when $\beta \approx \alpha n_{e0}$, i. e., when the attachment loss rate βn_{e0} becomes equal to the recombination rate αn_{e0}^2 . Taking $n_{e0} = 3 \times 10^{12}$ and $\alpha = 2 \times 10^{-7}$, we get $\beta \approx 6 \times 10^5$. This corresponds to approximately 0.5-percent O_2 in the gas. We should therefore attempt to keep the O_2 content well below this number. In the case of higher electron density and higher pumping rates, we note that this criterion is proportionately relaxed.

1. 1. 6 Predicted Laser Performance with E-Beam Variations

The results of ramping the electron beam up and then down are shown in Figs. 7(a) and 7(b). This has been applied to the two gas mixtures $N_2:CO_2:CO:H_2$, (8.2:1:0:0.8) and (8.2:1:0.6:0.18), denoted mixtures A and B, in order to illuminate the behavior of CO in the mixture. Recombination and attachment lag in electron density has been suppressed.

The same computation has been performed using an electron density proportional to $\sin^2 \omega t$, where ω is an arbitrary number. The results are shown in Figs. 8(a) and 8(b) for the same two gases. As anticipated, the highest level pumped is CO in the case where the gas is present, and the calculated CO^* population fraction reflects the pumping rate, which is proportional to the electron density. We would therefore expect this type of laser to be capable of producing an arbitrary signal using the present gas system, in which variation in the electron beam will be reflected in the output signal. We note that the characteristic recombination timescale is $\tau \sim (\alpha n_{e0})^{-1} \sim 1 \mu\text{sec}$ in the present experimental conditions, and that consequently it should be possible to generate frequencies lower than 10^6 Hz.

1. 1. 7 Acceptable Level of Smoke

The effect of particulate matter in the electron beam sustained laser (EBS) is important especially in the case where the source gas is the

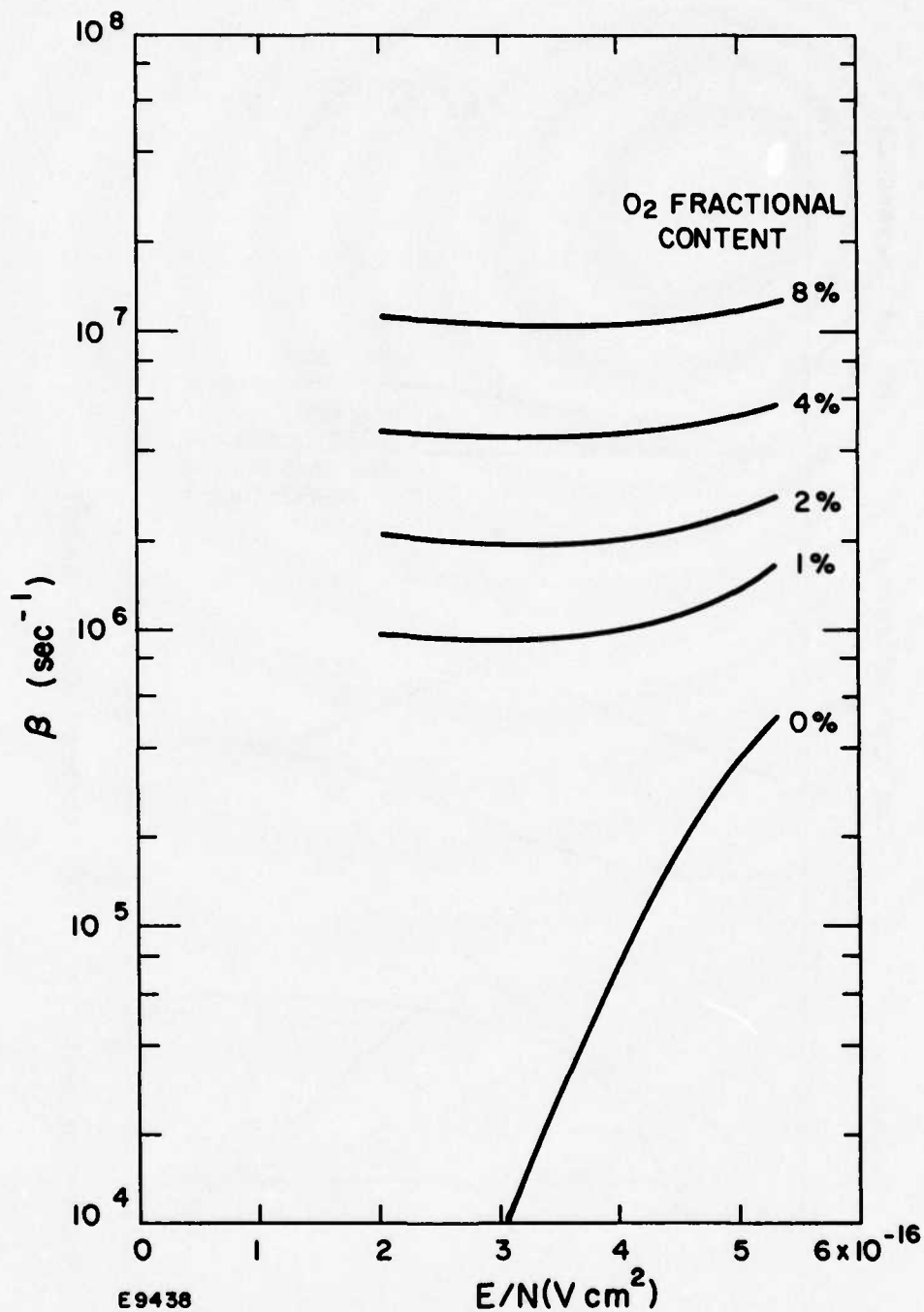


Fig. 6 Attachment Coefficient β for the Standard Gas to which a Fraction ψ_{O_2} of O_2 has been added. The sum of three-body and dissociative attachment coefficients is used. The zero O_2 line corresponds to dissociative attachment to the molecule.

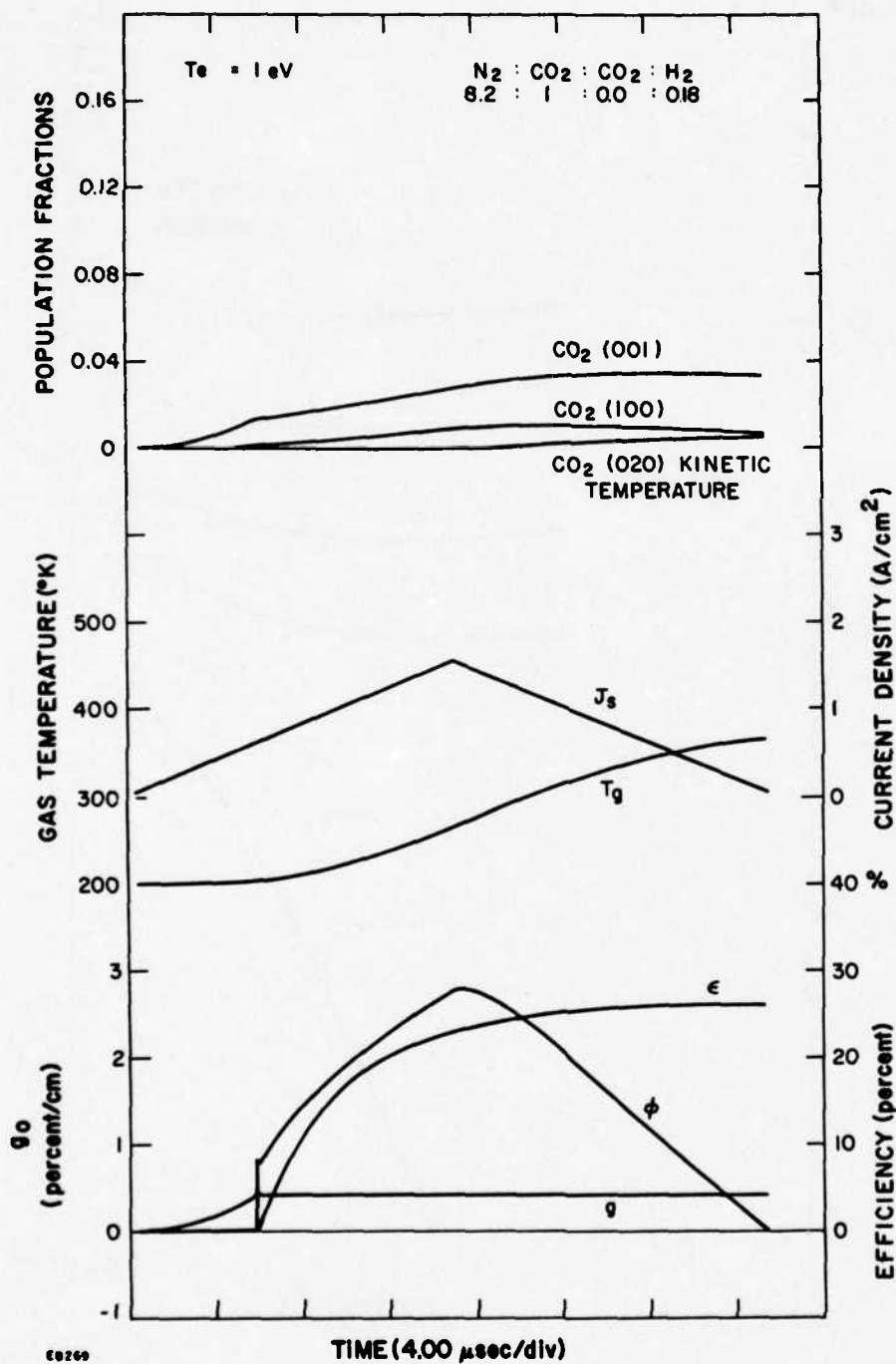


Fig. 7(a) Kinetics of CO_2 Laser for Ramped Power Input. Top three graphs give molecular population fractions, J_s and T_g are current density and gas kinetic temperature, and ϵ , ϕ , and g are net electrical efficiency, flux intensity (arbitrary units) and laser gain, respectively.

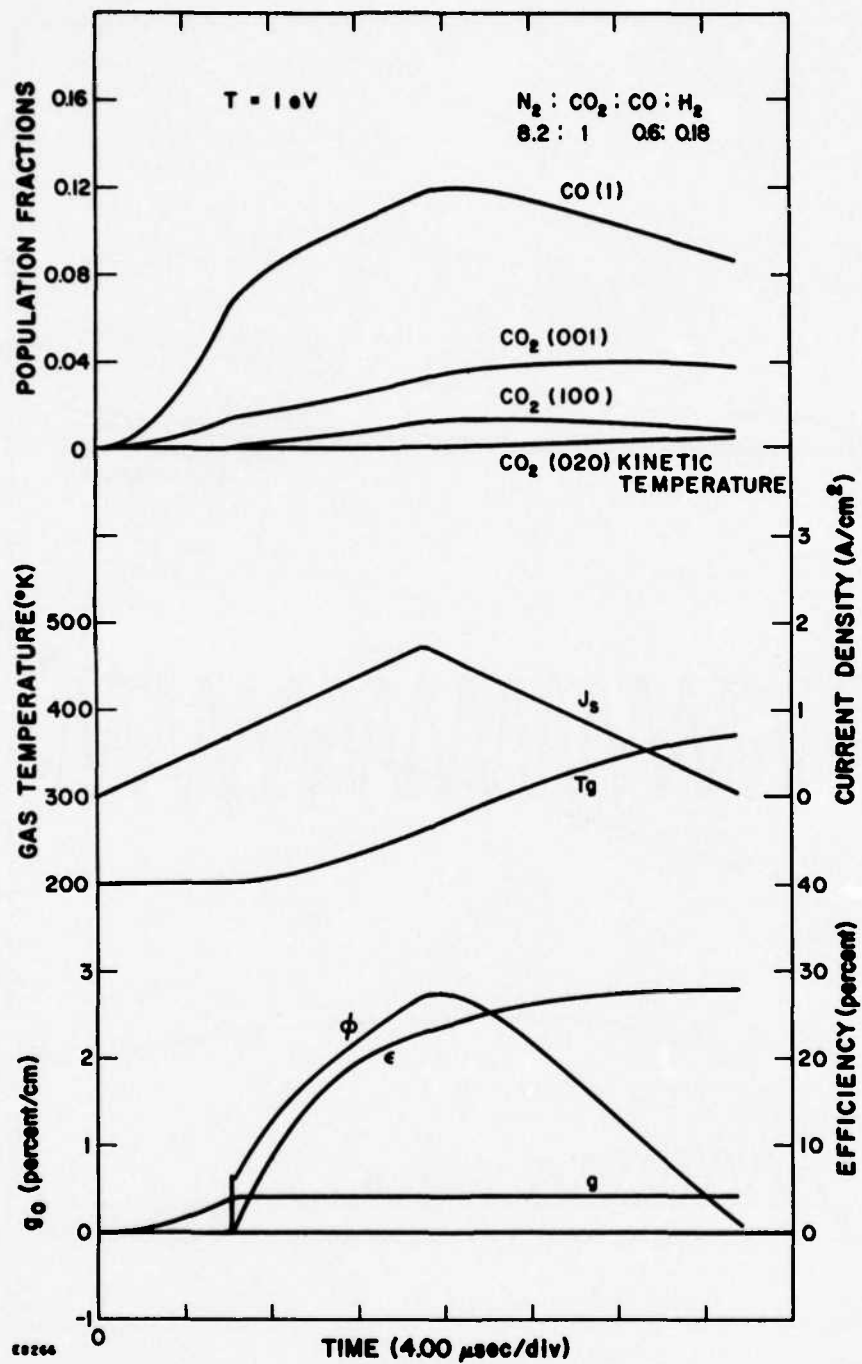


Fig. 7(b) Kinetics of CO₂ Laser for Ramped Power Input with 6-Percent CO Present in the Gas Mixture.

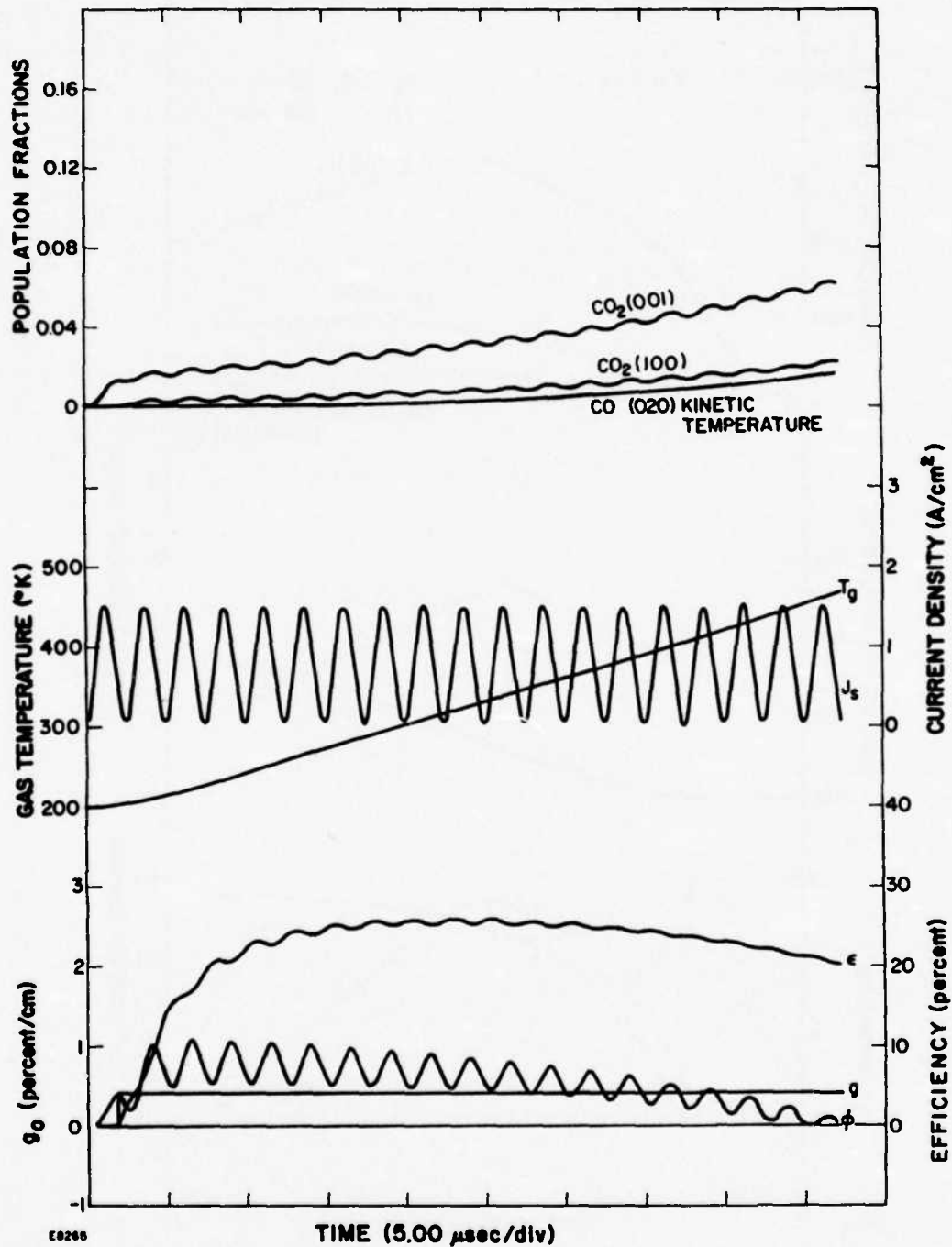


Fig. 8(a) Kinetics of CO₂ Laser System Using Sinusoidal Power Input, for Example by Varying the Electron Beam so as to Produce the Sustainer Current Indicated.

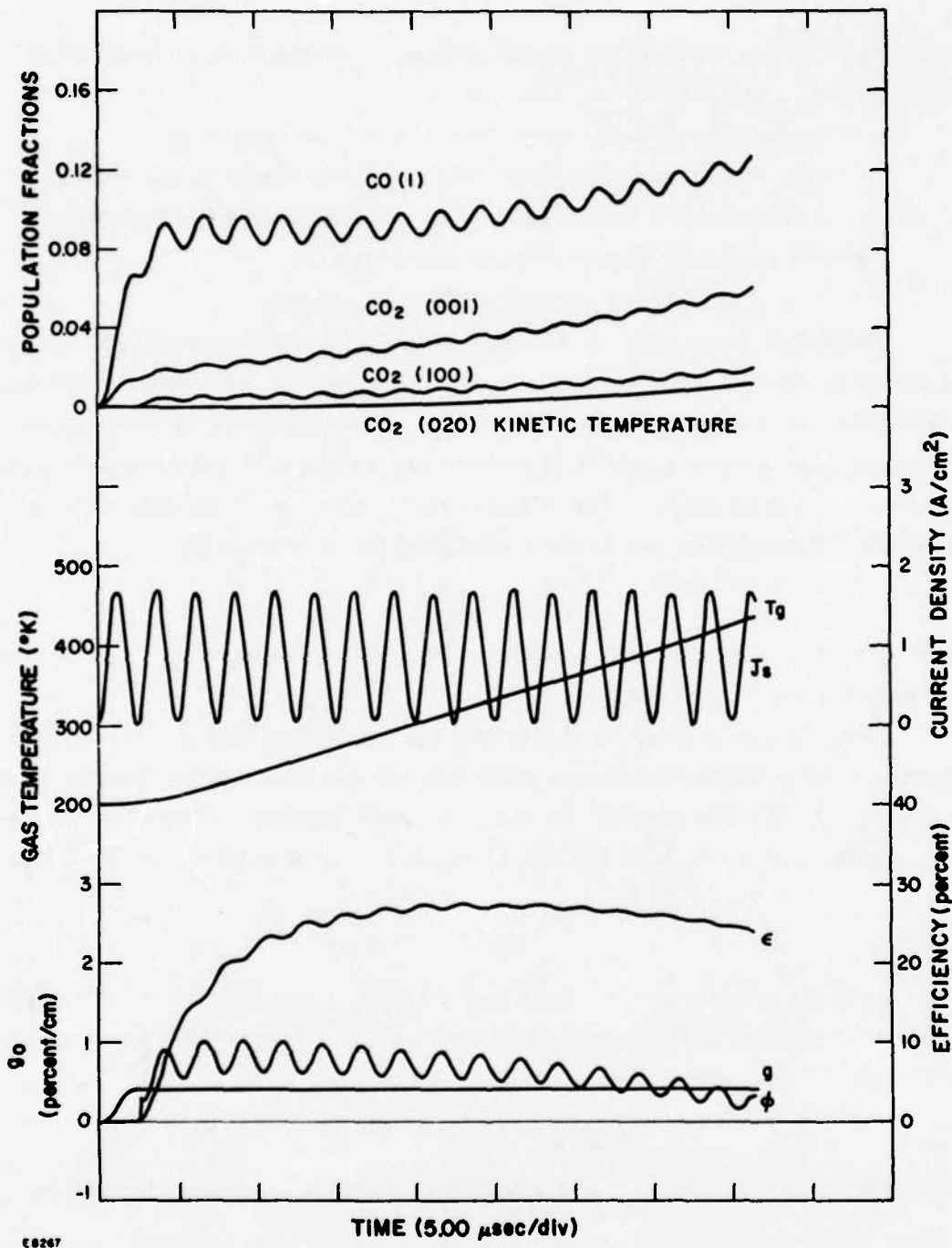


Fig. 8(b) Kinetics of CO_2 Laser Using Sinusoidal Power Input with 6-Percent CO Present. Note higher amplitude of $CO(1)$ fluctuations due to large energy fraction passing through that mode.

combustion product of burning hydrocarbons. We note that three interactions will be particularly significant.

- a. Interaction of discharge electrons with particles.
- b. Mie scattering and absorption of laser light by particles.
- c. Breakdown of laser gas caused by particle volatilization.

We will consider these effects separately.

1.1.7.1 Particulate Matter in EBS Discharge

Particles suspended in the gas of an EBS discharge will be charged by collection of electrons up to an equilibrium value, at which the rates of charging and discharging are identical. The presence of this charge then causes the particles to drift toward the anode and consequently remove them from the discharge. The steady-state velocity V at which the particles drift through the gas is then obtained from Stokes law:

$$V = \frac{qE}{6\pi a\eta} \quad (1)$$

where q and E are electric charge and field, respectively, a is particle radius and η is gas viscosity.

The charge q may be estimated by assuming that the discharge current to the particle continues until the charge-carriers (electrons) are repelled from the surface by the electric field buildup. The electric field at the surface of a charged sphere of radius a in a uniform field E_0 is

$$E = 3E_0 \cos \theta - \frac{q}{4\pi \epsilon_0 a^2}$$

where θ is the angle between field and radius. The maximum possible charge will then be that for which there is no positive value for E over the surface of the sphere, so that $\theta = 0$ and

$$q_{\max} = 12 \pi \epsilon_0 E_0 a^2 \quad (2)$$

Substituting Eq. (2) in Eq. (1) gives the maximum particle drift velocity

$$V_{\max} = \frac{2 \epsilon_0 E_0^2 a}{\eta}$$

Numerically, taking $\eta = 1.13 \times 10^{-4}$ poise (or 1.13×10^{-5} mks), the value for air at 169°K, $E = 5$ kV/cm, $a = 10^{-4}$ cm, we obtain for 1-nm particles

$$V_{\max} = 39 \text{ cm/sec}$$

The discharge time is characteristically 20 μsec , corresponding to a distance of 8 μm moved by the particle. We therefore conclude that precipitation processes will be insignificant in this discharge and the particles will remain in the optical medium.

1.1.7.2 Mie Scattering and Absorption of Light by Particles

For particle sizes comparable to the optical wavelength of 10.6 μm , Mie scattering and absorption become important. We will consider the case of carbon particles, whose complex refractive index at 10 μm is $3.5 + 2.5i$.

The absorption and scattering of light of intensity I by a particle of radius a may be expressed by the equation

$$\frac{dI}{dx} = - (Q_s + Q_a) \pi a^2 N I$$

where Q_s and Q_a are the Mie coefficients for scattering and absorption and N is particle number density. Since the mass of particles per cm^3 is $m = 4/3 \pi a^3 N \rho$, where ρ is density, the extinction coefficient becomes

$$g' = \frac{3 Q m}{4 a \rho}, \text{ where } Q = Q_s + Q_a.$$

We obtain the values of Q_s and Q_a from the detailed calculations of Wickramasinghe.⁷ We note that for $a < \lambda$, $Q \propto a$, approximately, thus giving us the fact that extinction depends only on particle mass density in the gas. This will give an upper limit on permissible particulate mass density, since in fact the absorption by larger particles will be overestimated by taking $Q \propto a$. We may therefore state that the maximum permissible particulate mass density is

$$m_{\text{max}} = \frac{4 a \rho}{3 Q} g'_{\text{max}} \quad (3)$$

Now the maximum permissible value of g' may be defined by requiring that its effect on laser output will be less than 1 percent. Using the integration² of the Rigrod equation, we relate the laser output flux ϕ to the zero-flux gain and cavity losses as

$$\phi = L \phi_s [g_0 - (g_c + g')]$$

where L is cavity length, ϕ_s is saturation flux, and g_0 and g_c are zero-flux and cavity gain, respectively.

Here

$$\frac{\Delta\phi}{\phi} = - \frac{\Delta g'}{g_0 - (g_c + g')}.$$

so that $\Delta g' \leq 0.01 [g_0 - (g_c + g')]$.

Placing $\Delta g' = g'$ we obtain

$$g' \leq \frac{0.01}{1.01} (g_0 - g_c).$$

Now typically $g_0 \sim 5\%/cm$ and $g_c \sim 1\%/cm$, so that $g' \leq 4 \times 10^{-4} cm^{-1}$, approximately. Substituting this into Eq. (3) yields the maximum permissible particulate mass loading. For $\frac{\Omega}{a} \approx 6000 cm^{-1}$, which is correct for carbon, we obtain

$$m_{max} = 1.8 \times 10^{-7} g/cm^3.$$

Since the gas density will be $1.2 \times 10^{-3} g/cm^3$, we require that the maximum permissible particulate fractional mass loading is near 2×10^{-4} or 0.02 percent of the gas weight. More precisely, this is the condition on particle content for particles for which $a \ll \lambda$. In fact, these are the most difficult particles to remove under the best circumstances.

1.1.7.3 Particulate Breakdown of Laser Gas

An upper limit on permissible particle size may be derived by demanding that the particles should not be permitted to exceed the melting (volatilization) temperature, which for carbon is $\sim 3800^\circ K$. Above this temperature we may anticipate breakdown of the gas from the laser radiation. Since smaller particles have a higher surface area and therefore a higher rate of cooling per unit mass, while the Mie absorption depends only on the particle mass density, it follows that particles above a certain size will be volatilized, and this has been shown experimentally at AERL to lead to breakdown.

Following the analysis of Weyl⁸ we write the particle's energy absorption rate \dot{Q} as:

$$\dot{Q} = \pi a^2 Q_{abs} \phi.$$

where a is radius, Q_{abs} Mie absorption efficiency and ϕ laser flux density. We note that for small particles $Q_{abs} \approx 2\pi a/\lambda$ in carbon.

The gas temperature T_g and solid temperature T_s then obey the following equations:

$$(\rho C_p)_s \cdot \left(\frac{4\pi}{3}\right) (a^3) \left(\frac{\partial T_s}{\partial t}\right) = \dot{Q} + \pi a^2 K \left(\frac{\partial T_g}{\partial r}\right), \quad r = a$$

and

$$(\rho C_p)_g \left(\frac{\partial T_g}{\partial t}\right) = \left(\frac{K}{r^2}\right) \left(\frac{\partial}{\partial r}\right) \left(r^2 \frac{\partial T_g}{\partial r}\right) \quad r > a$$

where ρ , C_p and K are gas density, specific heat and thermal conductivity. The solution for the solid temperature⁹ is then:

$$T_s = \frac{\dot{Q}}{4\pi a K} \left[1 - \frac{2m^2}{\pi} \int_0^\infty \frac{e^{-\chi u^2 t/a^2} du}{(u^2 - m)^2 + m^2 u^2} \right]$$

where $\chi = \frac{K}{(\rho C_p)_g}$ and $m = \frac{3(\rho C_p)_g}{(\rho C_p)_s} \ll 1$.

Thus, for long times $T_s = \dot{Q}/4\pi a K$, corresponding to heating of the air. For small times $T_s = \dot{Q}t/\frac{4\pi}{3}(\rho C_p)_s a^3$, and the intermediate region may be defined by writing

$$e^{-\chi u^2 t/a^2} = e^{-1}$$

at $u = \sqrt{m}$, where the integrand above has a minimum. Then the critical time t_c within which most of the heating has been done is:

$$\dot{Q} t_c = \dot{Q} \left(\frac{a^2}{\chi m}\right) - \frac{a^2 (\rho C_p)_s \dot{Q}}{3K}$$

now

$$t_c = \frac{4\pi a^3 (\rho C_p)_s (T_{\max} - T_0)}{3\pi a^2 Q_{\text{abs}} \cdot a}$$

Eliminating t_c between the above equations we may write the flux condition:

$$\phi_{\max} \approx \frac{4K T_{\max}}{Q_{\text{abs}} \cdot a}$$

as the maximum value of flux that may be permitted. Taking $K = 3 \times 10^{-4}$ J/cm-sec and $T_{\max} = 3000^\circ\text{K}$, calling $\frac{Q}{a} = 6000 \text{ cm}^{-1}$ for carbon we find

$$\phi_{\max} \approx \frac{6 \times 10^{-4}}{a^2} \text{ W/cm}^2 \quad (a \text{ in cm}).$$

We estimate the cavity flux for typical conditions from the integrated Rigrod equation. For

$$\phi_{\max} \approx \frac{L\phi_s (g_0 - g_c)}{L_c},$$

where L_c is the output coupling, and taking $L = 200 \text{ cm}$ and $L_c = 0.80$, while $g_0 \sim 5\%/cm$ and $g_c \sim 0.5\%/cm$, for $\phi_s = 3 \times 10^4$ we get $\phi \sim 3 \times 10^5$ for the cavity flux. From the above equations, we expect gas cooling of the solid carbon particles to be adequate provided $a < 0.5 \mu\text{m}$.

The above limit refers to the flux required to volatilize the particle. The experimental results obtained by Lencioni,¹⁰ however, indicate that the breakdown limit corresponds to much higher values, and that even particles of diameter 0.1 mm will not break down until the flux reaches $\sim 10^8 \text{ W/cm}^2$. We conclude that the only important limit on particles is that imposed by Mie scattering, as described previously.

Other particles that may be present include frozen droplets of hydrocarbon, water or intermediate combustion products. We may formally apply the same reasoning as that described above in order to define limits for H_2O and hydrocarbon ices. It is clear that since both the absorptance and refractive indices for these substances are much lower than for carbon, the heating rate will be slower, while the sublimation temperature is lower; after sublimation the vapor produced will be at so low a temperature that it is improbable that sufficient free electrons will be present to initiate breakdown. The above limits for carbon particles are therefore adequately stringent.

The Mie scattering and absorption by particles (e. g., carbon) in the laser beam leads to a requirement on the mass percentage of particles in gas. An output flux decrease of 1 percent will be produced by 0.02 percent by weight of particles in gas, and will vary approximately linearly with mass loading. Laser breakdown on particles appears very unlikely at the flux densities used here.

2.0 EXPERIMENTAL

2.1 INTRODUCTION

A number of tests were carried out on the Humdinger Junior facility with gases similar to those combustion product gases being considered for laser applications. Also, tests were conducted on an actual combustion product gas produced by Avco-Lycoming.

The general purpose of this effort was to determine whether there were any types of gas mixtures of interest for useful laser applications whose performance is significantly different from that predicted by the AERL kinetics code and not addressed during earlier work.² Also of interest is the performance of the Avco-Lycoming-produced gas with respect to that expected, as well as with respect to that of a simulated gas mixture of similar composition, but free of any impurities that could possibly degrade the performance of the actual combustion product gas mixture.

These studies indicated good agreement between measured and predicted joules/liter for most of the gas mixtures. The gas mixtures with a high CO content deviated most from the kinetic code predictions. And even here the outputs of the CO - containing gases were still good, and slightly higher than the outputs obtained in the non - CO gas mixtures under similar discharge conditions. The present results indicate that up to 12 percent CO substituted for N₂ (maximum concentration tested) does not appreciably affect the specific output (joules/liter) of the laser gas, and there may be no need to minimize the CO content of combustion product gases.

The measured output from the simulated and actual combustion product gases agreed with theoretical predictions. However, due to the 1 percent O₂ present in the actual combustion product gas the output was lower than the simulated gas mixture. This was due to the fact that O₂ is a strong attachment for electrons, thereby lowering the electron concentration in the optical volume for the same initial electron beam conditions.

The cavity and experimental arrangement are shown schematically in Figs. 9 and 10. The laser gas is circulated by fans through the heat exchangers, which are cooled by a slow or intermittent flow of LN_2 . The gas temperature is continuously monitored upstream and downstream of the discharge cavity. One of these two United Electric thermometers also regulates the gas temperature by controlling the cooling of the cold trap. The gas is typically 3 to 5°K warmer at the top of the cavity (downstream side) than below. Measurements in the cavity gave a value midway between the upstream and downstream values, and therefore the average of the two values was taken to be the initial gas temperature for these studies.

The cavity is thermally lined to reduce heat loss. The anode is aluminum, but is mounted on electrical insulators that provide reasonable thermal insulation. The cathode is made of thin titanium to reduce heat transfer to the cathode's mounting, which is not particularly well insulated thermally. The cathode has an opening 4-cm wide along its length and is covered by a 70 percent open stainless steel screen through which the E-beam can pass to ionize the gas. A Kapton foil is located just behind (on the E-beam side of) the screen which prevents gas flow into the region between the cold cathode and the warm E-beam box, and also provides an insulating dead air space in that region.

There are usually E-beam shields located upstream and downstream of the discharge cavity, spaced 4-cm apart. The anode-to-cathode spacing is also 4 cm. The mirror configuration is that of an unstable resonator laser cavity curvature produces an expansion of the beam resulting in a 40-percent feedback of the output beam and a 60-percent output coupling, giving a cavity gain (g_c) of 0.456%/cm. The mirrors are spaced 56-inches apart in a confocal configuration to produce a hollow square (40 percent hollow) beam either 3 x 3 cm (for 3-cm optics) or 4 x 4 cm (for 4-cm optics).

The beam, after passing the feedback mirror, leaves the cavity through a salt window, then goes to a convex expanding mirror located a few feet away where, after expansion to about 10 x 10 cm, it impinges on an anodized aluminum calorimeter.¹¹ The resultant calorimeter measurement of the laser output is recorded on a strip chart recorder.

Initial small signal gain measurements were made giving good agreement with predicted gains. Following that, laser output measurements were

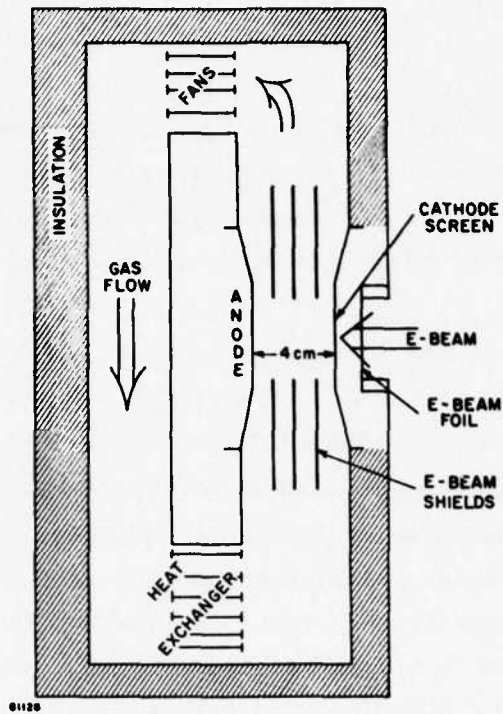


Fig. 9 Schematic of Cold Cavity Flow and Geometry.

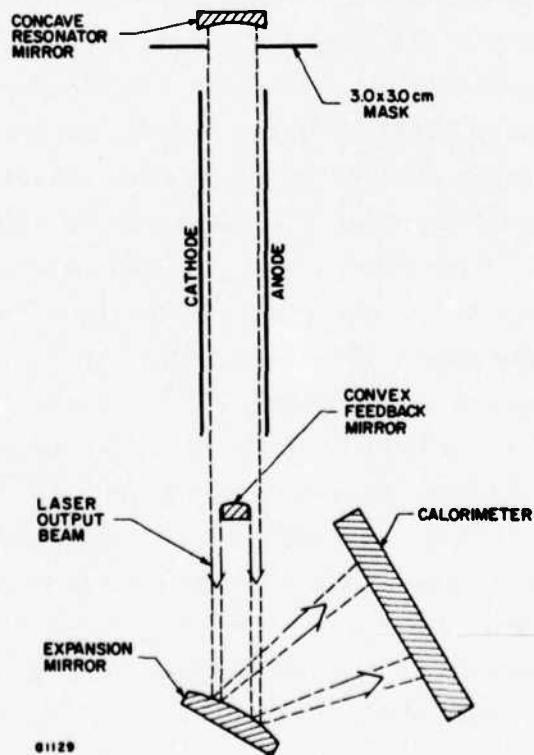


Fig. 10 Schematic of Optical Arrangement and Mask Location.

attempted using 4-cm optics; that is, optics such that the output beam completely covered the 4- x 4-cm discharge volume. Although the output was high, around 200 joules (optical volume was 1.6 liters) for an initial gas temperature of 200°K, it was still somewhat lower than the predicted value.

To avoid the possible losses due to "edge effects" (scattering of laser light off of the boundaries of the cavity, effects of refraction waves, etc.), 3-cm optics were installed in place of the 4-cm optics.

A 3 x 3-cm mask was found to be needed to further define the optical volume. When no masks were used laser light was obtained from the whole 4- x 4-cm cavity volume, rather than just the nominal central 3- x 3-cm optical volume. This extra emission was due to diffracted light from the main beam which was highly amplified in the high gain region outside the main 3- x 3-cm area. The final flux density from the outer region was comparable to (although less than) the flux density from the main 3- x 3-cm central portion.

To eliminate this extra and unwanted contribution to the output flux, a plastic mask with a 3- x 3-cm hole cut out of it was placed just in front of the large concave unstable resonator mirror, as shown in Fig. 10. This mask intercepted any diffracted light from the feedback mirror and also prevented any parasitic modes that might have otherwise run in the high gain region outside the nominal 3- x 3-cm optical volume. Any diffracted light from the edge of the mask itself was only once amplified by the factor eg^L (L the discharge length and g the gain in the area outside the 3- x 3-cm region). Without the mask, diffracted light from the feedback mirror is amplified by the square of that value, e^{2gL} , which is much more serious. The amplified diffracted light from the mask was non-consequential. Also, since the light must come from the edge of the mask on its one pass out, the extra volume of discharge swept out by the diffracted light is fairly small as compared with the volume swept out by the amplified diffracted light from the feedback mirror. With this mask carefully installed to coincide with the nominal 3- x 3-cm optical volume, an acceptably well defined output beam was obtained.

2.2 MEASUREMENTS

Preliminary data were taken in the gas mixture He:N₂:CO₂ (3:2:1) which (1) illustrated the laser performance with the 3- x 3-cm mask, (2) showed that laser action starts on the theoretically appropriate P-line and (3) obtained gain measurements indicating appropriate low temperature small signal gains. (The gain measurements were made in He:N₂:CO₂ (3:2:1), N₂:CO₂:CO:H₂ (7.76:1:0.57:0.19) and N₂:CO₂:H₂ (8.33:1:0.19).

2.2.1 Laser Performance Using He:N₂:CO₂ (3:2:1).

The laser output measurements for 3:2:1 are presented in Figs. 11 and 12. For these measurements, the 3- x 3-cm mask limits the volume over which energy is extracted to basically the 3- x 3-cm cross section.

The resultant burn pattern is shown in Fig. 11 for an initial alignment with the gas warm. The subsequent burn pattern after the gas has been cooled is also shown. These burn patterns were taken on 3M Premium Transparency Infrared Film (Type 577) and show that some energy appears outside the nominal 3- x 3-cm area (probably due to diffraction off the edge of the mask), but not too great an amount. If the burn pattern is taken on the other side of the transparency film, the less sensitive side, then only the shape of the bright part of the beam is seen, as shown in the rightmost burn pattern of Fig. 11.

In computing the specific output, the nominal 3- x 3-cm cross section is used for the volume from which energy is extracted. Any light scattered outside the 3- x 3-cm area by diffraction off the edge of the mask or by density fluctuations in the gas would be amplified on the way out, and both the scattered light and any increase due to amplification would be recorded by the calorimeter. An appropriate correction would be to subtract the amplified portion of such scattered light as it represents energy extracted from the volume outside the nominal volume of 3- x 3-cm cross section. No such correction was made for these runs because it represents less than 10 percent of the total energy as determined by the addition of a stripper.

Laser output measurements corresponding to the burn patterns and the computed specific outputs are shown in Fig. 11 and the experimental and predicted values are plotted against E/N in Fig. 12. The diffusely scattered radiation measured with a gold-doped germanium detector from

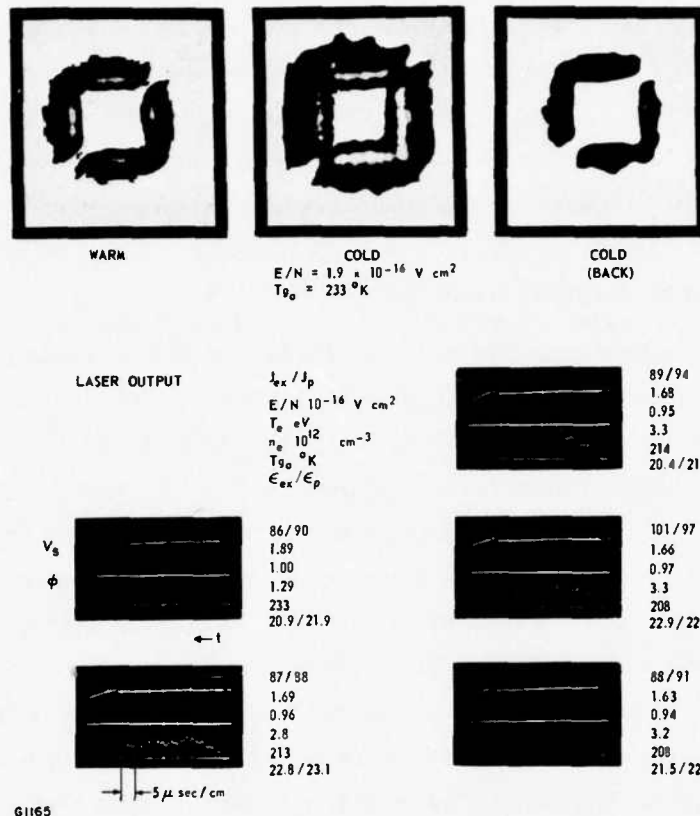


Fig. 11 Burn Patterns and Laser Output for the Gas Mixture He: N₂: CO₂: CO: H₂ (3: 2: 1: 0: 0) at Low Temperature. The output flux ϕ (in arbitrary units) is shown along with the corresponding trace of the sustainer voltage V_s . The downward dip of the voltage trace indicates the start of the E-beam and initiation of the discharge current, while the positive inductance kick of V_s indicates the turn-off of the E-beam and corresponding discharge current. Time runs right to left for these traces and the sweep speed is $5 \mu\text{sec}/\text{cm}$. The shape of the ϕ signal is a rough measure of the time history of the output flux; the shape varies somewhat with the position of the detector, suggesting that some of the spikiness may be due more to a localized spacial fluctuation in the flux than to a fluctuation in the overall laser output. The experimental and predicted specific outputs, J/l_{ex} and J/l_p , and efficiencies, ϵ_{ex} and ϵ_p , are given along with the electric field per unit density (E/N), the electron average energy T_e , the peak value of the electron density n_e and the initial gas temperature T_{g0} . The efficiency number is based on the specific energy input in the optical volume and does not include edge effect inefficiencies.

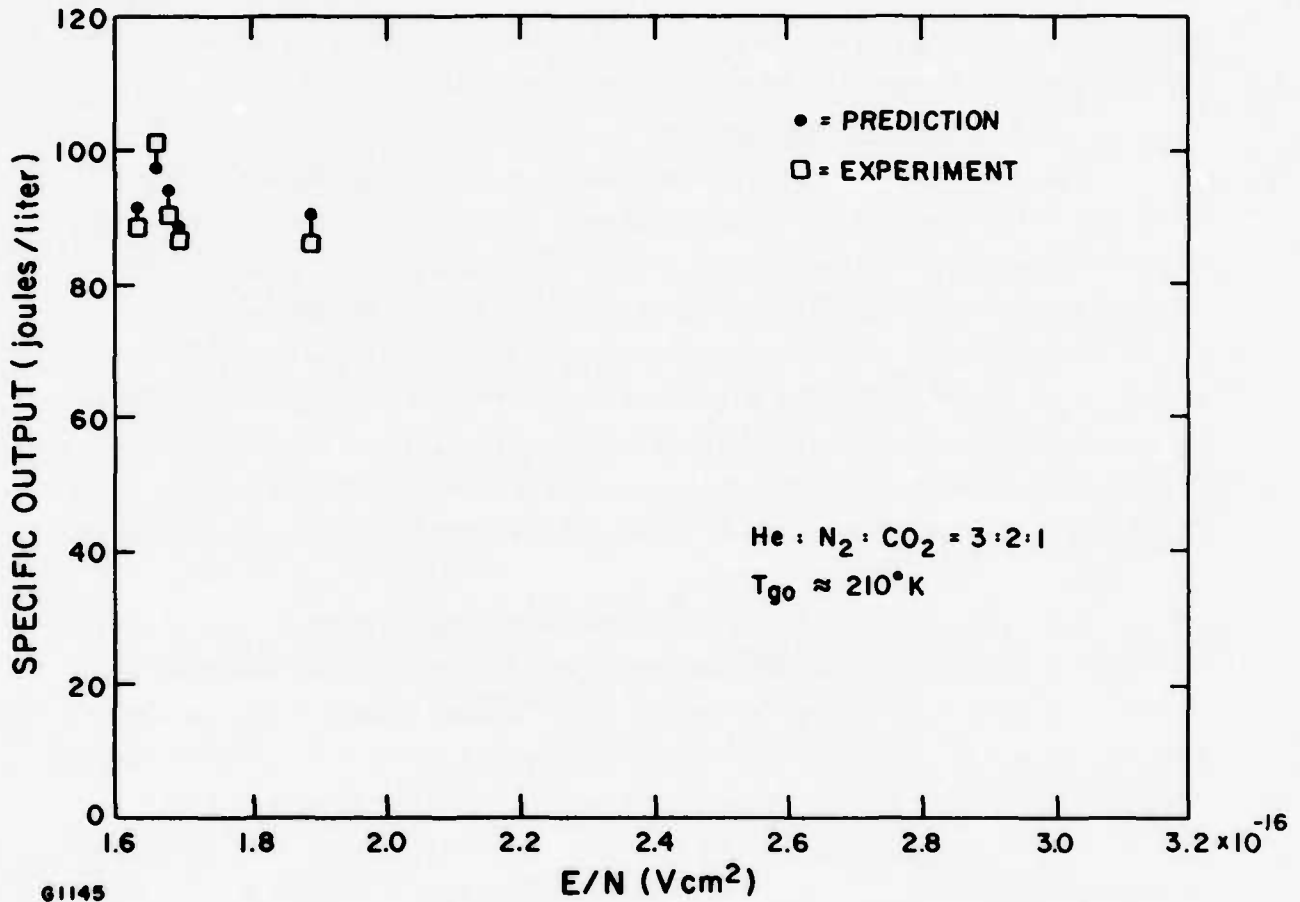


Fig. 12 Experimental and Predicted Values of Specific Output Plotted Against Electric Field Per Unit Density (E/N) for He: N₂: CO₂: CO: H₂ (3: 2: 1: 0: 0) at Low Temperature.

the surface of the calorimeter was used to measure the laser output flux as a function of time.

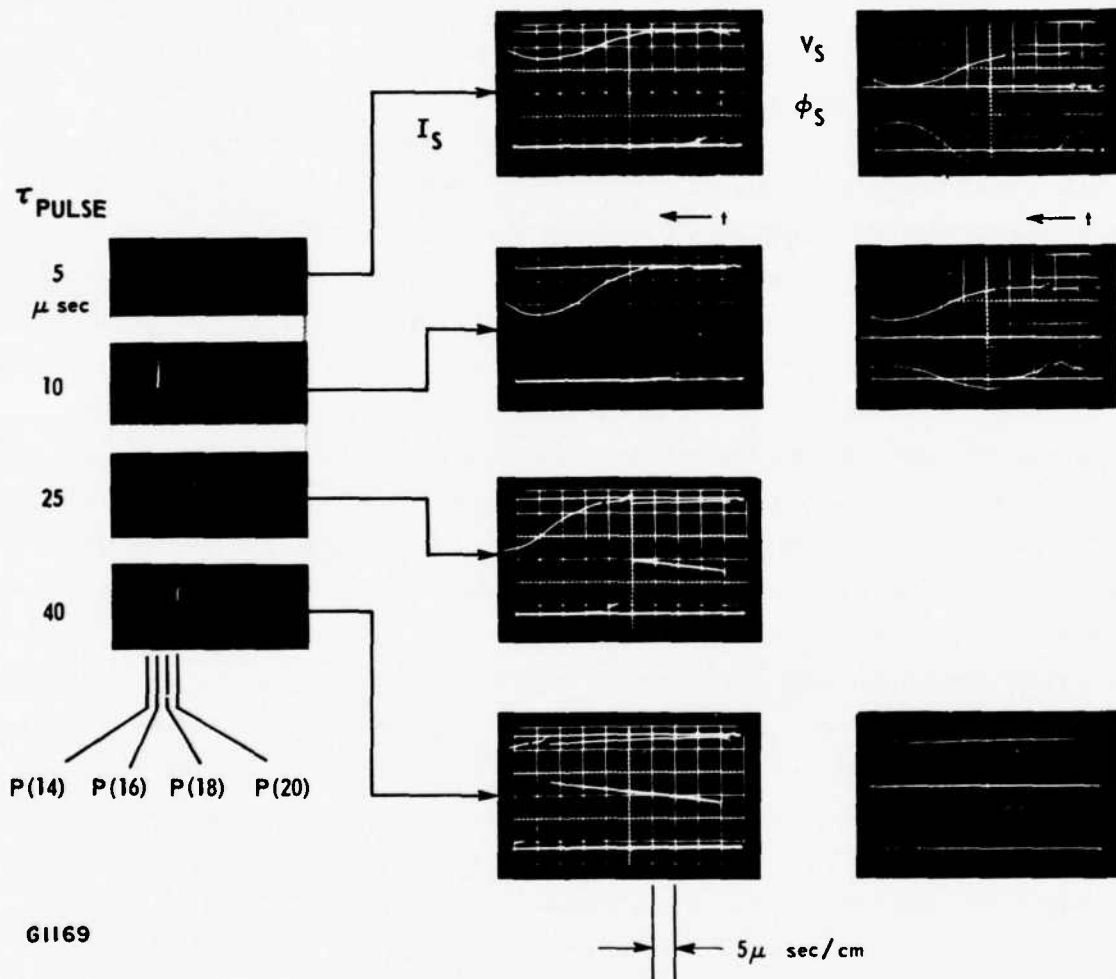
These measured values in He:N₂:CO₂ (3:2:1) agreed well with the theoretical values. The theoretical predictions were computed with the AERL kinetic code 2 using the actual measured time histories of the sustainer voltage and sustainer current as inputs to the code.

2.2.2 P-Line Measurements

Experiments were performed using a spectrum analyzer to determine the P-lines on which lasing occurred. It has generally been observed in the past that for lasers starting at room temperature most of the lasing usually occurs on the P(20) transition. This is due to the extra gain for the P(20) wavelength that is contributed by a matching "hot band" line of the 011→110 transition. The argument is that for a reasonably high bending mode population enough extra gain is added to the gain of the P(20) line of the 001→100 transition to keep the net gain for that wavelength higher than the gain for the neighboring lines (e. g., P(18), P(22)) over a large temperature range.

However, for cold initial temperatures, the optimal P-line is fairly far from P(20). Also, the bending mode population is lower than that for 300°K operation so that the "hot band" contribution to help P(20) should be lower. Thus for cold initial gas temperatures, a more "classical" behavior is expected with respect to the P-lines on which lasing occurs. This appears to be the case, as shown by the data of Fig. 13 where data were taken at pulse widths of 5, 10, 25, and 50 μsec. This was accomplished by turning off the E-beam at the appropriate times. During each run the laser output pulse went into a spectrum analyzer with the usual phosphorescent screen replaced by unexposed Polaroid film. The burn marks on the film indicated which P-transitions ran during the pulse.

The burn marks and corresponding voltage, current, and flux traces are shown in Fig. 13. The gas was He:N₂:CO₂ (3:2:1) at 215°K. The measurements were consistent with the kinetics code 2 assumption that lasing occurs on the line with the maximum gain. For an initial gas temperature of 215°K, the transition that has the maximum gain is P(14). As predicted, measurements showed P(14) was the main transition observed for a 5-μsec pulse with a faint trace of P(16). For a 10-μsec pulse, only P(14) and P(16) were observed with a weak indication of P(18), presumably



G1169

Fig. 13 Spectrum Analyzer Measurements of Laser Output at $T_{g0} = 215^{\circ}\text{K}$, for Pulse Durations of 5, 10, 25 and 50 μsec . Corresponding flux outputs and voltage and current traces are shown along with the burn marks indicating the output from transitions P(14) through P(20) during the pulse time.

occurring near the end of the pulse. The 40- μ sec pulse width data showed all four lines, P(14), P(16), P(18), and P(20). However, it appeared that P(18) did not run long relative to the other lines. Possibly the P(20) line comes on early, because of the "enhanced" gain for the P(20) wavelength once the bending mode population has built up.

2.2.3 Gain Measurements

Initial gain measurements were made in three gas mixtures to check on the consistency between prediction and experiment. The small signal gain measurements agreed well with predictions as did the He:N₂:CO₂ (3:2:1) laser output measurements and the P-line measurements. These gain measurements, because of the good agreement, add to the credibility of the laser output measurements.

Gain measurements for the gas mixture He:N₂:CO₂ (3:2:1) are shown in Fig. 14, where the measured gain g (percent/cm) is shown as a function of time along with the corresponding predicted value. Results for three different initial temperatures are shown. The measurements were made using a five-watt CO₂ laser beam which propagated along the optical axis in the center of the discharge. The beam flux was measured by a gold-doped germanium detector both before and during the discharge. The observed increase in flux thereby gives the build-up of gain as a function of time from the initiation of the discharge at $t = 0$. The He:N₂:CO₂ (3:2:1) measurements showed good agreement between predictions and experiments. Small signal gain measurements were also obtained in gas mixtures N₂:CO₂:H₂ (8.33:1:0.19) and N₂:CO₂:H₂ (7.8:1:0.57:0.19) as shown in Figs. 15 and 16. As seen from these figures, the agreement between predictions and experiments was quite good for these gases, with the exception of the room temperature run for the 8.33:1:0.19 gas mixture, which only showed the only significant discrepancy. Since the measured small signal gain results agreed well with the predicted values, measurements of laser output could be performed with increased certainty of obtaining predicted outputs.

2.3 LASER OUTPUT MEASUREMENTS

Laser output data were obtained using the 3- x 3-cm mask configuration for several groups of gas mixtures. The laser gases tested

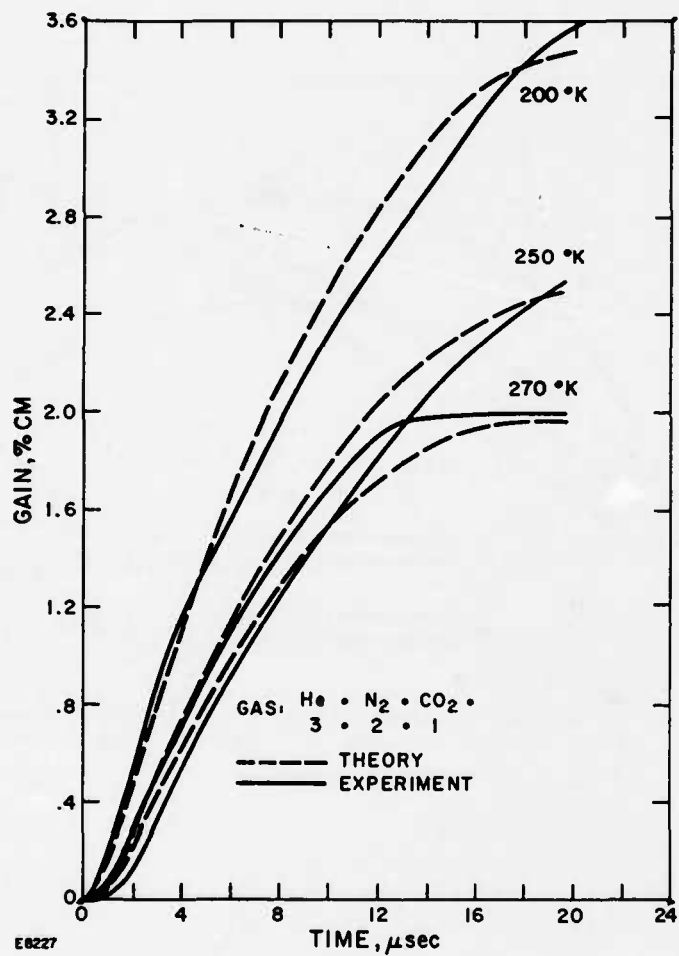


Fig. 14 Measured and Predicted Small Signal Gains $g(\text{cm}^{-1})$ as a Function of Time During the Discharge for He: N₂: CO₂ at Low Initial Gas Temperature and at Room Temperature.

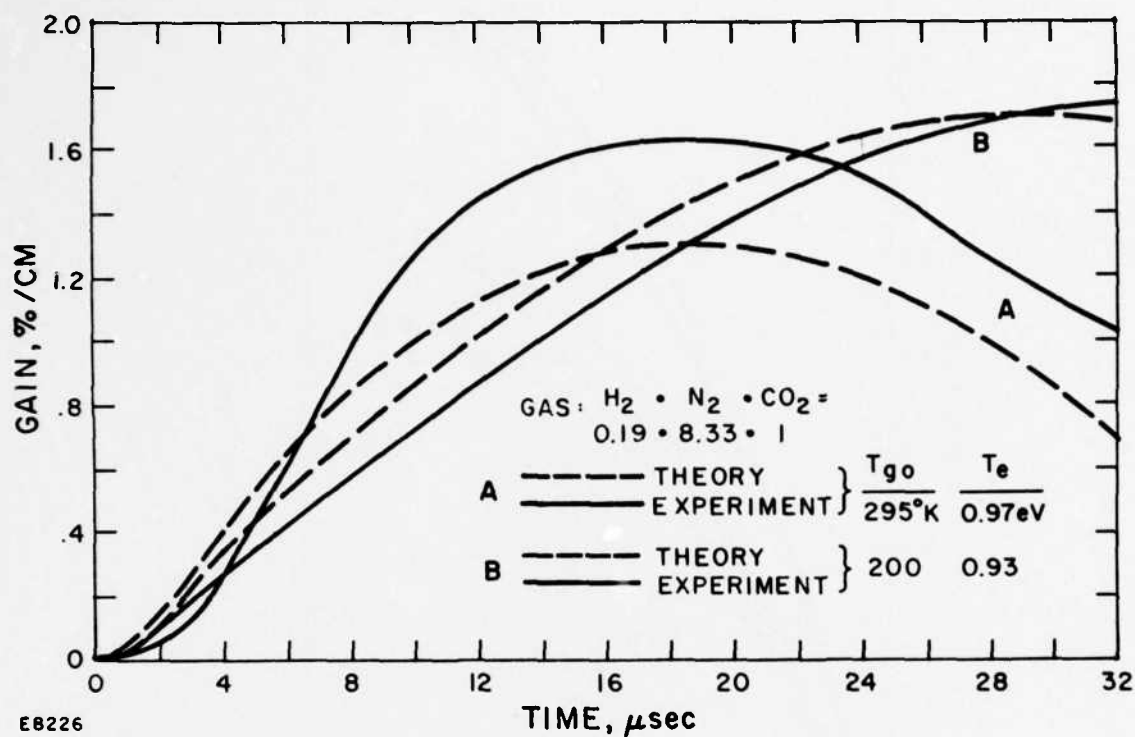


Fig. 15 Measured and Predicted Small Signal Gains for $N_2:CO_2:CO:H_2$ (8.33:1:0:0.19).

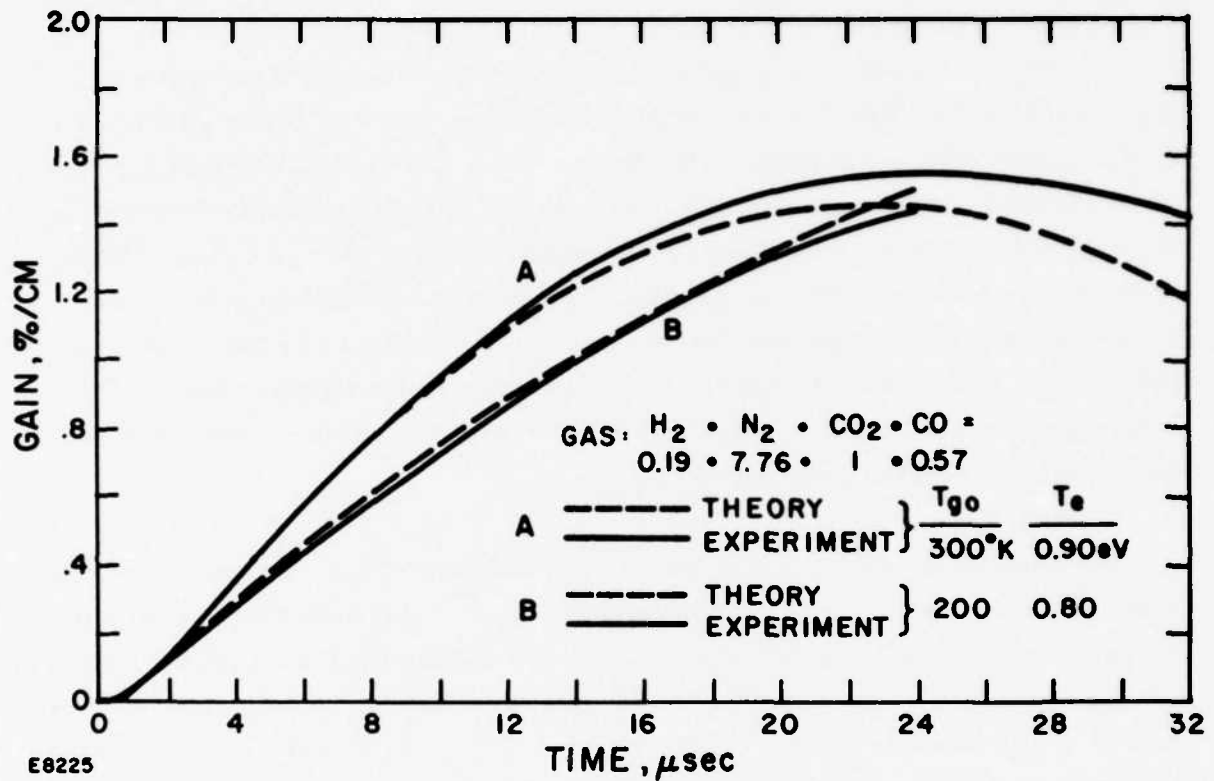


Fig. 16 Measured and Predicted Small Signal Gains for N₂: CO₂: CO: H₂ (7.8: 1: 0.57: 0.19).

within each group are given in Table 1. The corresponding initial gas temperatures T_{g0} , electron densities n_e , electron temperature T_e , and electric field-to-particle density ratios E/N are also given. The data for the gases in each group are given in the figures described below.

The data in the accompanying figures for each gas show some of the corresponding flux traces. Superimposed on some of these flux traces is the predicted time history of the output flux. The predicted curve has been scaled to have the same output/cm as the experimental curve; that is, the ratio of the area under the experimental curve to the area under theory curve is the same as the corresponding ratio of measured output to theoretical output. In comparing the two curves the measured onset time for the start of lasing usually agrees well with the predicted onset time. This indicates that the pumping rates and rate of gain buildup are in good agreement with the kinetic code predictions.

2.3.1 Group I

The He:N₂:CO₂ (3:2:1) gas mixture data of Fig. 11 showed reasonable agreement with the kinetic code predictions. Similar low temperature measurements with a 21 percent CO₂ content mixture with 2 percent replacing the He in the gas mixture also showed good agreement. The data are shown in Fig. 17 for the mixture N₂:CO₂:H₂ (3.67:1:0.19) run at an initial temperature of 215°K. The burn patterns are shown for several of the runs along with the corresponding flux measurements. The corresponding plot of measured output vs E/N for these data are shown in Fig. 18, where E is the electric field and N is the particle density. Note there is good agreement of experimental data with the predictions over the range of E/N values.

Data and corresponding burn patterns taken at an initial gas temperature of 215°K for the gas mixture N₂:CO₂:CO:H₂ (7.76:1:0.571:0.095) are shown in Fig. 19. The measured outputs and the corresponding predictions are shown as a function of E/N in Fig. 20. Here the agreement with theory is not as good. The measured values are 12 to 20 percent lower than the values predicted. The cause of this discrepancy is not known. It is believed that the code is not properly handling the CO molecule in either the pumping, deactivation or V-V transfer rates. Checks have been made

TABLE I
LASER CASES TESTED

Gas (He:N ₂ :CO ₂ :CO:H ₂)	T _{g0} (°K)	n_e (10 ¹² cm ⁻³)	T _e (eV)	E/N (10 ⁻¹⁶ x cm ²)
<u>GROUP I</u>				
3:2:1:0:0	210	2.8-3.3	0.95-1.00	1.66-1.89
0:3.67:1:0:0.095	208-233	2.5-4.1	0.82-0.98	1.65-2.54
0:7.76:1:0.571:0.095	211-217	5.0-5.7	0.88-0.92	2.13-2.46
0:8.33:1:0:0.19	210-214	5.6-6.5	0.98-1.01	2.16-2.42
213				
<u>GROUP II</u>				
0:8.33:1:0:0.19	300	4.2-4.7	0.99-1.02	2.26-2.64
0:16.4:1:0:0.36	300	5.2-5.5	1.00-1.03	2.26-2.44
0:7.19:1:1.14:0.19	300	4.1-4.5	0.86-0.87	2.44-2.65
0:8.33:1:0:0.19	235	3.8-4.6	1.00-1.02	2.29-2.52
<u>GROUP III</u>				
0:8.33:1:0:0.095	300	3.6-5.1	0.98-1.04	2.11-2.88
0:8.33:1:0:0.19	300	3.8-5.8	0.99-1.03	2.06-2.07
0:8.33:1:0:0.31	300	4.7-5.4	0.99-1.02	2.29-2.53
0:16.4:1:0:0.36	300	5.4-5.9	1.0-1.02	2.05-2.39
<u>GROUP IV - Avco-Lycoming Produced Combustion Gas</u>				
0:6.2:1:0.20:0.11 (Actual)	300	2.4-2.8	0.97-1.03	2.58-3.20
0:6.2:1:0.20:0.11 (Simulated)	300	3.6-4.4	0.93-1.01	2.21-2.95
0:6.2:1:0.20:0.11 (Actual)	220	2.5-3.2	0.96-0.99	2.47-2.78
0:6.2:1:0.20:0.11 (Simulated)	220	3.6-4.1	0.95-0.96	2.40-2.51
<u>GROUP V - Avco-Lycoming Produced Combustion Gas</u>				
0:6.2:1:0.20:0.098 (Actual)	208-233	2.0-2.8	0.94-0.99	2.29-2.73
0:6.2:1:0.20:0.098 (Actual)	300	1.7-2.0	0.97-1.03	2.53-3.14
0:6.2:1:0.20:0.098 (Actual)	233-256	2.6-3.9	0.97-1.02	2.61-3.03



$E/N = 1.65 \times 10^{-16} \text{ V cm}^2$
 $T_{g_0} = 216 \text{ }^\circ\text{K}$



1.89
211



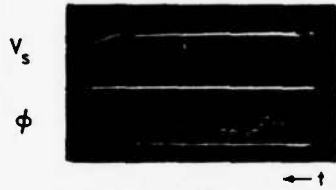
2.30
214

LASER OUTPUT

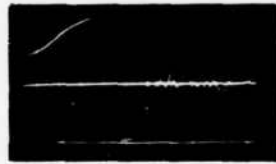
J_{ex}/J_p
 $E/N \text{ } 10^{-16} \text{ V cm}^2$
 $T_e \text{ eV}$
 $n_e \text{ } 10^{-12} \text{ cm}^3$
 $T_{g_0} \text{ }^\circ\text{K}$
 ϵ_{ex}/ϵ_p



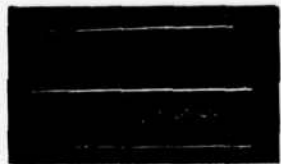
83/80
2.09
0.92
3.2
214
24.1/23.2



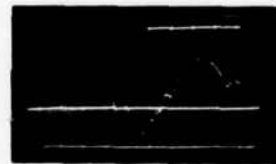
48/53
1.65
0.82
2.5
216
15.8/17.5



91/96
2.30
0.95
3.5
214
22.1/23.3



73/79
1.89
0.88
3.2
211
16.9/18.3



114/122
2.54
0.98
4.1
217
20.7/22.2

G1164

$\rightarrow \leftarrow 5 \mu \text{ sec/cm}$

Fig. 17 Laser Output for $\text{N}_2:\text{CO}_2:\text{CO}:\text{H}_2$ (3.67:1:0:0.19) at Low Temperature.

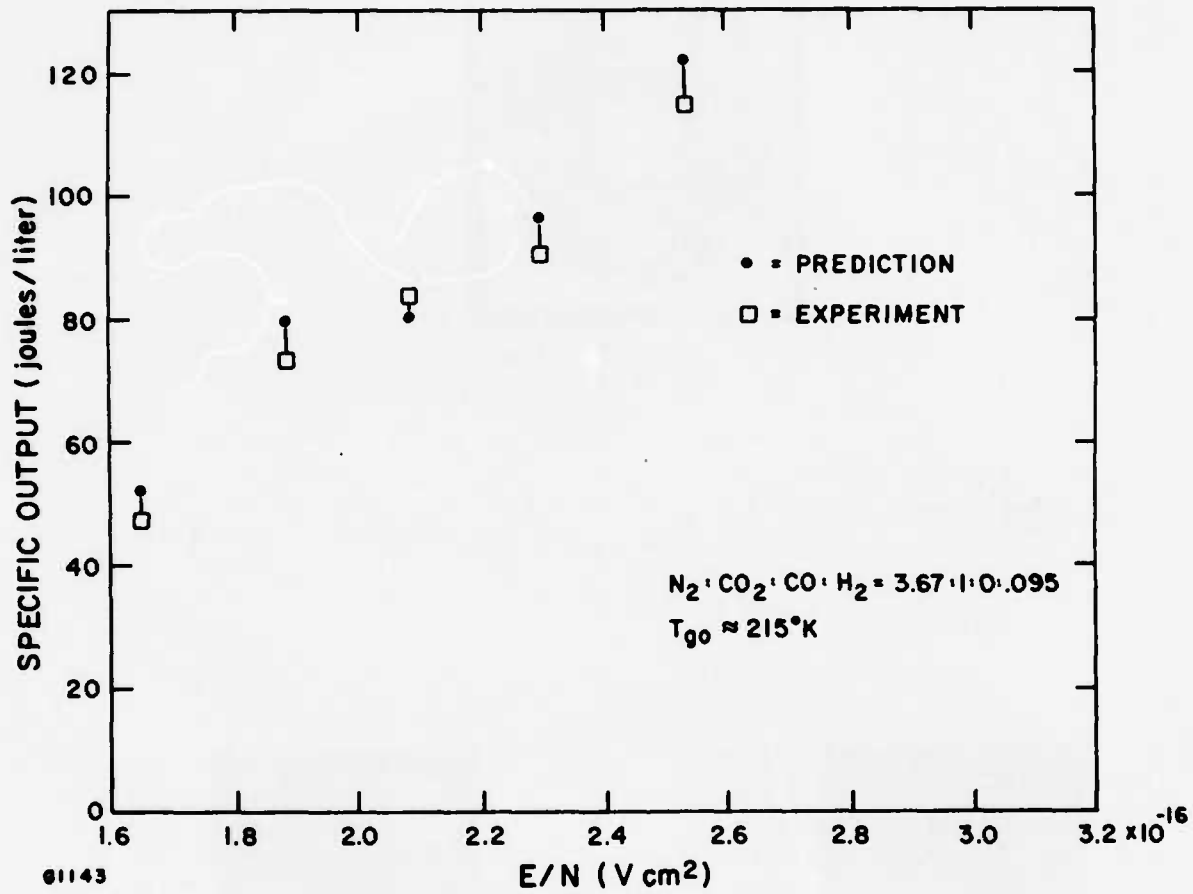


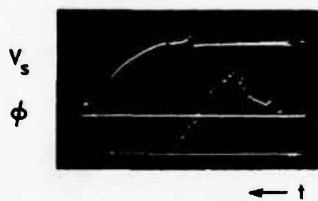
Fig. 18 Experimental and Predicted Values of Specific Output vs E/N for $N_2:CO_2:CO:H_2$ (3.67:1:0:0.19) at Low Temperature.



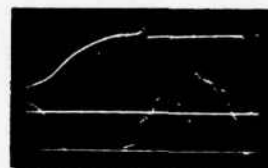
$E/N = 2.30 \times 10^{-16} \text{ V cm}^2$
 $T_{g_0} = 210 \text{ }^\circ\text{K}$

LASER OUTPUT

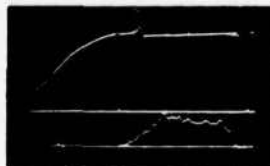
J_{ex}/J_p
 $E/N \text{ } 10^{-16} \text{ V cm}^2$
 $T_e \text{ eV}$
 $n_e \text{ } 10^{-12} \text{ cm}^{-3}$
 $T_{g_0} \text{ }^\circ\text{K}$
 ϵ_{ex}/ϵ_p



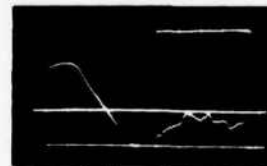
100/123
 2.13
 0.88
 5.3
 210
 19.1/23.5



110/122
 2.29
 0.90
 5.0
 212
 21.9/24.3



102/130
 2.30
 0.90
 5.1
 210
 18.4/23.5

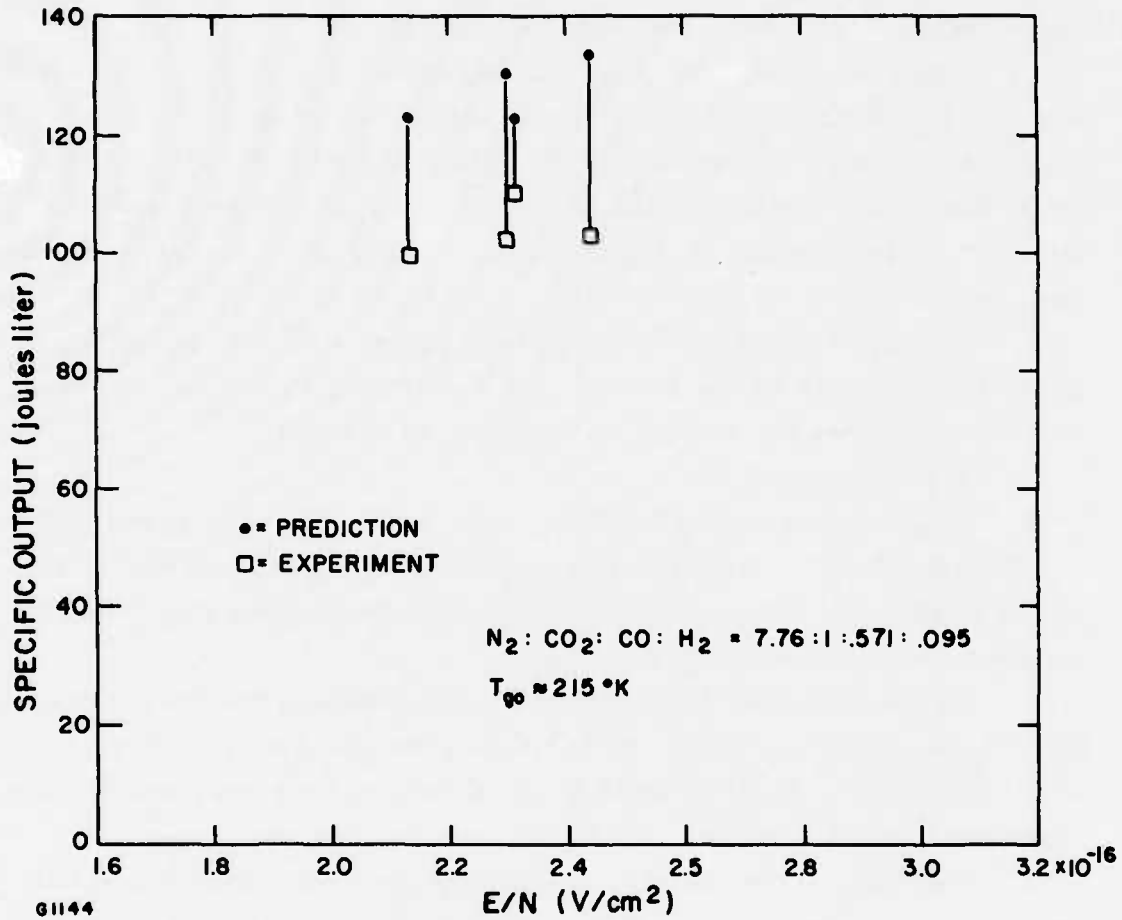


103/134
 2.46
 0.92
 5.7
 214
 17.8/23.1

G1163

5 μ sec/cm

Fig. 19 Laser Output for $N_2:CO_2:CO:H_2$ (7.76:1:0:571:0.095) at Low Temperature.



61144

Fig. 20 Experimental and Predicted Values of Specific Output vs E/N for $N_2 : CO_2 : CO : H_2$ (7.76:1:0.571:0.095) at Low Temperature.

on possible inaccuracies in CO rates, but no substantial corrections have yet been found. A similar predicted experimental discrepancy is found below for the CO mixture containing 12 percent CO.

The flux traces and corresponding burn patterns for the gas mixture $N_2:CO_2:H_2$ (8.33:1:0.19) at low temperature are shown in Fig. 21. The predicted and experimental values are plotted against E/N in Fig. 22. The predicted experimental agreement is fair. The discrepancy between predictions and experiment in this CO_2 lean mixture is about 1/2 to 2/3 that seen for the 6 percent CO mixture.

The onset times for lasing agreed rather well with prediction, as is shown in Fig. 23 by the overlay of the predicted flux time history on the measured ϕ signal for several of the gases of Group I.

2.3.2 Group II

Representative data including burn patterns for the gas mixture $N_2:CO_2:H_2$ (8.33:1:0.19) run at an initial gas temperature of $300^\circ K$ are shown in Fig. 24. The comparison of experimental data with prediction shows good agreement, see Fig. 25.

Reasonably good agreement was also obtained for the gas mixture $N_2:CO_2:H_2$ (16.4:1:0.36) at an initial gas temperature of $300^\circ K$, see Figs. 26 and 27. Again there is good agreement between predictions and experiment.

Representative flux traces and burn patterns are shown in Fig. 28 for the gas mixture $N_2:CO_2:CO:H_2$ (7.2:1:1.14:0.19) which contains 12 percent CO. The measured and theoretical output values plotted as a function of E/N are shown in Fig. 29. The measured values are about 25 percent below the predicted values. This is a considerably larger discrepancy than the usual 5- to 10-percent variance seen for the other gases. It should be noted that the data for the gases tested just before and just after this mixture containing 12-percent CO all agreed reasonably well with theory. The experimental arrangement and conditions were the same. This discrepancy in the 12-percent CO data appears to be real and not an experimental artifact.

The cause of this discrepancy is not clear, but as before the kinetic code 2 may be improperly handling the CO molecule. The possibility of an



$E/N = 2.32 \times 10^{-16} \text{ V cm}^2$
 $T_{go} = 213^\circ\text{K}$

LASER OUTPUT

J_{ex}/J_p
 $E/N \text{ } 10^{-16} \text{ V cm}^2$
 $T_e \text{ eV}$
 $n_e \text{ } 10^{-12} \text{ cm}^3$
 $T_{go} \text{ } ^\circ\text{K}$
 ϵ_{ex}/ϵ_p

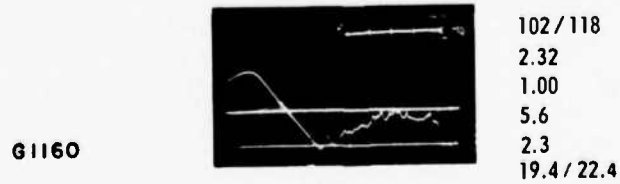
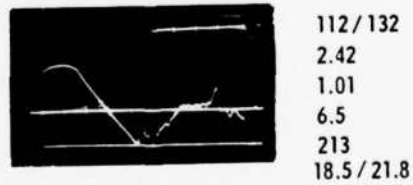
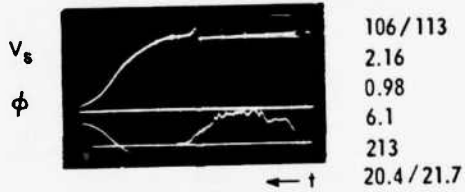


Fig. 21 Laser Output for $N_2:CO_2:CO:H_2$ (8. 22: 1: 0: 0. 19) at Low Temperature.

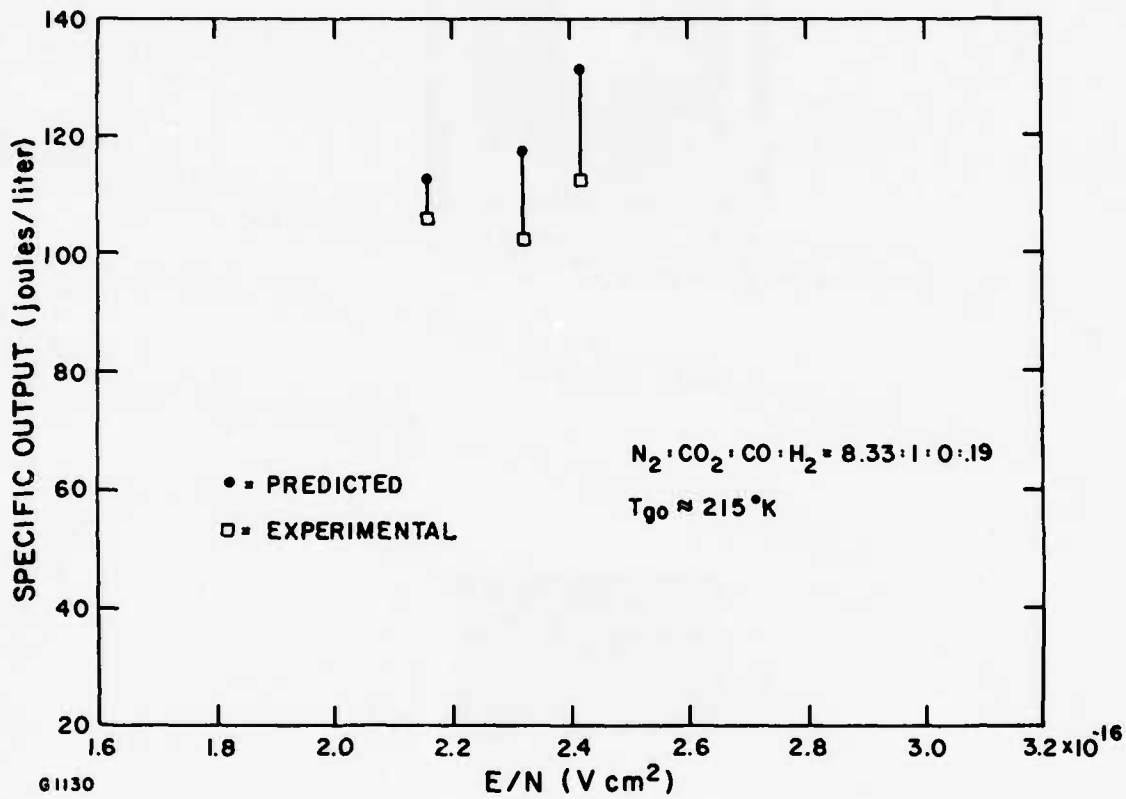


Fig. 22 Experimental and Predicted Values of Specific Output vs E/N for $N_2 : CO_2 : CO : H_2$ (8.33:1:0:0.19) at Low Temperature.

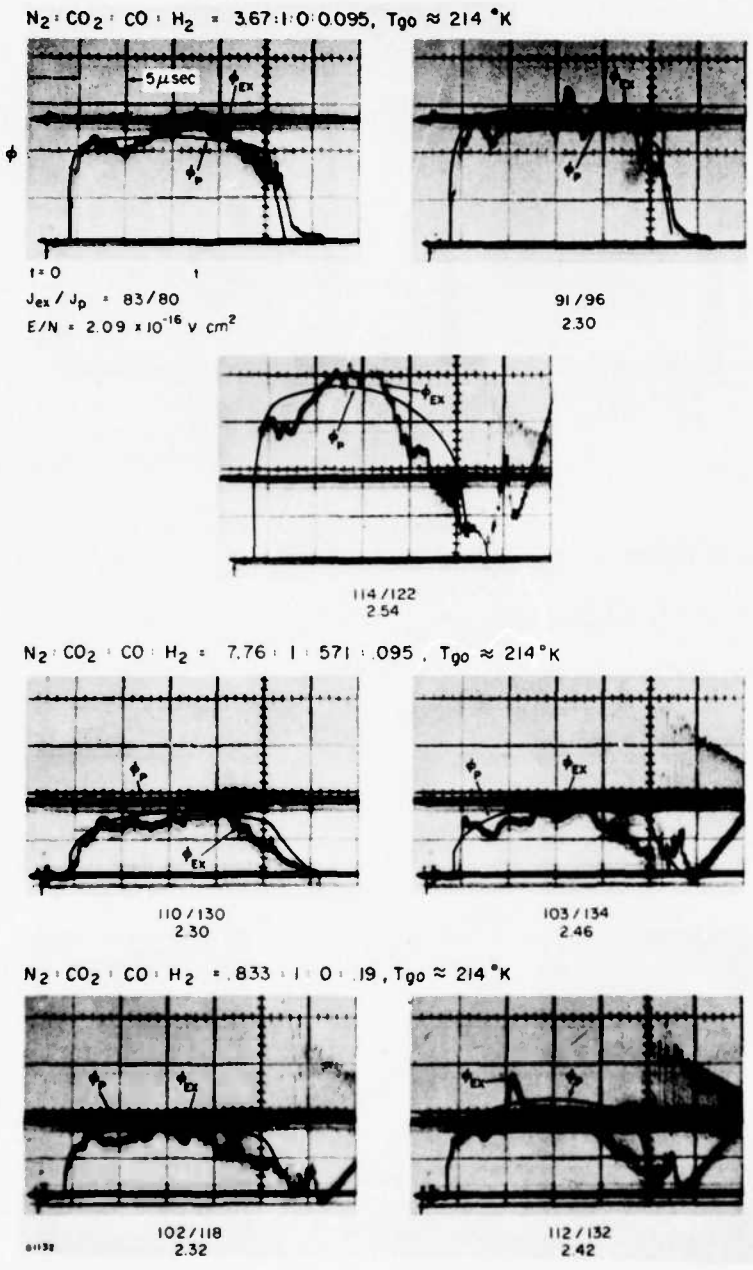


Fig. 23 Measured and Predicted Flux Onset Times and Flux Time Histories for Representative Cases of the Gas Mixtures $N_2 : CO_2 : CO : H_2$ (3.67: 1: 0: 0.095), (7.76: 1: 0.571: 0.059), and (8.33: 1: 0: 0.19) at Low Temperature. The predicted flux history (smooth curve) has been scaled such that the areas under the predicted and measured curves correspond to the respective predicted and measured specific outputs. Corresponding T_e and experimental and predicted specific outputs (J/l_{ex} and J/l_p) are also shown.



E/N $1.99 \times 10^{-16} \text{ V cm}^2$
 T_{g_0} $300 \text{ }^\circ\text{K}$



2.64
 300

LASER OUTPUT

J_{ex}/J_p
 E/N 10^{-16} V cm^2
 T_e eV
 n_e 10^{-12} cm^3

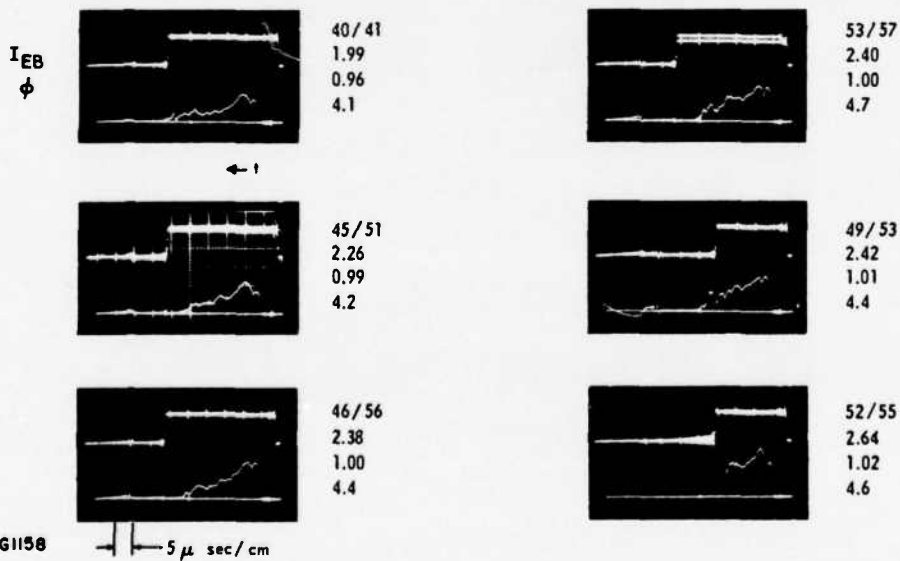


Fig. 24

Laser Output for $N_2:CO_2:CO:H_2$ (8.33:1:0:0.19) at Room Temperature. The output flux ϕ , giving approximately the time history of the laser output flux, is shown here along with the E-beam current T_{eb} , the duration of which determines the duration of the discharge. Time runs right to left at $5 \mu\text{sec/cm}$, and J/l_{ex} and J/l_p are the measured and predicted specific outputs, respectively.

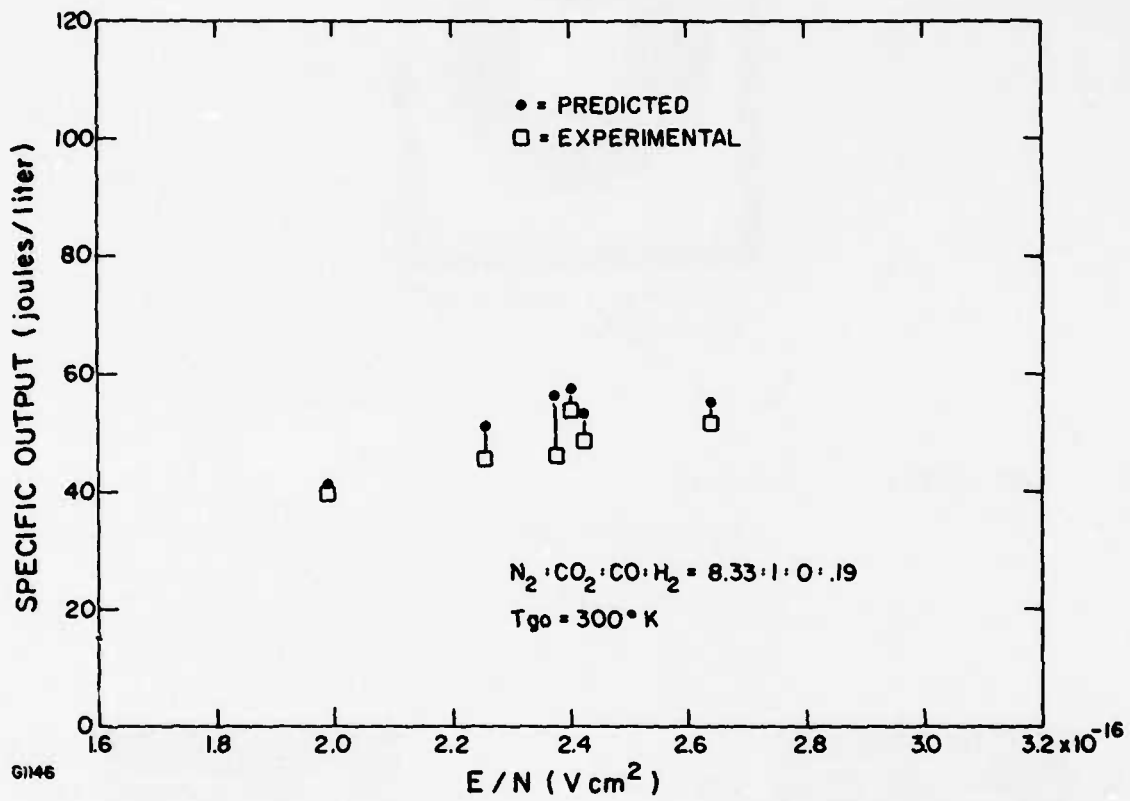


Fig. 25 Experimental and Predicted Values of Specific Output vs E/N for $N_2 : CO_2 : CO : H_2$ at Room Temperature.



$E/N = 2.26 \times 10^{-16} \text{ V cm}^2$
 $T_{g_0} = 300 \text{ }^\circ\text{K}$

LASER OUTPUT

J_{ex}/J_p
 $E/N \text{ } 10^{-16} \text{ V cm}^2$
 $T_e \text{ eV}$
 $n_e \text{ } 10^{-12} \text{ cm}^3$

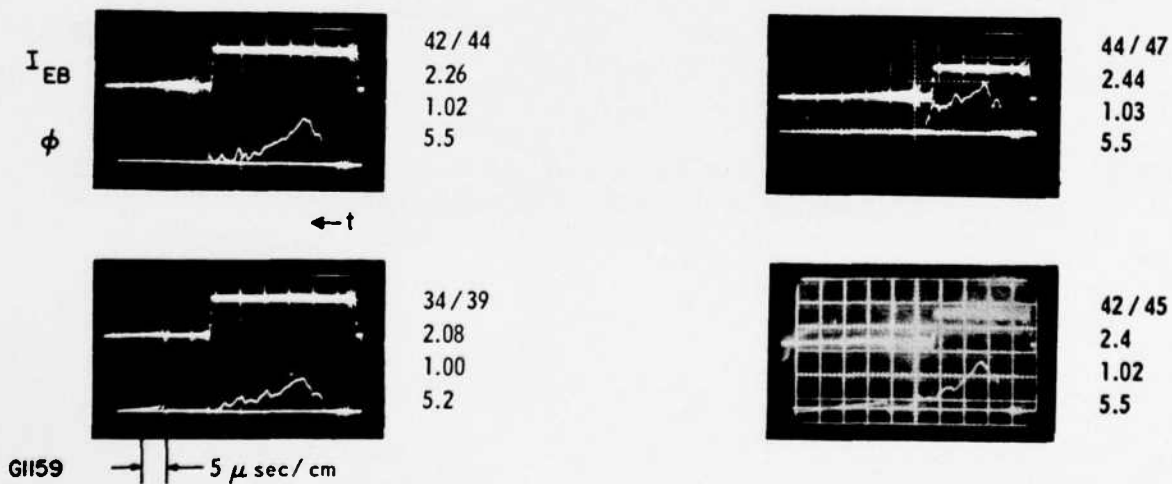


Fig. 26 Laser Output for $N_2:CO_2:CO:H_2$ (16.4:1:0:0.36) at Room Temperature.

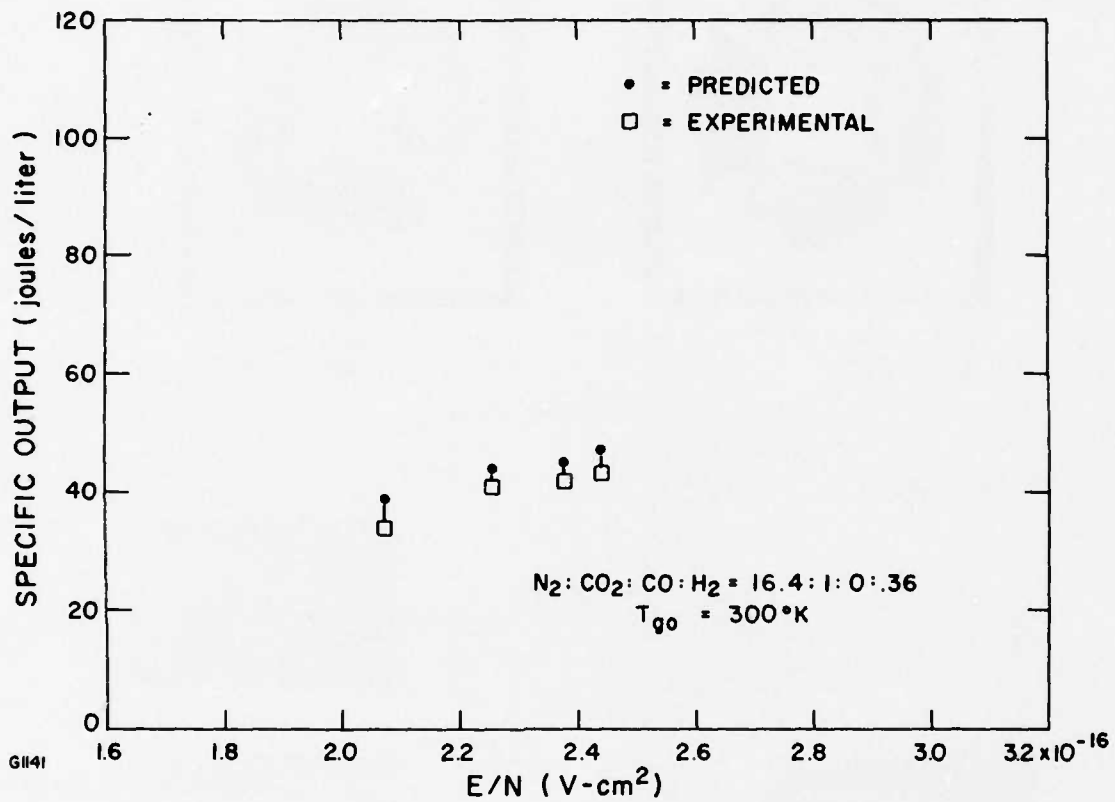


Fig. 27 Experimental and Predicted Values of Specific Output vs E/N for $N_2:CO_2:CO:H_2$ (16.4:1:0:0.36) at Room Temperature.



$E/N = 2.45 \times 10^{-16} \text{ V cm}^2$
 $T_{g_0} = 300^\circ\text{K}$

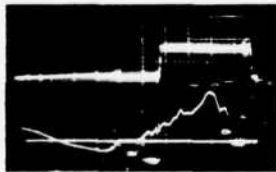


2.51
 300

LASER OUTPUT

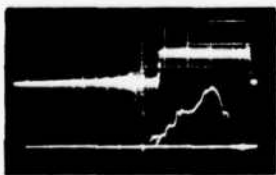
J_{ex}/J_p
 $E/N \ 10^{-16} \text{ V cm}^2$
 $T_e \ \text{eV}$
 $n_e \ 10^{-12} \text{ cm}^3$

I_{EB}
 ϕ

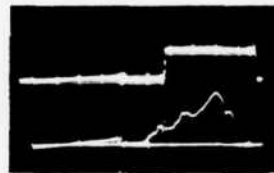


53/66
 2.45
 0.86
 4.1

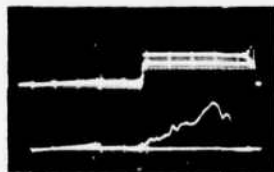
← t



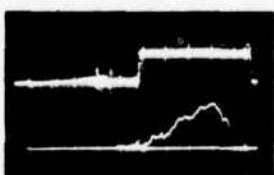
58/74
 2.65
 0.89
 4.5



54/70
 2.54
 0.87
 4.1



50/70
 2.44
 0.86
 4.1



57/73
 2.51
 0.87
 4.3

5 μ sec/cm

G1161

Fig. 28 Laser Output for $N_2:CO_2:CO:H_2$ (7.2:1:1.14:0.19) at Room Temperature.

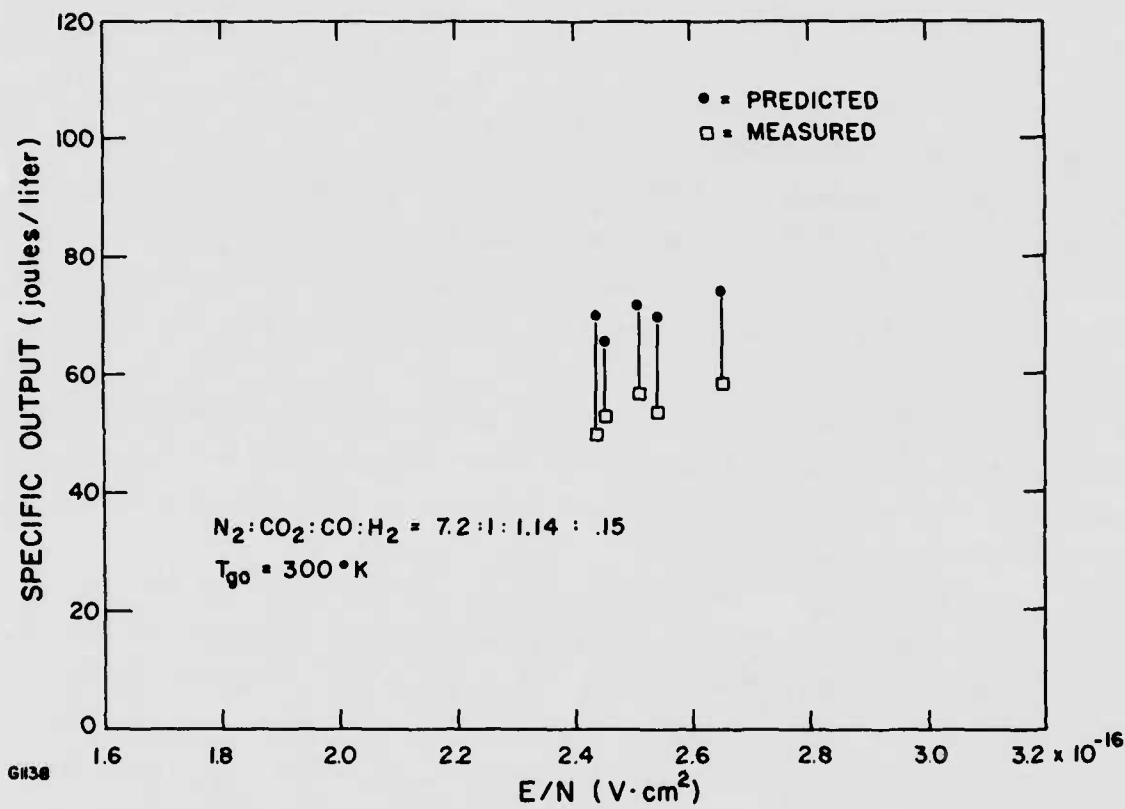


Fig. 29 Experimental and Predicted Values of Specific Output E/N for $N_2:CO_2:CO:H_2$ (7.2:1:1.14:0.19) at Room Temperature.

error in the H_2 deactivation rate existed. Nearly a factor-of-two error in the bending mode deactivation rate would be required to explain the data for this gas mixture. However, changing the H_2 deactivation rate by the indicated factor of two was inconsistent with the data for the non-CO-containing gas mixtures. This indicated the problem was not with the H_2 deactivation rate, but with CO kinetics.

The gas mixture $N_2:CO_2:H_2$ (8.33:1:0.19) data for initial gas temperatures of about $235^\circ K$ are shown in Fig. 30. Data and predictions are plotted against E/N in Fig. 31. The agreement with predictions is rather good and is similar to the previous results at $213^\circ K$ for this gas (in Group I) shown in Fig. 22.

Again the onset times for lasing agreed rather well with the predicted onset times, as shown in Fig. 32 for a number of cases from the gases of Group II. Perhaps not coincidentally, the largest discrepancy was for the 12-percent CO mixture.

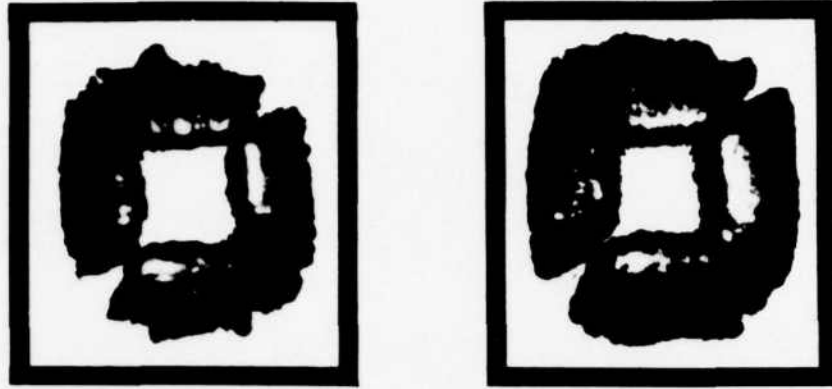
2.3.3 Group III

The data in this group were taken with the same experimental arrangement as the above data; however, it was found at the end of this sequence that about 20 percent of the laser beam was not reaching the calorimeter. The problem was corrected and a repeat of the runs was made in order to determine the appropriate correction factor to be applied to the data.

Laser output data at room temperature were taken for gases with 10.5-percent CO_2 and varying amounts of H_2 . The measured outputs for a 1-percent H_2 mixture, $N_2:CO_2:H_2$ (8.33:1:0.095) are shown as a function of E/N in Fig. 33 along with the corresponding values predicted by the kinetic code.

The measured laser outputs and corresponding predicted values for the 2-percent H_2 mixture $N_2:CO_2:H_2$ (8.33:1:0.19) are given vs E/N in Fig. 34, and measured and predicted values for the 3.3-percent H_2 mixture, $N_2:CO_2:H_2$ (8.33:1:0.314) are given in Fig. 35.

The comparison of measured values to predicted values seems to be equally good for all three H_2 concentrations. A significant error in the H_2 rate would be likely to cause one of the H_2 mixtures to have the comparison of prediction to experiment be considerably different from the



LASER OUTPUT

J_{ex}/J_p
 $E/N \ 10^{-16} \text{ V cm}^2$
 $T_e \text{ eV}$
 $n_e \ 10^{-12} \text{ cm}^3$
 $T_{g_0} \text{ }^\circ\text{K}$

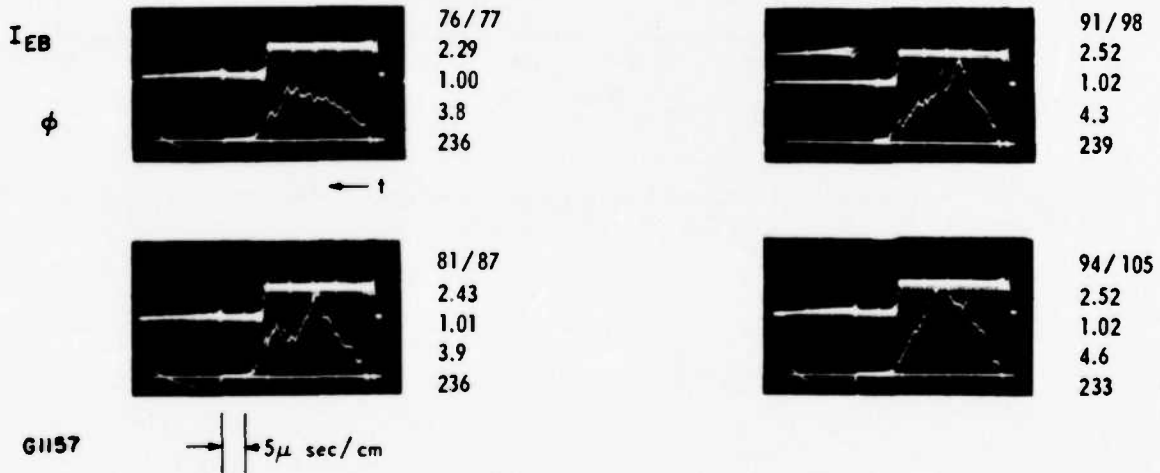


Fig. 30 Laser Output for $\text{H}_2 : \text{CO}_2 : \text{CO} : \text{H}_2$ (8.33:1:0:0.19) at Low Temperature.

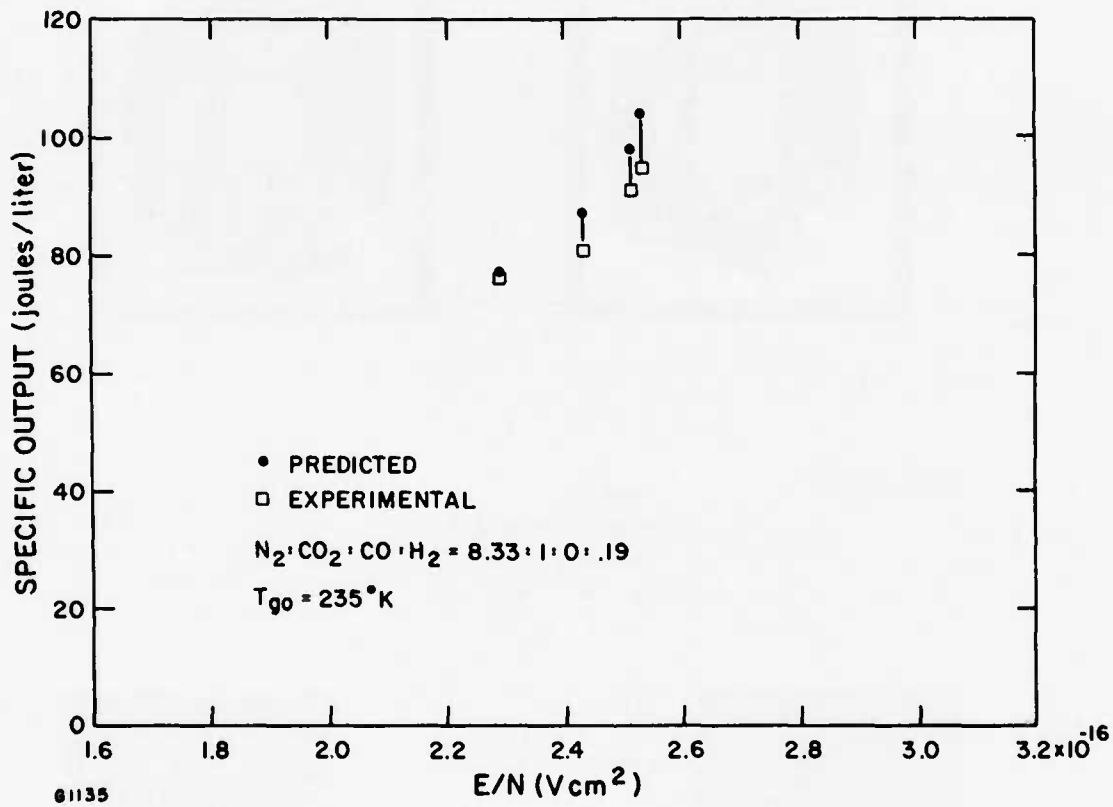
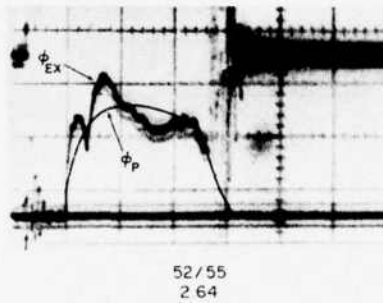
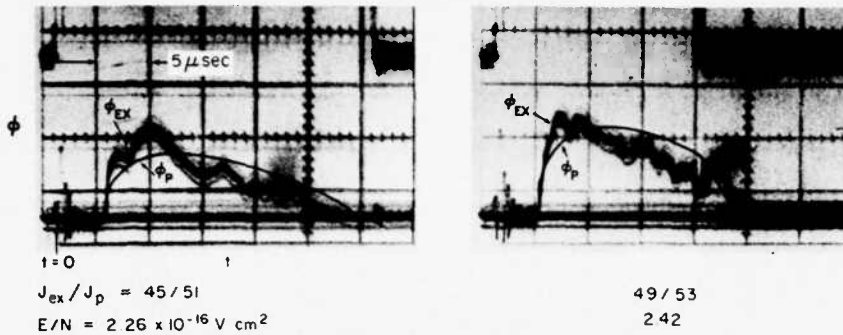
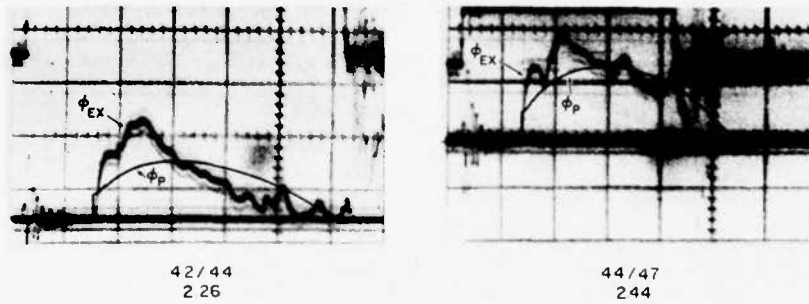


Fig. 31 Experimental and Predicted Values of Specific Output vs E/N for $N_2:CO_2:CO:H_2$ (8.33:1:0:0.19) at Room Temperature.

$N_2 : CO_2 : CO : H_2 = 8.33 : 1 : 0 : .19, T_{g0} \approx 300^\circ K$



$N_2 : CO_2 : CO : H_2 = 16.4 : 1 : 0 : .36, T_{g0} \approx 300^\circ K$



$N_2 : CO_2 : CO : H_2 = 7.19 : 1 : 1.14 : .19, T_{g0} \approx 300^\circ K$

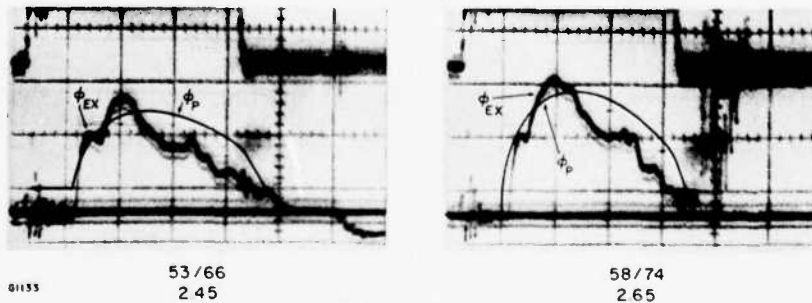


Fig. 32 Measured and Predicted Flux Onset Times and Flux Time Histories for Representative Cases of the Gas Mixtures $N_2 : CO_2 : CO : H_2$ (8.33:1:0:0.19), (16.4:1:0:0.36), and (7.19:1:1.40:0.19) at Room Temperature.

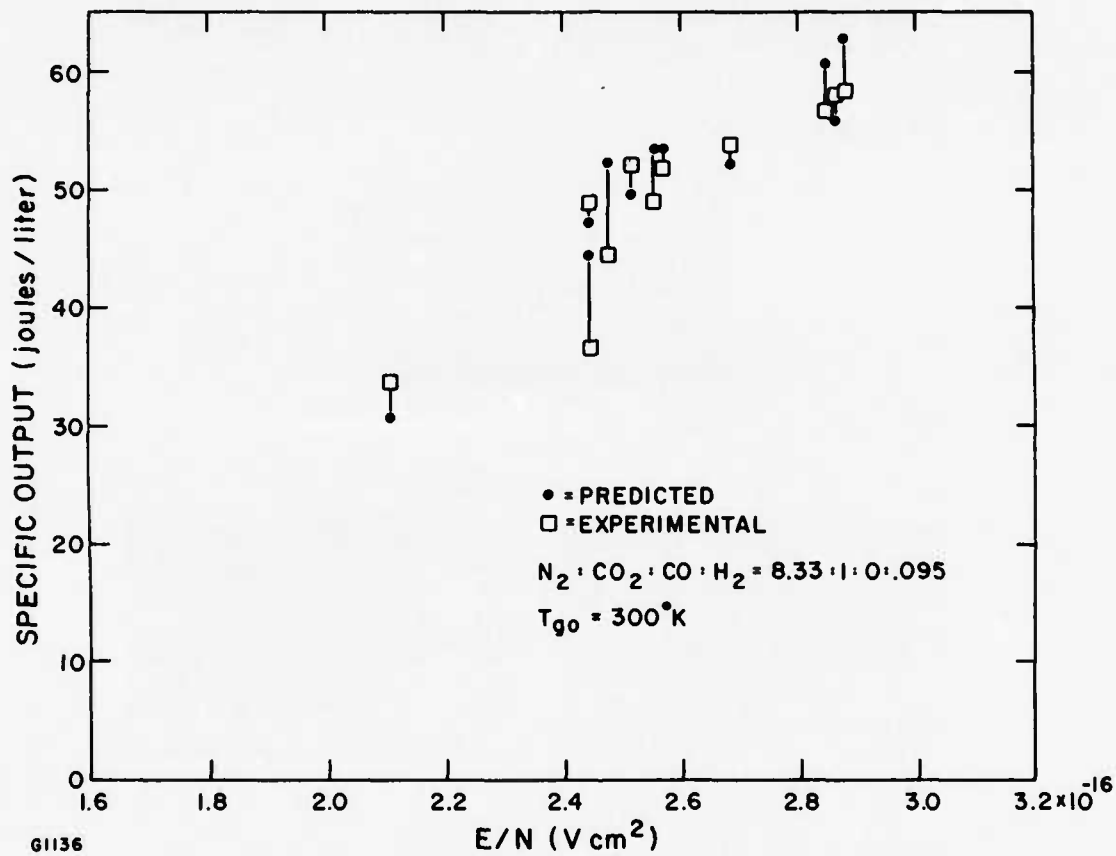


Fig. 33 Experimental and Predicted Values of Specific Output vs E/N for $N_2 : CO_2 : CO : H_2$ (8.33:1:0:0.095) at Room Temperature.

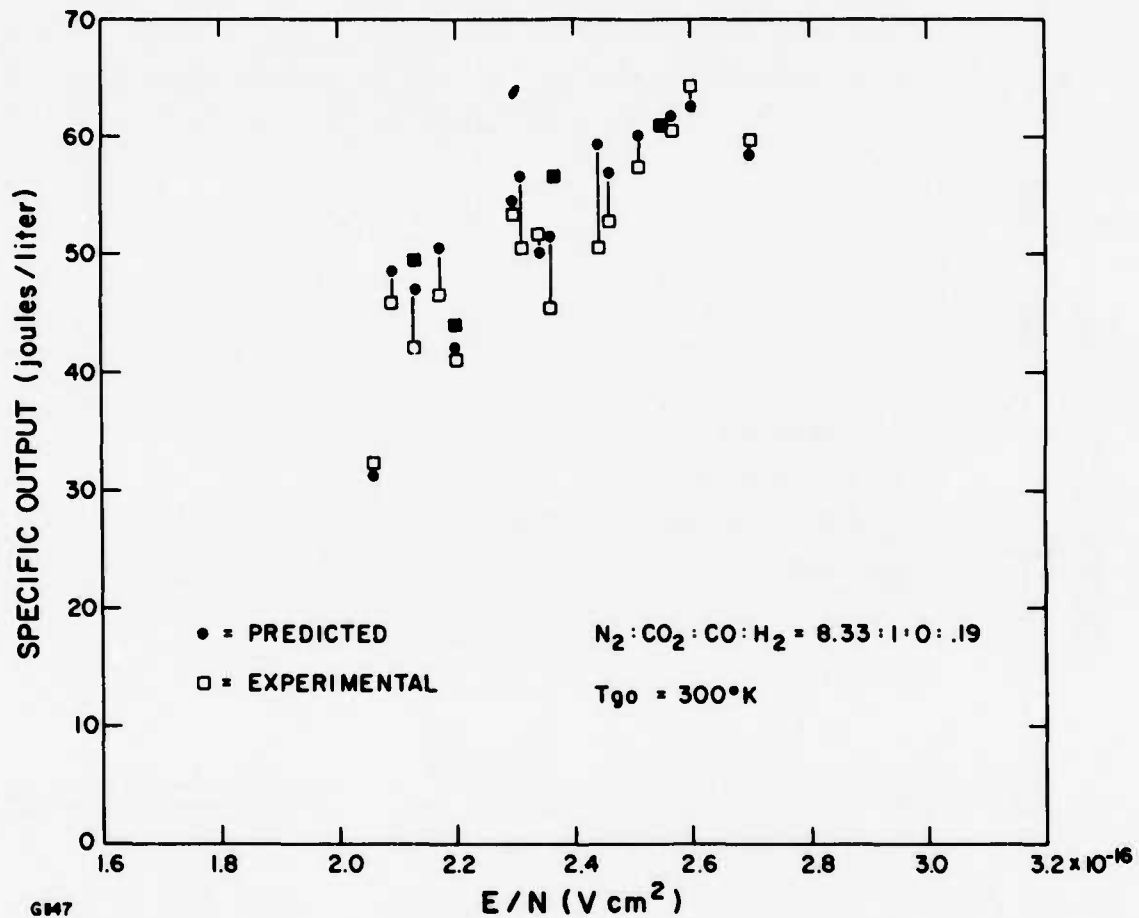


Fig. 34 Experimental and Predicted Values of Specific Output vs E/N for $N_2:CO_2:CO:H_2$ (8.33:1:0:0.19) at Room Temperature.

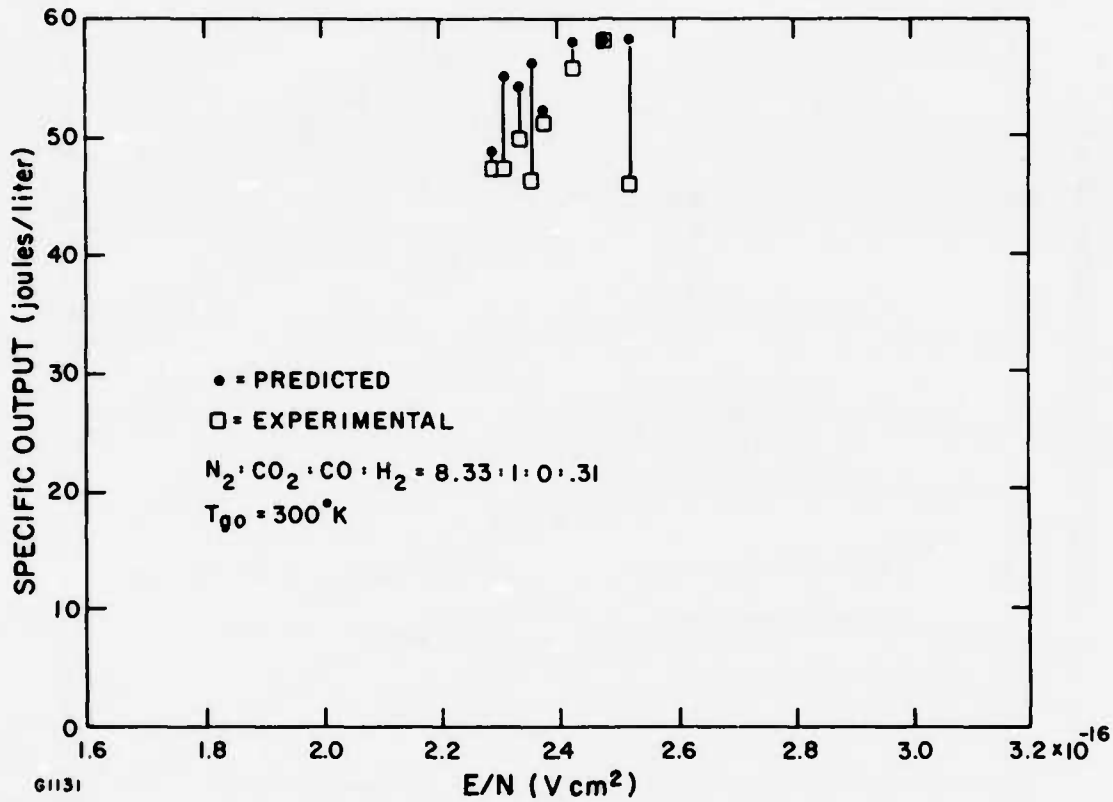


Fig. 35 Experimental and Predicted Values of Specific Output vs E/N for $N_2 : CO_2 : CO : H_2$ (8.33: 1: 0: 0.314) at Room Temperature.

comparisons found for the other two H_2 contents. No such asymmetry was seen.

The laser output measurements for the 5.5-percent CO_2 mixture $N_2:CO_2:H_2$ (16.4:1:0.36) at $300^\circ K$ is plotted with the code prediction in Fig. 36 as a function of E/N . Again, although there is some scatter, the predictions and experiment agree reasonably well and are consistent with the 5.5-percent CO_2 data of Group II (Fig. 27).

2.4 COMBUSTION PRODUCT GAS

2.4.1 Group IV

Laser output measurements were made using the combustion product gas (which contains impurities) produced at Avco-Lycoming. A simulated mixture was made up which had the same N_2 , CO_2 , CO , and H_2 composition as the actual combustion mixture, but without impurities. The actual combustion product gas mixture also contained about one percent each of argon and O_2 . The argon has little effect on the kinetics in such small quantities (argon behaves essentially like helium but slowed by the square root of the mass ratio). The O_2 affects the discharge in that the attachment coefficient for O_2 is large and that 1-percent O_2 causes a significant decrease in the electron density and, correspondingly, in the sustainer current. Indeed, the current was down by about one-third as expected in the combustion product gas from the current that was drawn in the simulated gas for the same E-beam input. This decrease in electron density does not affect the comparison between theory and experiment since in computing the predicted output the proper electron density is computed from the current measurement.

For comparison purposes, four test sequences were made:

- (1) using the actual combustion mixture at $300^\circ K$ initial temperature,
- (2) using the simulated mixture also at $300^\circ K$ followed by
- (3) the actual mixture at low temperature ($220^\circ K$) and
- (4) the simulated mixture also at low temperature ($220^\circ K$).

These sets of data were taken when 20 percent of the beam was not reaching the calorimeter. Otherwise, the data were taken with the 3- x 3-cm mask in front of the large resonator mirror, as above.

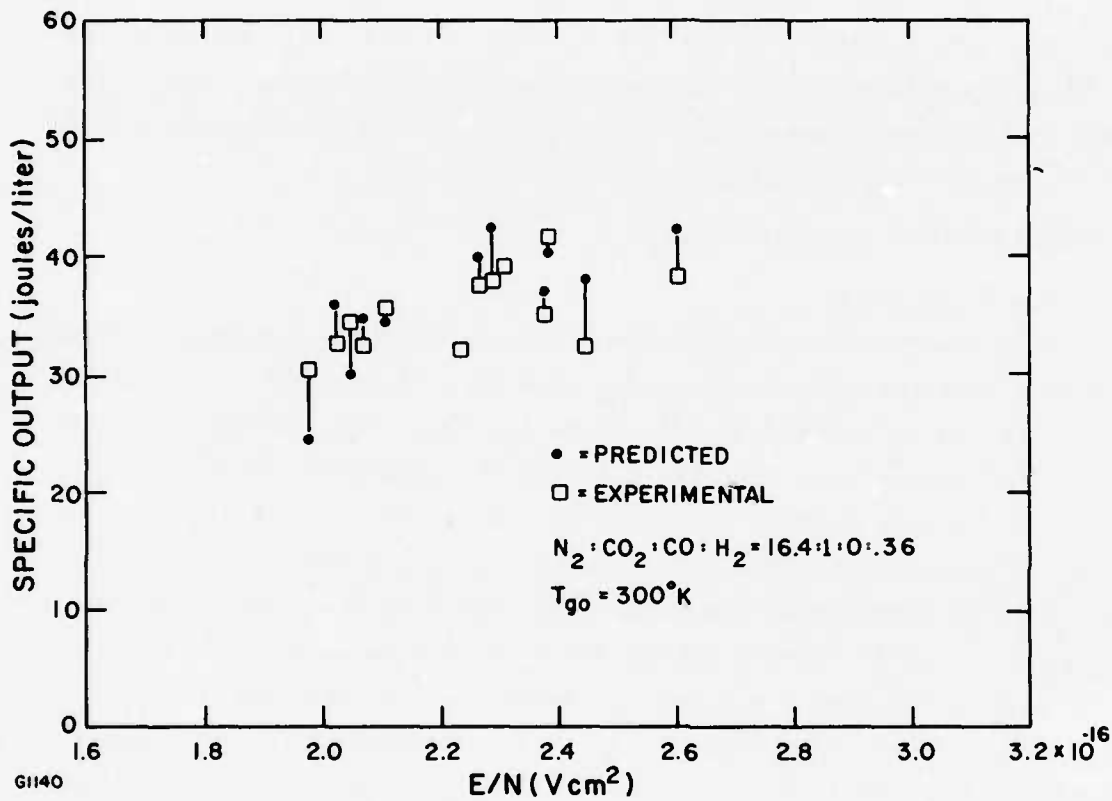


Fig. 36 Experimental and Predicted Values of Specific Output vs E/N for $N_2 : CO_2 : CO : H_2$ (16.4 : 1 : 0 : 0.36) at Room Temperature.

The laser output data (with the correction factor applied) are given in Fig. 37 for the actual combustion mixture, and the corresponding predicted and measured specific outputs are given as a function of E/N in Fig. 38. The gas composition was $N_2:CO_2:CO:H_2$ (6.3:1:0.20:0.11) plus the O_2 and argon mentioned above, with a $300^\circ K$ initial gas temperature.

Laser output data for the simulated combustion gas $N_2:CO_2:CO:H_2$ (6.3:1:0.20:0.11) with the correction factor applied are presented in Fig. 39. The corresponding predicted and measured values as a function of E/N are included in Fig. 38. The agreement between theory and experiment is rather good for both simulated and actual combustion product gases. Of particular importance is that both gases do about equally well with respect to their corresponding theoretical values, which indicates that the impurities due to the combustion process are sufficiently small and do not appear to have any deleterious effects.

A good comparison between the actual and the simulated combustion product was also obtained at low temperature. The laser output data is given in Fig. 40 for the actual combustion gas and in Fig. 41 for the simulated combustion product gas; all for initial gas temperatures of 210 to $240^\circ K$. The measured and predicted specific outputs are given vs E/N in Fig. 42. Again the actual combustion product gas performed as well with respect to predictions as did the simulated, impurity-free version.

2.4.2 Group V

Additional laser output measurements were made using a slightly different end product combustion gas mixture. The gas mixture was $N_2:CO_2:CO:H_2$ (6.2:1:0.2:0.98) and again contained about 1-percent argon and 1-percent O_2 plus combustion impurities.

The predicted and measured values as a function of E/N are given in Fig. 43 for data taken at about 215° , 250° and $300^\circ K$. The comparison with theory is again reasonably good for the $215^\circ K$ data, although there is some scatter. For the data at $300^\circ K$, the agreement with theory is fair, but the average discrepancy is over 10 percent. For the data taken at $250^\circ K$, the agreement between the measured performance and the predicted values is quite good.



$E/N = 2.78 \times 10^{-16} \text{ V cm}^2$
 $T_{g_0} = 300 \text{ }^\circ\text{K}$



2.78
 300

LASER OUTPUT

J_{ex}/J_p
 $E/N \text{ } 10^{-16} \text{ V cm}^2$
 $T_e \text{ eV}$
 $n_e \text{ } 10^{-12} \text{ cm}^3$

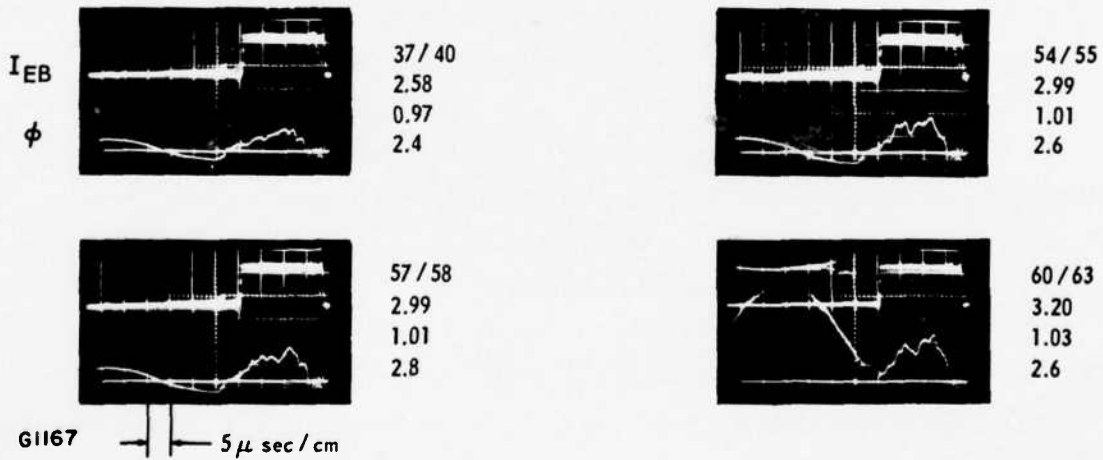


Fig. 37 Laser Output for Actual Combustion Product Gas $N_2:CO_2:CO:H_2$ (6.2:1:0.2:0.11) at Room Temperature.

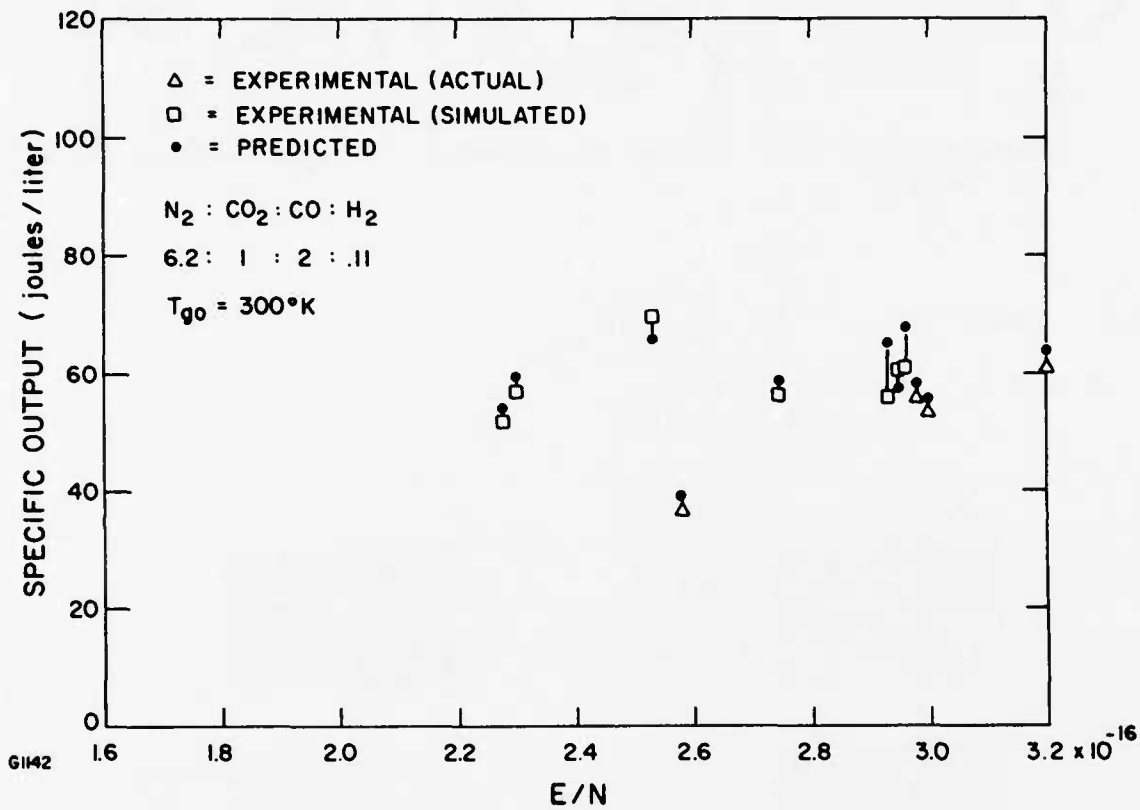


Fig. 38 Experiment and Predicted Values of Specific Output vs E/N for Actual and Simulated Combustion Product Gas $N_2 : CO_2 : CO : H_2$ (6.2 : 1 : 0.2 : 0.11) at Room Temperature.



$E/N = 2.23 \times 10^{-16} \text{ cm}^{-3}$
 $T_{g_0} = 300 \text{ }^\circ\text{K}$



2.45
300

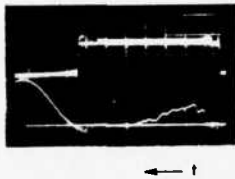


2.96
300

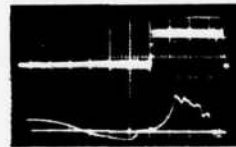
LASER OUTPUT

$J/l \text{ EX } J/l \text{ P}$
 $E/N \text{ } 10^{-16} \text{ V cm}^2$
 $T_e \text{ eV}$
 $n_e \text{ } 10^{-12} \text{ cm}^3$

I_{EB}
 V_s



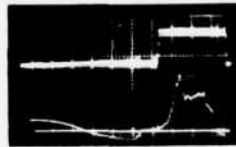
57/59
2.23
0.93
4.4



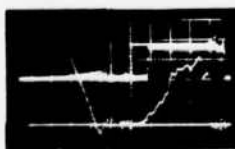
60/57
2.96
1.01
3.8



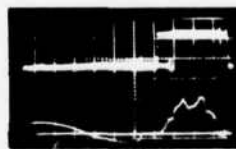
52/53
2.21
0.93
4.1



57/65
2.94
1.01
3.8



66/64
2.45
0.95
4.3



61/68
2.95
1.01
3.6

G1166

$5 \mu \text{ sec/cm}$

Fig. 39 Laser Output for Simulated Combustion Product Gas $\text{N}_2 : \text{CO}_2 : \text{CO} : \text{H}_2$ (6. 2: 1: 0. 2: 0. 11) at Room Temperature.



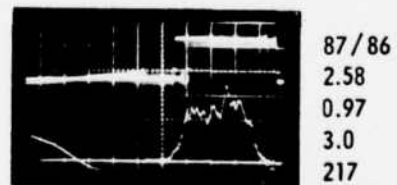
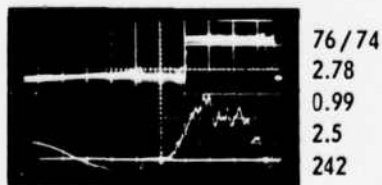
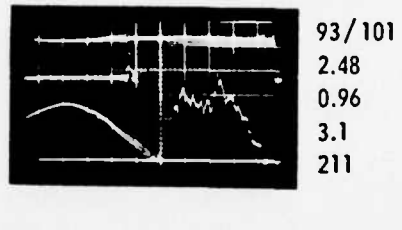
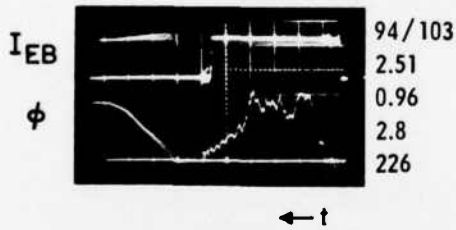
E/N 2.73×10^{-16} V cm²



2.47

LASER OUTPUT

J_{ex}/J_p
 E/N 10^{-16} V cm²
 T_e eV
 n_e 10^{-12} cm³
 T_{g0} °K



G1156 → ← 5 sec/cm

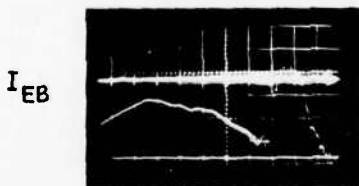
Fig. 40 Laser Output for Actual Combustion Product Gas N₂:CO₂:CO:H₂ (6. 2: 1: 0. 2: 0. 11) at Low Temperature.



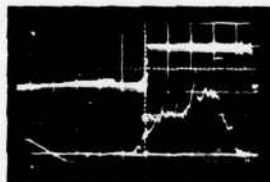
$E/N = 2.40 \times 10^{-16} \text{ V cm}^2$

LASER OUTPUT

J_{ex}/J_p
 $E/N \ 10^{-16} \text{ V cm}^2$
 $T_e \ \text{eV}$
 $n_e \ 10^{-12} \text{ cm}^3$
 $T_{g_0} \ ^\circ\text{K}$

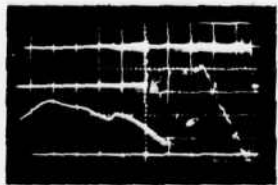


70/86
 2.46
 0.96
 4.0
 210



100/105
 2.4
 0.95
 3.6
 222

← t



88/92
 2.50
 0.96
 3.8
 218

G1162

$5 \mu\text{sec/cm}$

Fig. 41 Laser Output for Simulated Combustion Product Gas $\text{N}_2:\text{CO}_2:\text{CO}:\text{H}_2$ (6.2:1:0.2:0.11) at Low Temperature.

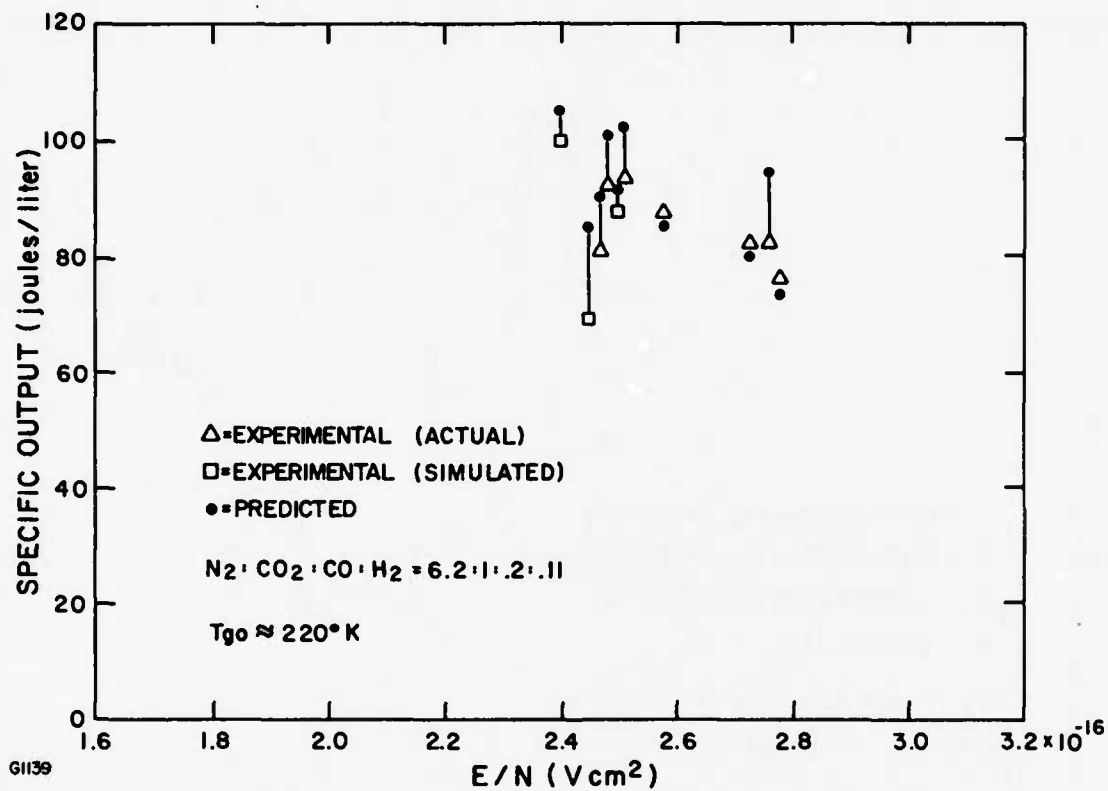


Fig. 42 Experimental and Predicted Values of Specific Output vs E/N for Actual and Simulated Combustion Product Gas $N_2 : CO_2 : CO : H_2$ (6.2 : 1 : 0.2 : 0.11) at Low Temperature.

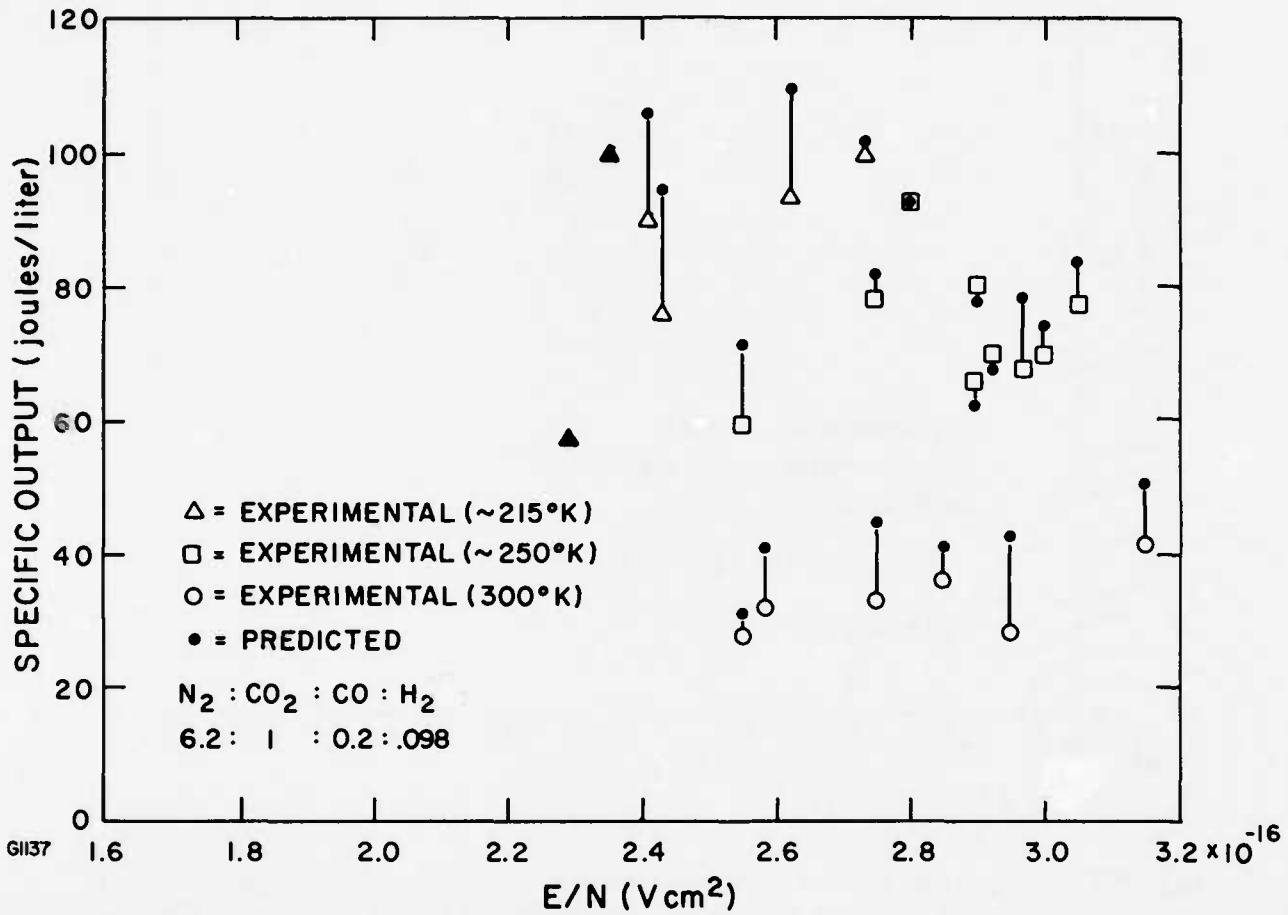


Fig. 43 Experimental and Predicted Values of Specific Output vs E/N for Combustion Product Gas $\text{N}_2 : \text{CO}_2 : \text{CO} : \text{H}_2$ (6.2 : 1 : 0.2 : 0.098) at $T_{g0} = 215^\circ\text{K}$, 250°K and 300°K .

The predicted flux histories for some representative cases from Groups IV and V are given with the measured flux signal in Fig. 44. Again there is reasonable agreement between measured and predicted onset times.

2.5 SUMMARY AND CONCLUSIONS

These experiments, for gases related to possible combustion product gas mixtures, gave results that generally agreed well with predictions and tended to verify the applicability of the kinetics code. Only CO-containing gases showed any significant discrepancy in the comparison of measured performance with predicted performance.

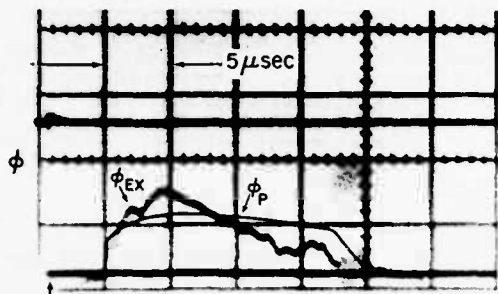
Tests at temperatures down to 210°K were made with actual combustion product gases prepared by Avco-Lycoming. No unexpected problems due to background impurities were observed. The particular gas tested did have a 1-percent O₂ content (which can be avoided in combustion product gases) and a corresponding expected decrease in sustainer current was observed. The measured laser output performance for this combustion product gas was as expected, both with respect to the kinetic code predictions and relative to the performance of a simulated gas mixture of the same N₂, CO₂, CO and H₂ composition, but free of impurities.

The measurements made for the gas mixtures without CO were all consistent with respect to the corresponding predictions, both for variations in the CO₂ content and for variations in the H₂ content. Measurements of small signal gain and of the spectral time history indicated proper performance with respect to the kinetics code. These measurements showed that at low temperature the lasing action began on the P(14) transition, going to higher P-lines as the gas heated, and that the small signal gain increased at a rate corresponding to the pumping rate assumed in the kinetics code 2. Both for room temperature and for low initial gas temperatures, the measured laser output was within 10-percent of predictions, and the observed laser output onset times agreed quite well with the predicted onset times.

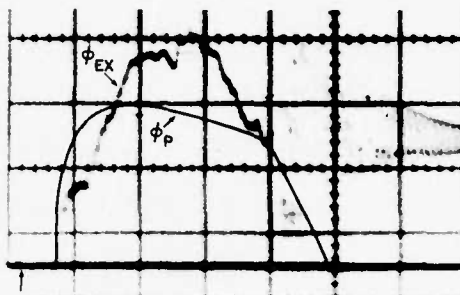
The predicted laser outputs for CO-containing gases were higher than the measured values. Despite this discrepancy, small CO contents may not be particularly harmful in combustion product gases. The CO content did allow operation without arcing at electric field (E/N) values

COMBUSTION PRODUCT GAS (ACTUAL)

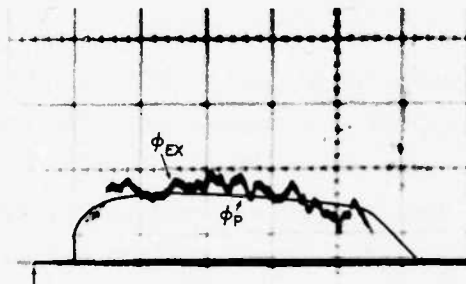
$N_2 : CO_2 : CO : N_2 = 6.2 : 1 : .2 : .098$



$t = 0$
 $J_{ex} / J_p = 36 / 41$
 $EN = 2.83 \times 10 \text{ V cm}$
 $T_{go} = 300^\circ K$



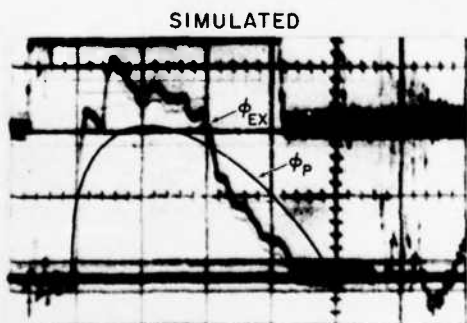
78/72
 2.71
 253



99/101
 2.73
 219

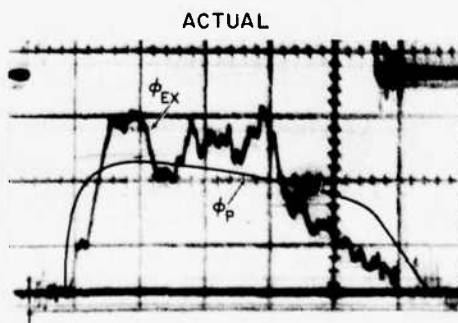
COMBUSTION PRODUCT GAS

$N_2 : CO_2 : CO : N_2 = 6.2 : 1 : .2 : .11$



66/64
 2.45
 300°K

G1134



94/103
 2.51
 226°K

Fig. 44 Measured and Predicted Onset Times and Flux Time Histories for Representative Cases of Combustion Product Gas.

somewhat higher than for comparable mixtures without CO, and the measured laser outputs were still as large (in fact, slightly larger due to the higher possible E/N and power input) as those for comparable non-CO gas mixtures. The reason for the lower than predicted output is not clear. The small signal gain measurements for the 6-percent CO mixture gave good agreement with predictions suggesting proper CO excitation rates and proper transfer to the CO_2 . However, somewhat in keeping with the discrepancy in laser output, the observed lasing onset time is somewhat later than predicted (as shown in Figs. 23 and 32), the discrepancy being larger for the CO mixes than for the non-CO mixes.

The variation in performance with respect to CO_2 and CO content is illustrated in Fig. 45, where the average ratio of experimental-to-predicted specific outputs ($J/\ell_{\text{ex}}/J/\ell_{\text{p}}$) for each gas is plotted as a function of CO_2 and CO content. The variation with CO_2 content is rather flat (as is the variation with H_2 content as shown by the data of Figs. 33, 34, and 35), while a more significant departure from theory exists with respect to CO content. This discrepancy for CO-containing gases does not necessarily imply that the specific output is decreased if some CO is substituted for N_2 , it is more a non-manifestation of the predicted increase with CO addition, as illustrated in Fig. 45(b). The plot of Fig. 45(b) shows the predicted variation in specific output vs CO_2 and CO variation, with each gas mixture run for the same values of E/N , n_e and T_{g0} . The gas composition for the CO_2 variation has 2% H_2 and the balance N_2 , and for the CO variation the gas has a constant 10.5% CO_2 with 2% H_2 and the balance N_2 , as in Fig. 45(a). The values of E/N , n_e and T_{g0} used for generating Fig. 45(b) correspond to one of the runs of the reference gas mixture 10.5% CO, 2% H_2 , no CO and 87.5% N_2). The corresponding experimental curve also shown in the figure was obtained by multiplying the predicted curve by the experiment-to-theory discrepancy factors shown in Fig. 45(a) for these gas mixtures. The resultant curve shows little change in specific output with CO addition, rather than the predicted increase.

The cause of this discrepancy has not been identified. The problem could be due either to the kinetic code itself or to an experimental error. If the problem is thought to be experimental and to be either in the inputs

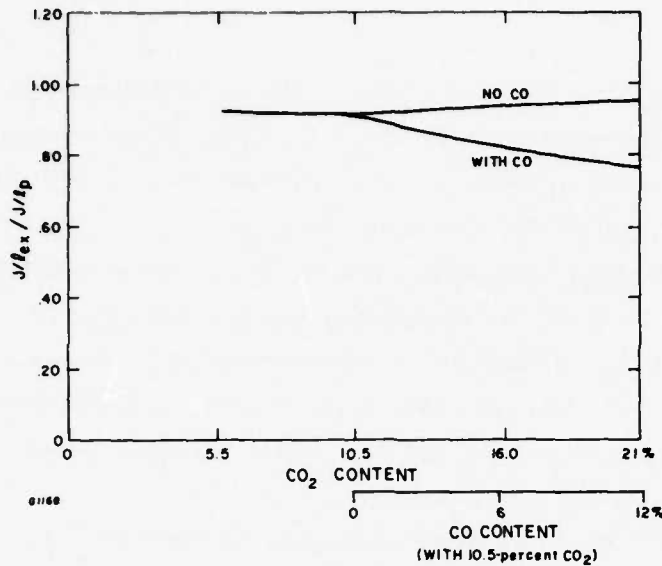


Fig. 45(a) Variation in Output Relative to Prediction as a Function of CO_2 and CO content is the ratio of measured to predicted specific outputs

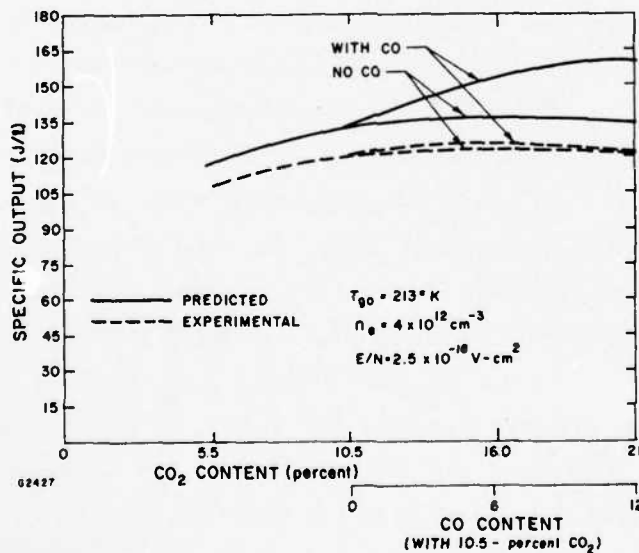


Fig. 45(b) Plot of Specific Output vs Gas Composition for Constant E/N , T_{g0} and n_e values. The H_2 content is 2% and the balance of the gas is N_2 . For the CO content variation, the CO_2 content is 10.5% with 2% H_2 and the balance is N_2 . The curve labeled experimental is obtained from the predicted curve by multiplying by the corresponding experiment-to-theory discrepancy factors shown in Fig. 45(a).

to the code (namely, the voltage and current measurements) or in the measurements of the laser output, then a reason would be needed as to why the problem was only of significance to the CO data. The possible errors in the code itself would likely be related to the kinetic process and rates for CO. It is possible that the problem could be related to another gas, but if so, then any correction for that gas should not be inconsistent with the results for other gas mixtures. For example, the 12-percent CO data are somewhat sensitive to the accuracy of the H₂ rate for deactivating the CO₂ bending mode; however, not sufficiently more sensitive than the data for the other gases (where good agreement was obtained) to warrant the consideration of a change in the H₂ rate. Possible problems in the CO kinetics would include unexpectedly high values of H₂ deactivation of CO, V-V transfer to a mode of CO₂ other than the upper laser level, or superelastic electron-CO collisions (i. e., electron deexcitation of CO). Also, there is the possibility that poor V-V transfer out of the CO to the CO₂ or N₂ or an error in the computation of the electron distribution for a given E/N value would affect both the CO electron excitation rate and the CO₂ and N₂ rate. Some of these possible corrections have been examined, but only very slight changes in the predicted outputs have been found at this time.

3.0 GAS SYSTEM

3.1 GAS PRODUCTION

3.1.1 Introduction

Laser gas which had actually been produced by combustion of a hydrocarbon fuel with air in a burner needed for experiments on Humdinger Junior. An actual combustion product gas was required rather than a synthesized gas in order to determine the influence of gas components associated with combustion products which could not be replicated with synthesized gases. These components are particulates and/or hydrocarbons and other trace species, whose concentration in the combustion products is intimately related to the burner concept and characteristics. The laser gas to be produced was desired at fuel/air ratios consistent with the results for optimal gas composition as determined in the laser experiments. These gases were also desired early in the program, and in sufficient quantity to conduct an experimental investigation of the gas products composition and verification of the synthesized gas laser performance and practicability of utilizing combustion products as a laser gas.

The products of combustion that are the result of burning a hydrocarbon fuel in air are critically dependent upon the burner design and fuel/air ratio. Current gas turbine burners rely upon excess air to provide burner cooling as well as burner exit temperatures consistent with turbine blade material limitations. The excess air insures complete combustion. The mixing process and subsequent cooling with excess air determines what gas species result in the exhaust product. The O_2 content of typical gas turbine exhaust is over 10%. This O_2 concentration in the exhaust product is unacceptable if the gas products are to be used as a laser gas (due to the high electron attachment cross section of O_2 , only a few tenths of a percent O_2 are allowable). Utilizing cooled combustion gas products (without O_2) to cool the burner and the gas products in a recirculation concept is attractive, but would require development of the burner.

An alternative approach, which was used to generate the gases, was to utilize a research burner (developed for low pollution emission). Although excess air is required, the appropriate gas can be obtained by extracting only gases from the combustion zone of the burner.

3. 1. 2 Gas Generation and Processing

The gas composition requirements were established on the basis of preliminary analyses. The requirements comprised a specification of desired species and concentrations, as well as the limiting concentrations of "pollutants". Table 2 below summarizes the initial desired composition of the combustion gases. (See Section 1.0 of this report.) The particulates were further restricted both in terms of size and mass fraction a radius less than 0.5 μm and a mass concentration less than 0.2 percent compared to the original requirement of 10- μm diameter.) The initial CO_2 concentration requirement was based on the knowledge of combustion products and not necessarily that of the optimum laser gas mixture. The optimum would be the result of a complex tradeoff between gas generation system and laser device, including the electrical power system, laser gas feed system, and cavity design; since the laser gas composition and its performance (e. g., specific output, electro-optical efficiency, etc.) influence these system characteristics. The CO_2 concentration anticipated was approximately 12 percent by volume. Nitrogen gas formed the bulk of the residual gases.

TABLE 2
COMBUSTION GAS COMPOSITION REQUIREMENTS

Oxygen (O_2)	< 300 ppm
Carbon Monoxide (CO)	< 2 percent
Hydrogen (H_2)	\leq 2 percent
Water Vapor	< 150 ppm
Particulates	< 10- μm diameter and 0.02% by mass
Nitrogen Oxides	< 1000 ppm
Sulphur Dioxide (SO_2)	< 500 ppm

AD-A039 812

AVCO EVERETT RESEARCH LAB INC EVERETT MASS
HIGH SPECIFIC ENERGY PULSED ELECTRIC DISCHARGE LASER RESEARCH. (U)
DEC 75 D H DOUGLAS-HAMILTON, R M FEINBERG

F/G 20/5

DAAH01-75-C-0503

NL

UNCLASSIFIED

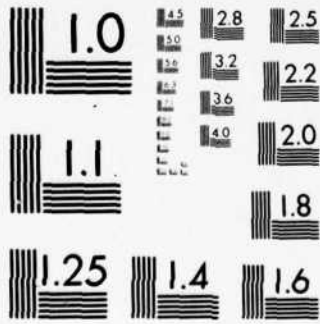
2 of 2
ADA039812



END

DATE
FILMED
6-77

039 8

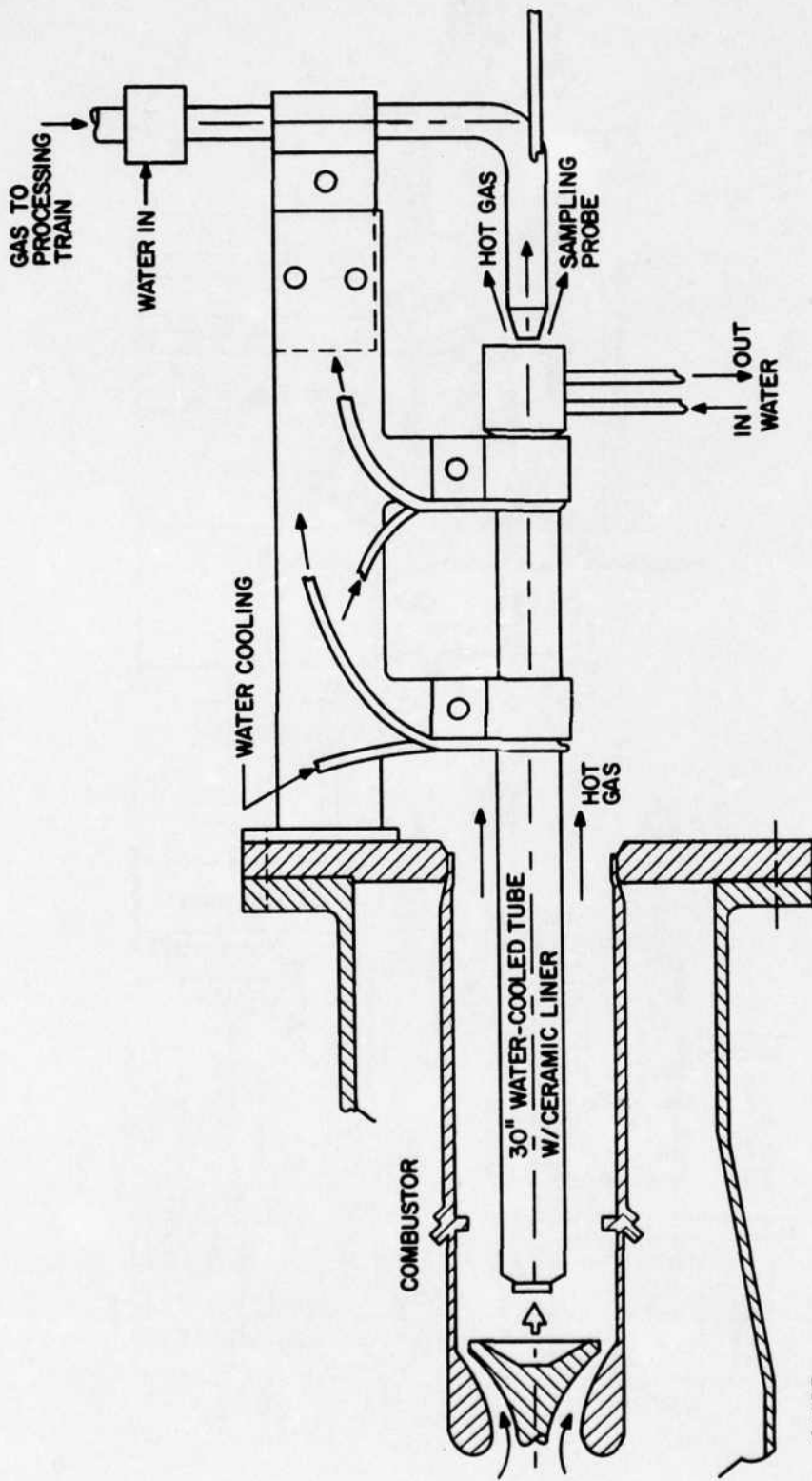


MICROCOPY RESOLUTION TEST CHART
NATIONAL BUREAU OF STANDARDS-1963-A

The Avco-Lycoming turbine combustor development facility was used with a low pollutant emission burner providing the combustion gases. The burner system operates with excess air (supplied to the burner at approximately 50 psia and 400°F. However, there are regions where the burner conditions are either stoichiometric or fuel rich, thereby providing the necessary conditions for O₂-free gas products. A water-cooled tube was inserted into the combustor primary zone to ingest the relatively rich primary zone gas. Details of the probe and tube are shown in Fig. 46. The tube length (30 inches) was selected to permit sufficient time for the gas to reach equilibrium. A ceramic tube was inserted into the water-cooled tube to keep the gases hot and reduce boundary layer quenching. A water-cooled probe collected the hot gas at the end of the ceramic tube and provided initial cooling of the hot gas.

The gas discharge entering the large sampling probe was further cooled, sub-cooled to drop out excess water, filtered, dried, filtered again, and then pumped up to the storage bottle pressure (Fig. 47). At the exit of the high pressure pump, an oil filter was used to remove any oil that may have been introduced by the compressor. Bottles were pumped up to 2000 psig, while maintaining combustor fuel and air flow as steady as possible; the bottles were evacuated by means of a vacuum pump prior to filling with gas. No measurable variations were noted in combustor air flow. Fuel flow indicated fluctuations were ± 0.1 to 0.2 lb/hr at flows approximately 50 lb/hr. Air inlet temperature was held at approximately 400°F, and did not change over 10°F during any one test.

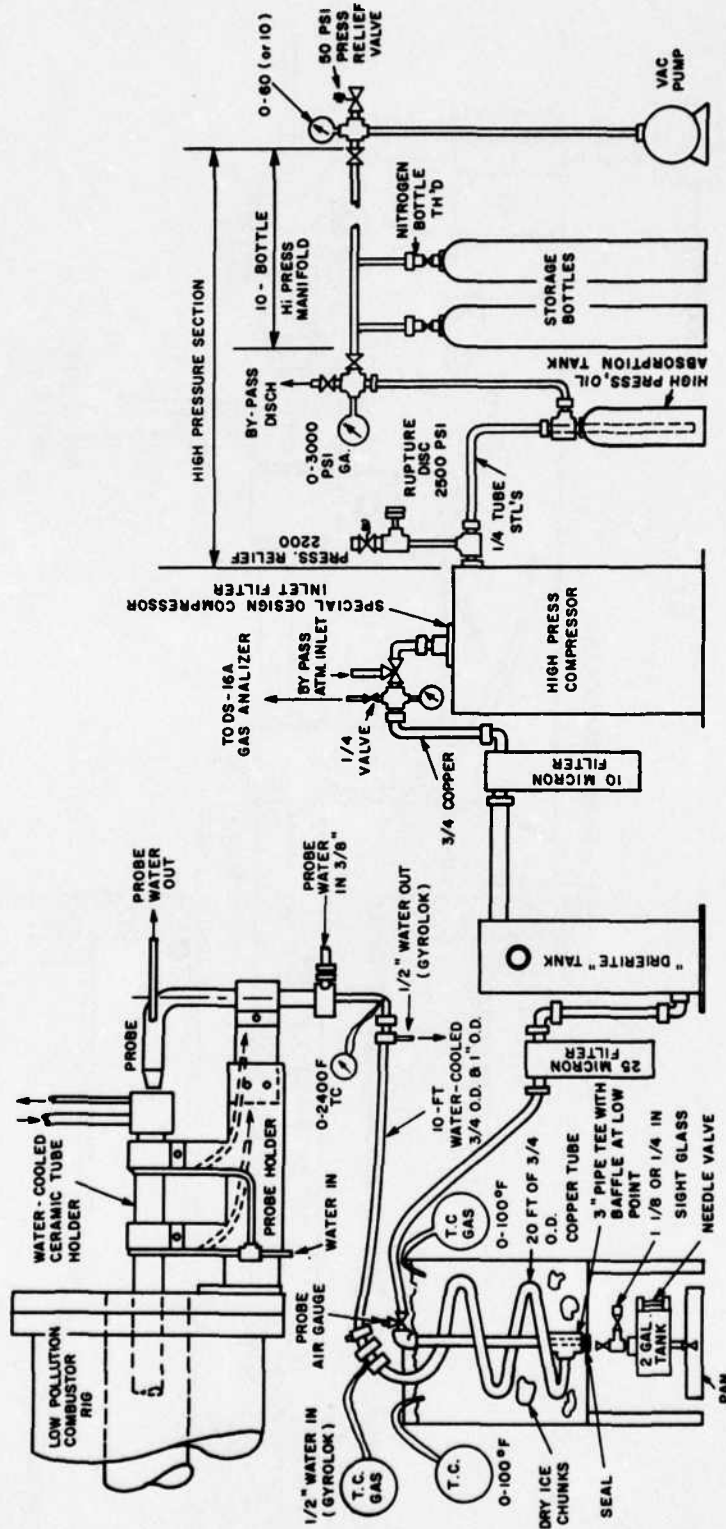
Gas composition was monitored on the Avco-Lycoming DS-16A gas analyzer (See Table 3) during the full length of the tests and recorded two to three times for each bottle filled. In addition, samples were analyzed from each bottle approximately three days after filling. Small sample bottles were filled from each storage bottle in order to have the gases analyzed by an independent laboratory (Gollob) which were analyzed by both mass spectroscopy and chromatography:



G1405

Fig. 46 Lycoming Gas Generator Schematic of Combustor, Water-Cooled Tube and Sampling Probe

1. ALL FITTINGS IN GAS SAMPLE LINE ARE 3/4" TUBE SIZE OR LARGER, MINIMUM I.D. IS 5/8" UP TO H.P. PUMP; 1/4 TUBE DOWNSTREAM.
2. ALL VALVES IN GAS SAMPLE LINE ARE 3/4" BALL OR PLUG, OR LARGER.
3. ALL FITTINGS & TUBING FOR HIGH PRESSURE SECTION ARE RATED FOR 2000 PSI PLUS SAFETY FACTOR.



61406

Fig. 47 Gas Generator

TABLE 3
AVCO-LYCOMING GAS ANALYSIS MEASUREMENT ACCURACIES

A. INSTRUMENT ACCURACIES

Specie	Instrument	Range	Accuracy
O ₂	Beckman	0 to 5	± 500 ppm
CO	Mine Safety 200 (Non-Dispersive Infrared)	0 to 800 ppm	± 8 ppm
HC	Varian 1400 (Flame Ionization Detector)	0 to 300 ppm (Carbon) 0 to 10000 ppm C	± 3 ppm C ± 100 ppm C
CO ₂	Mine Safety 300 (Non-Dispersive Infrared)	0 to 8% 0 to 40 %	$\pm 0.08\%$ $\pm 0.4\%$
NO _x	Scott Model 225 (Chemical Luminescence)	0 to 10000 ppm	$\pm 1\%$

B. ACCURACY OF MEASUREMENT

1. Instrument Repeatability $\pm 1\%$ of full scale
2. Zero Drift $\pm 1\%$ of full scale
3. Calibration Gas Accuracy $\pm 2\%$ ($\pm 3\%$ of full scale)
4. Span Drift $\pm 1\%$

Estimated Measurement Error $\pm 3.5\%$

Mass Spectroscopy Analysis: CO₂, O₂, N₂, NO, H₂, SO₂
Chromatography: CO

The water content was determined from samples collected in a special bottle at the end of each test (when the performance of the drying system would be poorest).

3. 1. 3 Combustion Laser Gas Composition

Initial burner installation operation was used to determine the gas composition and its variation with fuel flow. The Avco-Lycoming on-line DS-16A gas analyzer, as well as the Gollob measurements were used to establish the dependence of specie concentrations on burner operating conditions. The results of the initial measurements are presented in Fig. 48. Increasing the fuel flow while increasing the H₂ content also increases the hydrocarbon and CO. The O₂ concentration conversely decreases with increased fuel flow. Both the Avco-Lycoming and Gollob measurements illustrate these trends. The CO₂ content remains nearly constant; the increase in fuel flow resulting in production of CO, hydrocarbons and water vapor. The NO concentration remained nearly constant. The acceptable O₂ concentrations were established at fuel flows greater than 45 lb/hr. The CO concentration, however, was greater than the initial target requirement of less than two percent, but still acceptable at three percent. The most attractive gas composition is realized at a fuel flow of 48.5 lb/hr. Most of the gas was generated at this fuel flow with additional gas generated at 45 and 52.5 lb/hr.

The gases generated were analyzed for composition with the results summarized in Table 4. The compositions presented are the result of three measurements; i. e. ,

- (a) Average of 2 or 3 on-line gas analysis data points, recorded during the test, with 2 or more recordings per data point, and recorded on the Avco-Lycoming DS-16A gas analyzer.
- (b) "Average" sample from each 1A bottle, analyzed on the Avco-Lycoming DS-16A three days after the test had been completed.

TABLE 4
AVCO LYCOMING GAS GENERATOR

AVCO LYCOMING TEST AVERAGE
INCLUDES 3 DATA POINTS WITH 2
RECORDINGS AT EACH POINT

TEST RESULTS

Bottle No.	CO ₂		O ₂		HC		CO	NO	N ₂	H ₂	H ₂ O	A	SO ₂
	Avco Test Average	Collob from Bottle	Avco Test Average	Collob from Bottle	Avco Test Average	Collob from Bottle							
2	12.53%	12.43	.324	.114	108 ppm		3.5%	124 ppm	Bal.	1.66%		.94%	<.001%
3	12.31%	12.48	.364	.114	112 ppm		3.5%	126 ppm		1.90%		.94%	
4	12.56%	12.83	.442	.139	80 ppm		2.7%	126 ppm		1.41%	<5 ppm	.93%	
5	12.93%	12.65	.654	.273	80 ppm		3.1%	125 ppm		1.48%		.94%	
6	12.55%	13.28	.500	.148	94 ppm	Not Recorded	3.2%	122 ppm		1.12%	<5 ppm	.89%	
7	13.79%	12.8	1.004	.848	90 ppm	59	1.5%	114 ppm	22 ppm	.84%		.94%	<.001%
8	12.99%	12.77	1.262	1.180	160 ppm	93	1.7%	106 ppm	2 ppm	.95%		.94%	
9	13.44%	12.99	1.434	1.310	51 ppm	74	1.6%	110 ppm	1 ppm	.94%	<5 ppm	.94%	
10	11.46%	11.50	.193	.091	940 ppm	840	3.4%	103 ppm	8 ppm	2.9%		.94%	
11	12.81%	12.50	.455	.330	135 ppm	139	2.6%	117 ppm	5 ppm	1.12%		.94%	
12	12.77%	12.83	.392	.336	112 ppm	112	2.5%	118 ppm	5 ppm	1.25%		.94%	
13	12.83%	12.73	.361	.358	95 ppm	128	2.5%	118 ppm	4 ppm	1.35%		.94%	
14	12.77%	12.77	.336	.330	127 ppm	100	2.6%	118 ppm	7 ppm	1.45%		.94%	
15	13.04%	12.73	.362	.358	100 ppm	111	2.5%	118 ppm	5 ppm	1.56%		.95%	
16	12.92%	12.70	.337	.348	130 ppm	82	2.6%	118 ppm	7 ppm	1.40%	<5 ppm	.94%	
17	10.88%	11.33	.080	.033	779 ppm	640	4.5%	106 ppm	17 ppm	2.5%		.94%	
18	10.66%	11.40	.059	.033	685 ppm	733	4.6%	103 ppm	18 ppm	2.6%		.94%	

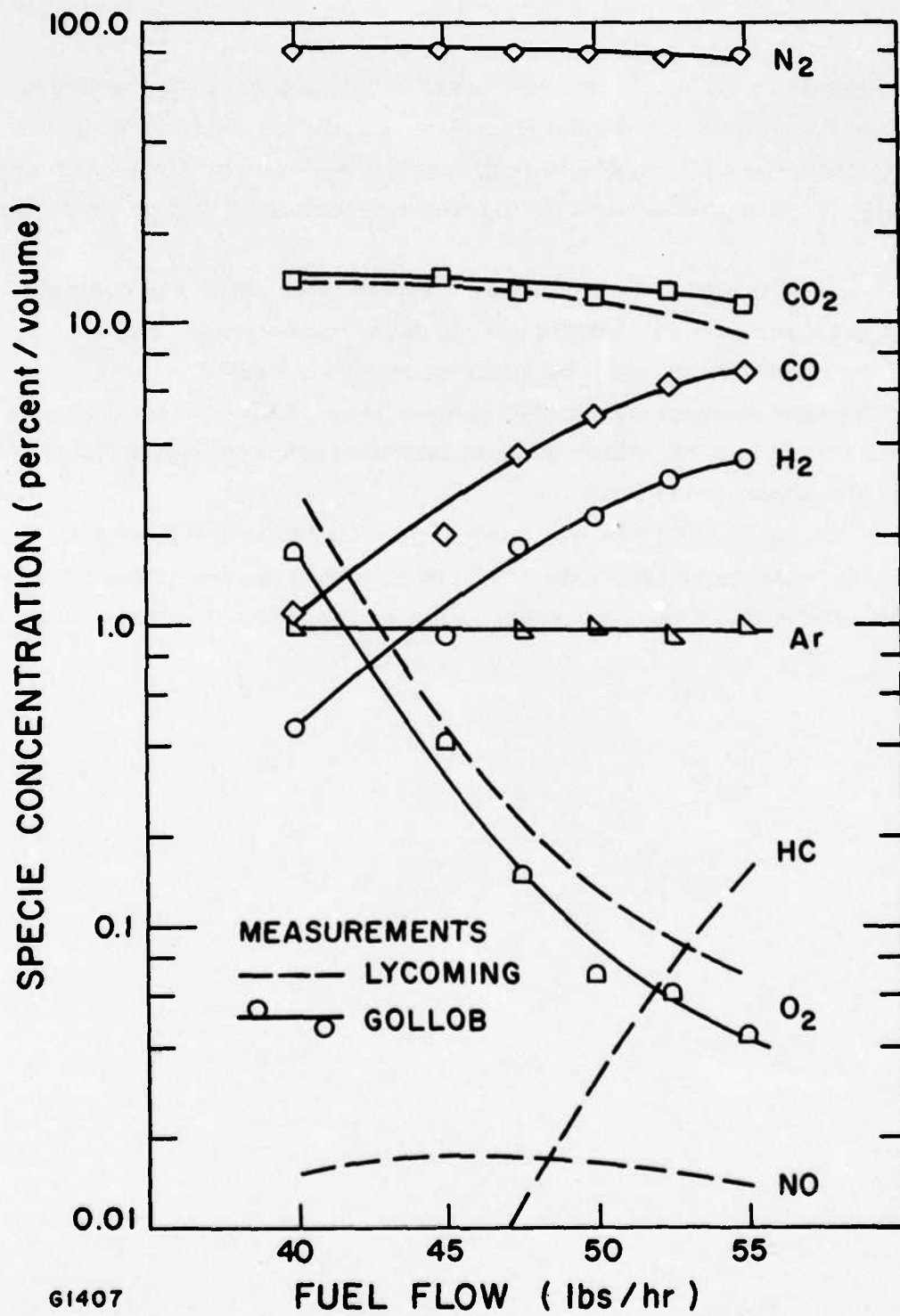
e Fuel flow increased slightly from 5 to obtain comparison
see No. has nearly "Disappeared" in the bottle

- (c) "Average" sample from each 1A bottle, analyzed by Gollob Analytical Services.

Differences exist between the three measurements, and may be caused by:

- (a) Real-time fluctuations in the gas composition, as measured on the Avco-Lycoming gas analyzer, and when compared to the bottle average.
- (b) Possible absorption of some components into the metal walls of the bottle. This is shown in particular for NO, where over 100 ppm are indicated in the sample line during the sampling operation, and only 1 to 10 ppm for the sample from the bottle after 3 days storage. Part of the variation is that of NO absorption into the steel walls of a bottle.
- (c) Differences in sensitivity and interference level in the measure of gaseous components by different detection methods. For example, the NDIR CO detector may suffer from interference from propane, diazomethane and a few other compounds, if present. Mass spectroscopy of CO is very difficult because the mass number of CO is the same as for N₂. Carbon monoxide interferences in chromatography for these gases are relatively small. Therefore, an extra chromatograph was required to detect CO.
- (d) Calibration and operational errors or malfunctions. (A recheck of data reveals no large errors of this type).

The compositions of the gases generally agreed with those selected from Fig. 48, with some variations. Fuel flow, air flow and air temperature were repeated very closely, but compositions did not repeat as well. The most probable reason is that the water-cooled tube and ceramic liner may possibly have been displaced by a small distance (1/8 to 3/16 inch) between tests. The displacement would ingest gas from a slightly different position in the primary zone of the combustor, with probable variations in composition.



61407

Fig. 48 Combustion Gas Composition Variation with Fuel Flow

Combustor flame fluctuations were most noticeable in the hydrocarbon measurements. Reduced fluctuations could be obtained by better fuel distribution and increases in both fuel and air temperature. However, the luxury of experimental optimizing was not permitted within the budget allowed.

It was noted that when fuel flow was set to produce a previously selected gas composition, but did not produce this composition exactly, the desired composition could be more precisely obtained by adjusting the fuel flow and monitoring the gas composition. This was attempted in bottles 10, 17 and 18, which were obtained on two separate days, but required the same composition.

Nitric oxide (NO) gas was analyzed by Gollob in the first six bottles, but found to be less than 150 ppm in all cases, the lower detectable limit of the mass spectrograph. This result was not listed in Table 2.

4.0 GAS PRODUCTION SYSTEMS

4.1 INTRODUCTION

The generation of laser gas through a combustion process provides an attractive concept, especially if the fuel considered is one that is readily available in the field. The concept (among several) which has received particular attention is that which burns fuel at above stoichiometric conditions resulting in an acceptable laser gas containing H_2 , CO_2 and N_2 in appropriate concentrations. In addition, CO is present. Water vapor, one of the resulting species in the combustion process, can be removed by cooling the gas combustion products to a condition consistent with the desired or acceptable dew point.

The gas temperatures which result from stoichiometric burning are excessively high for present heat exchanger technology. The combustion gases are therefore diluted with previously generated and cooled combustion gas. This recirculation, in addition, provides burner component cooling.

The cycle associated with the gas generation system can have many variations depending upon the required delivery pressure and process rate. The selection of these parameters is intimately related to the field application and its requirements. As examples, three basic cycles were investigated wherein attention was focused on the interrelationship, between the gas production and shaft power requirements for both the gas production and processing, and possible electric generator power.

The cycles considered included two gas-storage systems, with the laser gas system being either open or closed cycle, and an on-line, open-cycle system, wherein the gas production rate equals the laser system gas flow requirements. The storage systems reduce the gas production rate thereby reducing the associated equipment weight and volume. However, there is an inherent laser system shutdown period for a given operating time. The ratio of these quantities is termed the duty cycle.

The closed-cycle laser gas system could be on-line generation system. However, in the closed-cycle system considered, gas storage was utilized because of start-up requirements. The gas pressure during processing has a significant impact on cooling and subsequent water removal. It is possible that for on-line, closed-cycle operation, very little pressurization is required (laser cavity operation at one atm), if water removal is provided by methods utilizing desiccants, for instance.

4.2 SUMMARY

Figure 49 presents simplified schematics of the laser gas production system and its relation to the laser gas system, including power generation. Gas turbine drives have been considered, which provide minimum weight for extended laser operating time. This prime mover (gas turbine) is not as attractive as a chemical turbine for quick starts, which suffer from excessive propellant (fuel and oxidizer or monopropellant) requirements and, in addition are not presently as attractive in the field (logistics). However, the exhaust products from the chemical turbine are highly hazardous compared with that of the gas turbine, where nearly ideal combustion within the power generation system is realized.

Table 5 summarizes the results of the study comparing three gas production systems with cold laser gas generated in terms of weight, volume, fuel expended and other characteristics, which while reflecting the power system for generating electrical power does not include the alternator nor its gear box.

The stored gas, open-cycle laser gas operation has a 15-sec firing capability with a duty factor of 50. The total weight of this system is considerably less than that of the other systems considered.

The stored gas, open-cycle system provides power for the alternator drive. The energy in the compressed gas is utilized in an expansion turbine. In order to match the alternator power requirements, the laser gas is heated by means of a heat exchanger in the gas generator prime mover exhaust. An afterburner is provided to increase the temperature difference, thereby minimizing heat exchanger requirements.

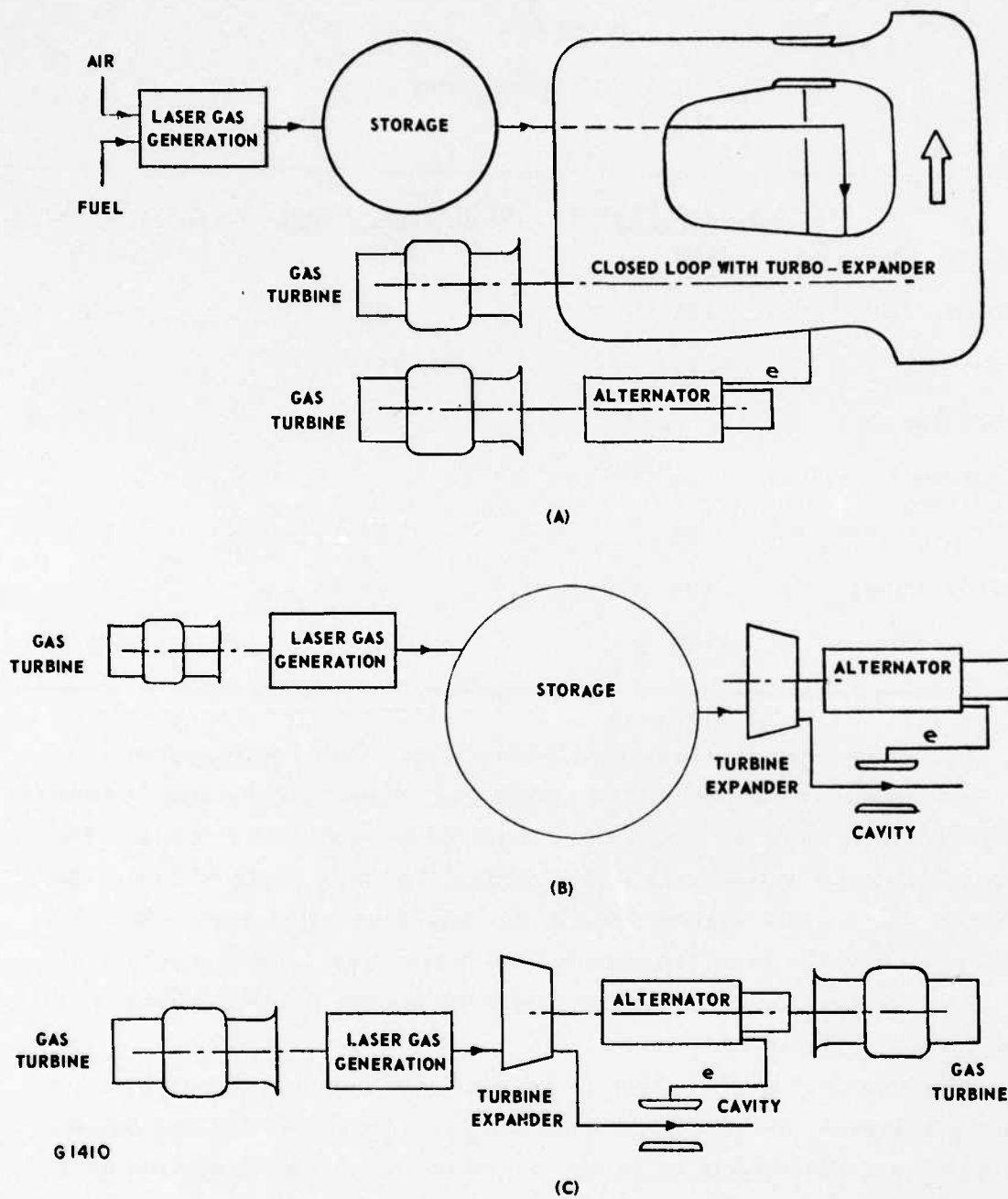


Fig. 49 Simplified Schematics of Gas Turbine Type Gas Generation Systems

TABLE 5
CYCLE COMPARISON

	(a) <u>Storage, Closed</u>	(b) <u>Storage, Open</u>	(c) <u>On-Line, Open</u>
FSS Weight (lbs)	3892	1669	3280
Volume (CF)	194	59	80
Cost (K\$)	1141	331	984
Fuel (lb/sec)	1.40	.16	2.84
Fuel for 1 min. firing (lb)	84	49	170
Air (lb/sec)	191	16.4	292
Power (Shp)	11179	627	10260

The stored gas, closed-cycle and on-line, open-cycle system can operate continuously whereas, the stored gas, open-cycle system is limited by the duty cycle, because of the time required to replenish the gas in the storage tank after its use in the firing mode. The duty cycle of 50 for the stored gas, open-cycle system results in a gas generation system which is consistent with the requirements for the stored gas, closed-cycle system. The laser gas flow rate in the cavity during the firing mode is 26.7 lb/sec for all systems considered.

The stored gas, closed-cycle system requires substantially larger packaging volumes, due to the recirculating ducts and rotating equipment. The stored gas, open-cycle laser gas operation needs only a portion of the air (necessary for processing, conditioning, and prime mover) required by the other cycle systems; in addition, its power requirements are substantially less, while still providing external power to drive the alternator. The costs indicated in Table 5 are estimated on the basis of 100 units, and also reflect an advantage of the stored gas, open-cycle system.

The variation of the system weights with laser firing time is dominated by the fuel expended both in providing power, and in generating laser gas. Figure 50 illustrates the variation in the total gas system weight with firing time indicating the regimes of apparent superiority for the three systems investigated. Similarly, Fig. 51 presents the volume variation. Two alternatives are possible; i. e., either stored gas, open-cycle (total firing time less than 300 sec) or stored gas, closed-cycle system (firing time greater than 300 sec). The on-line, open-cycle system is competitive with the other two systems over a restricted operating time. In terms of minimum volume, however, the on-line, open-cycle system becomes attractive after 250-sec continuous firing time. The closed-cycle volume advantage does not occur until 4000-sec continuous firing.

In summary, the results indicated the desirability of the stored-gas, open-cycle system. However, it has performance limitations imposed by the duty factor. With extended firing time requirements then fire vehicle considerations in terms of weight or volume limitations may determine the system selected. An additional factor favoring the stored gas, open-cycle system is the fuel requirement (already included as part of the weight and volume advantage).

4.3 FIELD APPLICATION OF EACH CYCLE SYSTEM

Further details on the systems investigated are presented below providing information on the components and their functional inter-relationship within the system.

4.3.1 Stored Gas, Closed-Cycle System

The detailed schematic for this system is presented in Fig. 52. The stored gas, closed-cycle system consists of two sections: a gas generation section, and a closed-cycle, fluid supply section. The gas generation section is sized for a production rate of 0.58 lb/sec, which is about 2 percent of the laser gas flow rate of 26.7 lb/sec during firing. It is separately driven by a small turbo-shaft engine, such as the Avco-Lycoming LTS 101. The closed-cycle, fluid supply section has three compressor stages with air-cooled interstage compact heat exchangers. For 1-sec start-up time, it must be powered by a chemical turbine. If

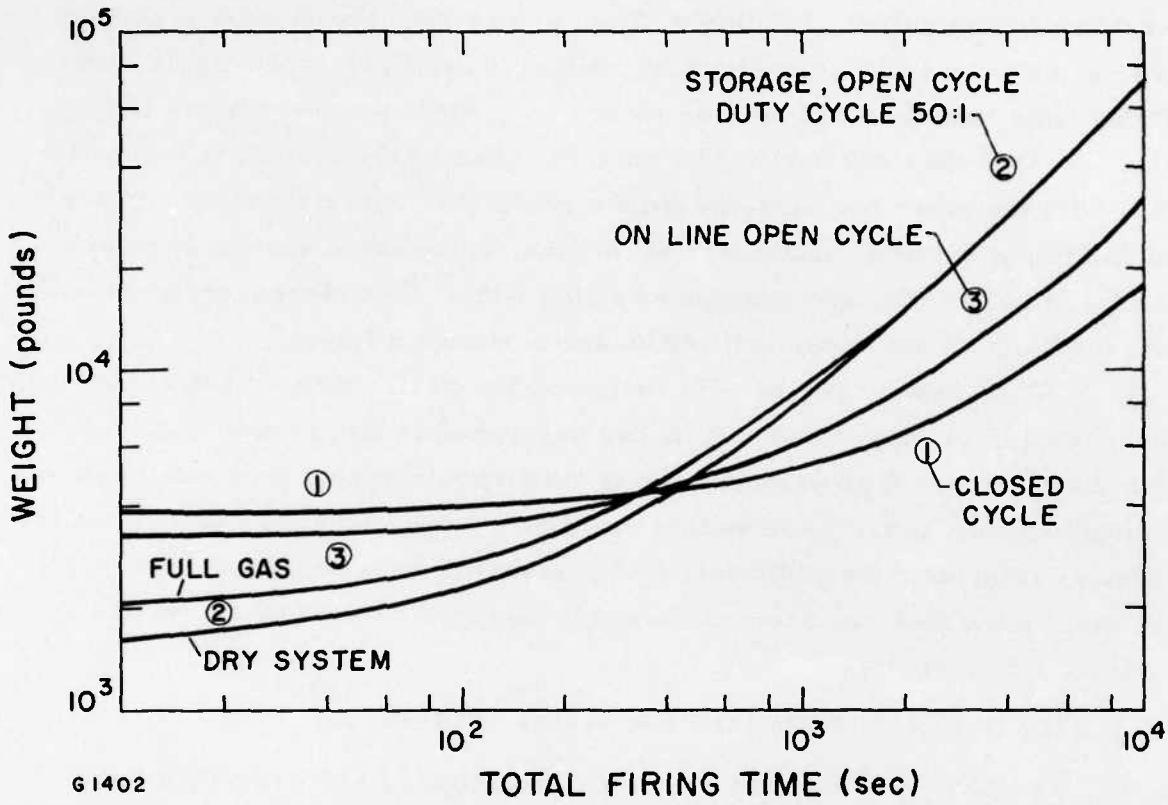


Fig. 50 Variation in Total Gas Systems Weight, 25 lb/sec FSS

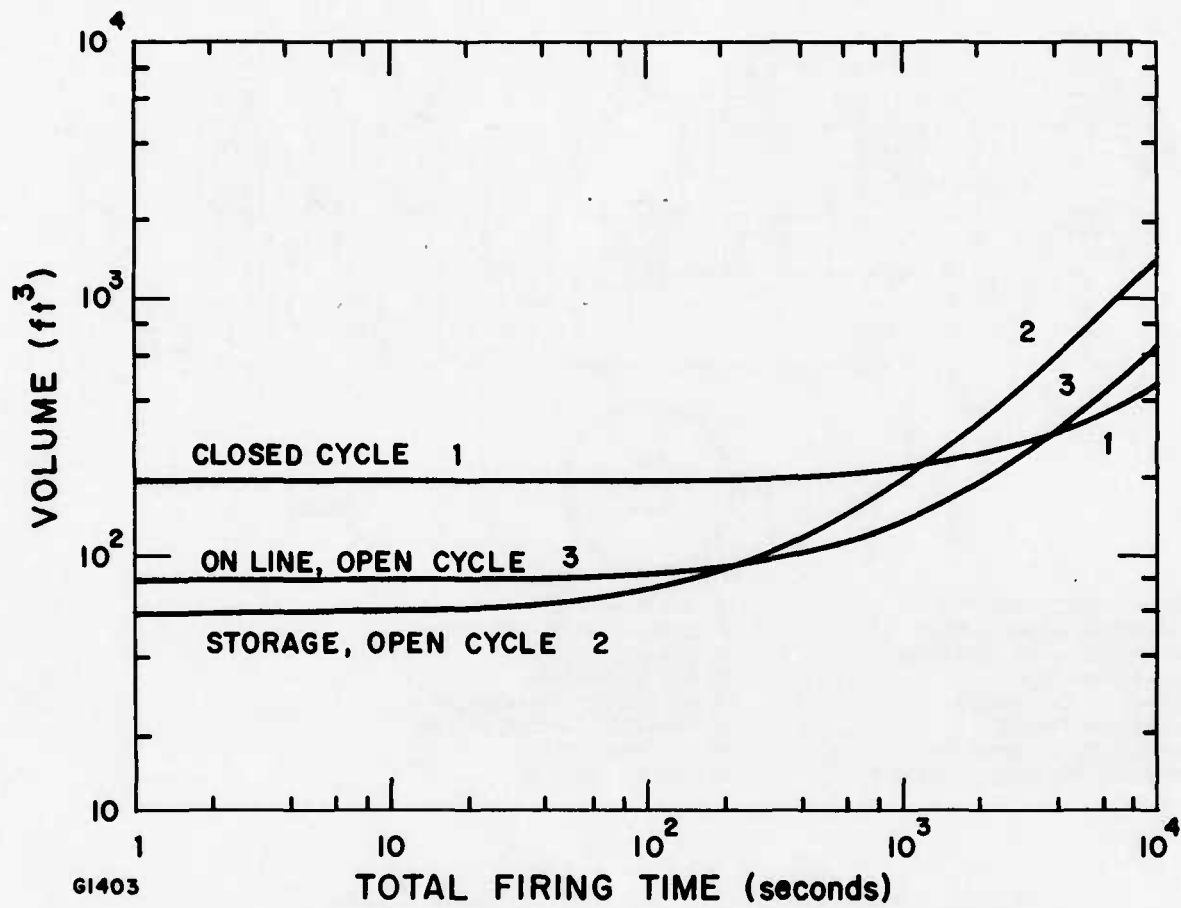
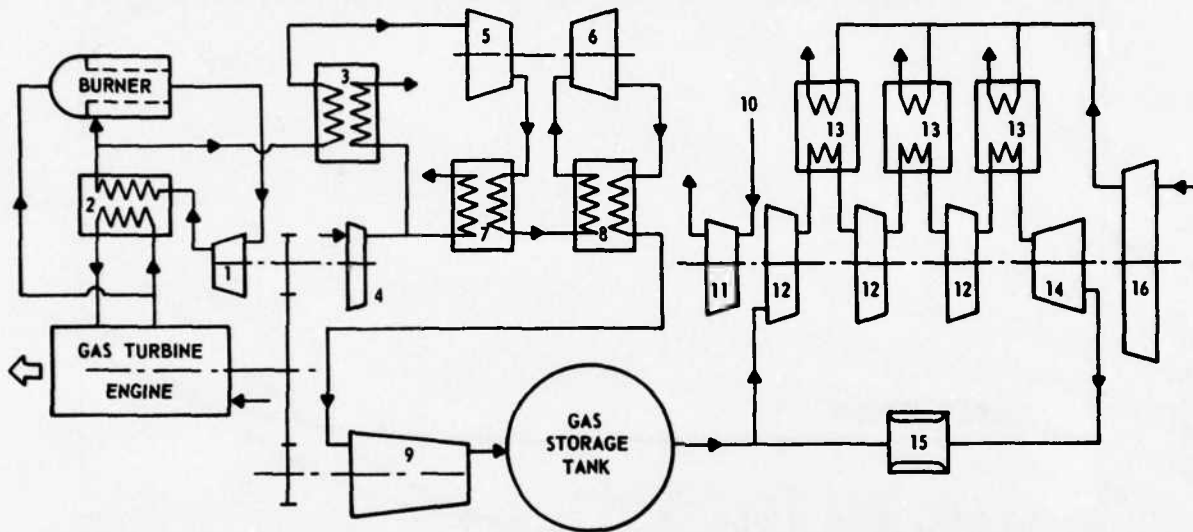


Fig. 51 Variation in Operational System Volume, 25 lb/sec FSS



- | | |
|--------------------------------|------------------------------|
| 1. BURNER CIRCULATION FAN | 9. GAS COMPRESSOR |
| 2. GAS ENGINE REGENERATOR | 10. CHEMICAL FUEL GENERATOR |
| 3. AIR COOLED HEAT EXCHANGER | 11. CHEMICAL TURBINE |
| 4. COOLING AIR FAN | 12. GAS COMPRESSORS |
| 5. BOOTSTRAP COMPRESSOR | 13. AIR COOLED INTERCOOLERS |
| 6. BOOTSTRAP TURBINE | 14. EXPANSION TURBINE COOLER |
| 7. AIR COOLED INTERCOOLER | 15. LASER CAVITY |
| 8. REGENERATIVE HEAT EXCHANGER | 16. COOLING AIR FAN |

61400

Fig. 52 Schematic-Stored Gas, Closed Cycle

longer start-up periods are acceptable, a turbo-shaft engine, fueled with JP-4, will give weight economy for long firing times. The expansion turbine in the closed-cycle cools the laser gas to 200°K and returns power to the turbo-shaft, keeping the compressor power requirement down to about 5000 shp. An additional 5600 shp is required to drive the alternator for electric power generation.

Table 6 lists the system components and their weight, volume, fuel and air consumption.

4.3.2 Stored Gas, Open-Cycle System

Figure 53 gives the system diagram including the alternator and cavity components.

The stored gas, open-cycle system consists of two sections: a gas generation section and a blowdown section. The gas generation section is sized for a production rate of 0.58 lb/sec, as in the previous system. This rate allows firing of the laser at a duty cycle rate of 50:1.

The blowdown section consists of the high pressure gas storage tank, a heat exchanger at the gas turbine exit of the gas generator, an afterburner for the same, and an expansion turbine coupled to the alternator. The stored energy of the high pressure gas storage is utilized both to cool the laser gas and to provide additional power by means of the turbo-expander. Heat addition to the high pressure gas is required in order to increase the power output from the turbine. This is done by a compact heat exchanger in the exhaust gas stream of the turbo-shaft engine of the gas generator. During firing, the enthalpy of the exhaust gas is raised by the afterburner to offset the small heat capacity rate of the engine exhaust. At the same time, a high heat exchanger efficiency is obtained, which minimizes the heat exchanger weight and volume. The components are sized such that all power, required for the alternator, is provided by the expansion turbine for a laser gas flow rate of 26.7 lb/sec.

The above approach to gas conditioning effectively eliminates the requirement for about 10,000 shp of on-line power for cooling and electric power generation. The disadvantage of this approach is the introduction of a duty cycle, rather than continuous operation. If a reasonable duty cycle is acceptable, however, remarkable weight, volume and cost savings are realized with this system.

TABLE 6
STORED-GAS, CLOSED-CYCLE SYSTEM BREAKDOWN

	<u>Weight (lb)</u>	<u>Volume (ft³)</u>	<u>Fuel lb/sec</u>	<u>Air lb/sec</u>	<u>Cost (K\$)</u>
Gas Turbine (LTS 101)	180	6.74	0.100	4.2	55.0
Burner	36.4	.87	0.058		4.8
Burner Circulation Fan	9.1	1.07			1.2
Gas Engine Regenerator	64.9	3.16			6.3
Air Cooled Heat Exchanger	50.0	8.63			17.3
Cooling Air Fan	13.1	1.25		20.5	1.7
Bootstrap Compressor	7.0	.10			2.1
Bootstrap Turbine	6.5	.09			2.0
Air Cooled Intercooler	4.6	.48			1.0
Regenerative Heat Exchanger	12.2	3.24			6.5
Gas Compressor	38.1	.32			60.0
Miscellaneous, Gas Generator	<u>100.0</u>	<u>3.00</u>	_____	_____	<u>6.0</u>
Sub Total, Gas Generator	522.0	29.00	0.158	20.5	164.0
Gas Turbine (FSS)	590.0	16.00	0.584	33.4	300.0
Gas Compressors (3)	510.0	6.00			182.0
Air Cooled Intercoolers (3)	660.0	30.00			60.0
Expansion Turbine	90.0	1.00			32.0
Cooling Air Fan	210.0	12.0		100.0	28.0
Tunnel	420.0	75.0			67.0
Gas Storage	50.0	5.0			8.0
Gas Turbine (Alternator)	590.0	16.0	0.654	37.4	300.0
Miscellaneous	<u>250.0</u>	<u>4.0</u>	_____	_____	_____
TOTAL	3,892.0	194.0	1.396	191.3	1141.0

Table 7 lists the system components and their weight, volume, fuel and air consumption.

Figure 54 gives the shp output of an expansion turbine for 26.7 lb/sec gas flow rate as a function of blowdown pressure. It also gives the preheat temperature required for the gas in order to achieve a temperature of 200°K at the turbine exit. A novel gas storage tank concept has been analyzed for possible use in this cycle. This concept and analysis is presented in Appendix A.

4.3.3 On-Line, Open-Cycle System

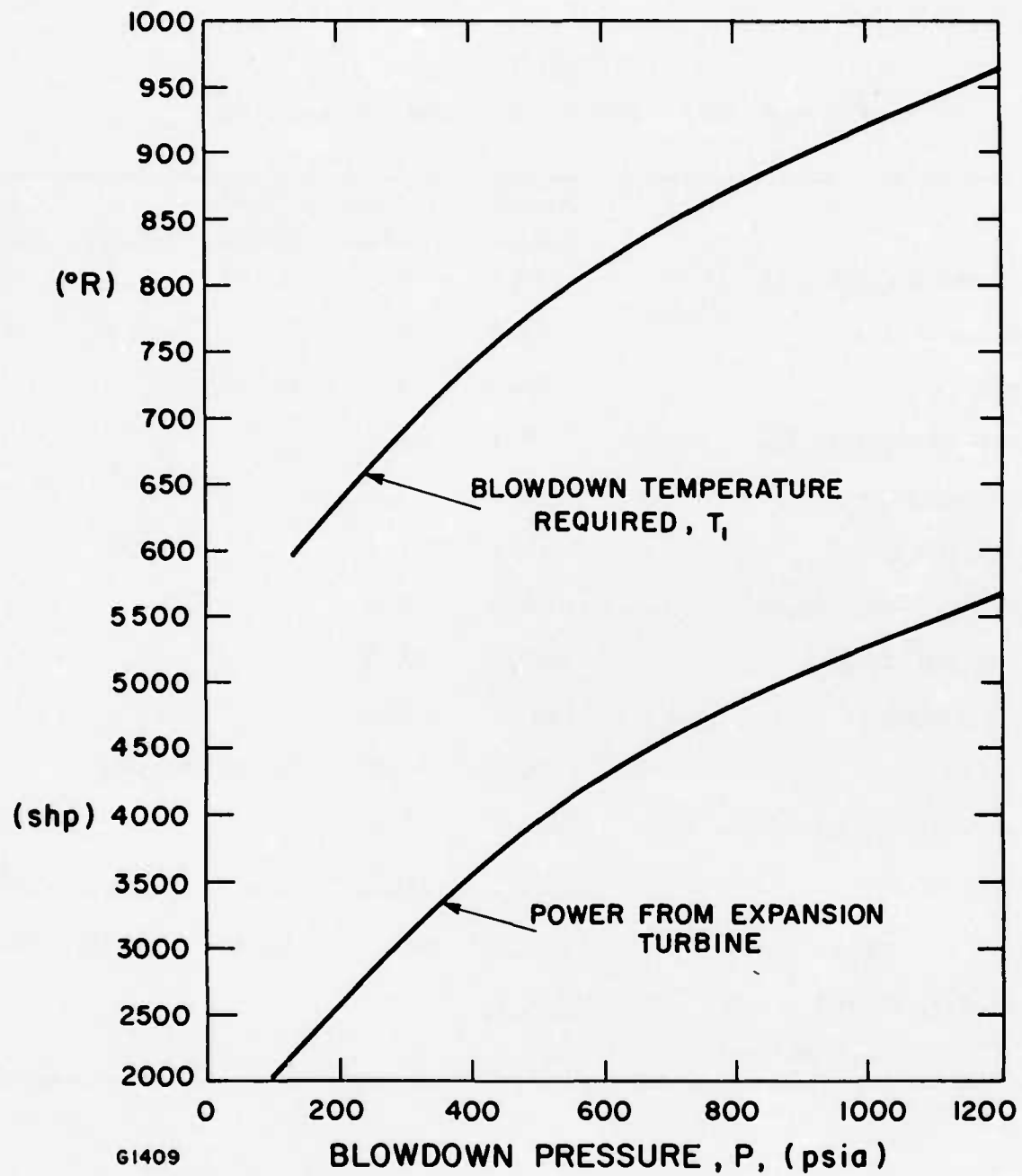
Figure 55 shows the system diagram and the alternator and cavity components.

The on-line, open-cycle system consists of the turbo-shaft gas turbine engine power plant, the gas generation section and an expansion turbine with de-icer. All laser gas is produced on-line and the gas generation rate is thus 50 times larger than in the previous systems. A periodic heat regenerator has been introduced to cool the burner gases. It consists of a rotating ceramic disc and affords a substantial weight saving over a compact heat exchanger. Discussions with Ford Motor Corporation and Corning Glass Works indicate that 15-atm operating pressure for the burner leads to a regenerator that is not at the present state-of-the-art. A compact heat exchanger at this location would nearly triple the weight of this item. This will further increase the weight of this heaviest of systems investigated. The required cooling air flow is substantial and in the analysis came out as 8 times the laser gas flow rate. The burner recirculation gas flow rate is 3 times the laser gas flow rate.

Table 8 lists the system components and their weight, volume, fuel and air consumption.

TABLE 7
STORED-GAS, OPEN-CYCLE SYSTEM BREAKDOWN

	<u>Weight (lb)</u>	<u>Volume (ft³)</u>	<u>Fuel lb/sec</u>	<u>Air lb/sec</u>	<u>Cost (k\$)</u>
Gas Turbine (LTS 101)	180.0	6.8	0.100	4.2	55.0
Air Compressor	38.1	0.3		0.58	11.6
Burner	36.4	0.9	0.058		4.8
Burner Circulation Fan	9.1	1.1			1.2
Heat Exchanger	50.0	8.6			17.2
Air Cooling Fan	13.1	1.3		11.6	1.7
Laser Gas Compressor	60.0	1.0			80.0
Gas Storage Tank	380.0	24.0			60.8
Heat Exchanger	432.0	6.6			13.2
After Burner	20.0	1.0	0.1/DF=0.002		6.1
Expansion Turbine	200.0	3.2			71.4
Miscellaneous	<u>250.0</u>	<u>4.0</u>	_____	_____	<u>8.0</u>
Dry Weight	1669.0	58.8	0.16	16.38	331.0
Laser Gas, Stored	<u>420.0</u>				
Wet Weight	2089.0				



61409

Fig. 54 Stored Gas, Open Cycle

TABLE 8

ON-LINE, OPEN-CYCLE SYSTEM BREAKDOWN

	<u>Weight (lb)</u>	<u>Volume (ft³)</u>	<u>Fuel lb/sec</u>	<u>Air lb/sec</u>	<u>Cost (K\$)</u>
Gas Turbine (LTC 4V-1) 2 Units	1180	31.4	1.167	66.7	600.0
Air Cooling Fan, 1695 shp	100	12.0		200.0	35.7
Rotary Heat Exchanger	950	13.6			27.2
Air Compressor, 7180 shp	335	5.3		25.0	
Burner	195	5.0	1.67		300.0
Burner Circulation Fan, 266 shp	20	1.0			
Expansion Turbine, 2460 shp	150	2.4			
De-Icer	100	5.0			13.3
Miscellaneous	<u>250</u>	<u>4.0</u>			<u>8.0</u>
	3280	79.7	2.84	291.7	984.0

REFERENCES

1. Douglas-Hamilton, D.H., Feinberg, R.M. and Lowder, R.S., "Experimental and Theoretical Electron-Beam-Sustained CO₂ Laser Output at ~200 and ~300°K," *J. Appl. Phys.* 46, 3566 (1975).
2. Douglas-Hamilton, D.H. and Lowder, R.S., AERL Kinetics Handbook, Avco Everett Research Laboratory, Everett, Massachusetts 02149 (1974).
3. Smith, M.L. and Stinson, R.W., Fuels and Combustion (McGraw Hill, New York, 1952).
4. Douglas-Hamilton, D.H., Sutton, G.W., Westra, L. and Lowder, R.S., "Air-Combustion Product N₂-CO₂ Electric Laser," *J. Appl. Phys. Lett.* 26, 373 (1975).
5. Miller, D.J. and Millikan, R.C., "Vibrational Relaxation of Carbon Monoxide by Hydrogen and Helium down to 100°K," *J. Chem. Phys.* 53, 3384 (1970).
6. Douglas-Hamilton, D.H. and Mani, S.A., "Attachment Instability in an Externally Ionized Discharge," *J. Appl. Phys.* 45, 4406 (1974).
7. Wickramasinghe, N.C., Light Scattering Functions for Small Particles, (Adam Hilger, Ltd., London) Chap. 3, p. 25.
8. Weyl, G., "IRAD Report," Avco Everett Research Laboratory, Everett, Massachusetts 02149, February 1975.
9. Carslaw, H.S. and Jaeger, J.C., Heat Conduction in Solids, (2d ed., Oxford-Clarendon Press, 1959).
10. Lencioni, D.E., "The Effect of Dust on 10.6 μm Laser-Induced Air Breakdown", *Appl. Phys. Lett.* 23, 12 (1973).
11. Jacob, J.H., Pugh, E.R., Daugherty, J.D. and Northam, D.B., "An Absolute Method of Measuring Energy Outputs from CO₂ Lasers," *Rev. Sci. Instrum.* 44, 471 (1973).

APPENDIX A
THE STABLE VESSEL -
A NEW TYPE PRESSURE VESSEL

APPENDIX A

THE STABLE VESSEL - A NEW TYPE PRESSURE VESSEL

The stable pressure vessel is designed to allow stresses in the vessel wall that exceed the yield stress and approach the ultimate tensile stress of the wall material. Stable vessels are lighter, safer and stronger than conventional pressure vessels.

Conventional pressure vessels rarely exceed the yield stress in the vessel wall. To insure long life in pressure cycling applications, a typical design goal is a wall stress of about half the yield stress. Conventional vessels become unstable when loaded beyond the yield point and burst.

Interior tie-plates are used in construction of the stable pressure vessel. Therefore, the stable vessel is most useful for storage, where tie-plates will not interfere with other requirements. A well-designed joint between the tie-plates and the pressure vessel wall is essential to insure ultimate success of the concept.

Tie-plates provide stationary anchor lines for mounting stressed pressure vessel walls, a necessity for achieving an inverse change of radius of curvature with increased pressure. The rigidity of the tie-plates controls the radius of curvature of the deflecting vessel wall. Increasing wall deflection produces a shorter radius of curvature rather than a longer radius, as in conventional pressure vessels. As a result, the stress in the pressure wall is stabilized.

The tie-plate concept is applicable to both cylindrical and spherical pressure vessels. In each, crossed tie-plates (at 180° to each other) are used. For cylindrical vessels, a pair of crossed tie-plates is used. Six crossed tie-plates in the spherical vessel create the shape of a cube.

Figure A-1 ties pressure vessel stability to the dimensionless parameter σ_t/P_r for a cylindrical vessel and its change, as a function of increasing elongation in the pressure vessel wall for conventional and stable pressure vessels.

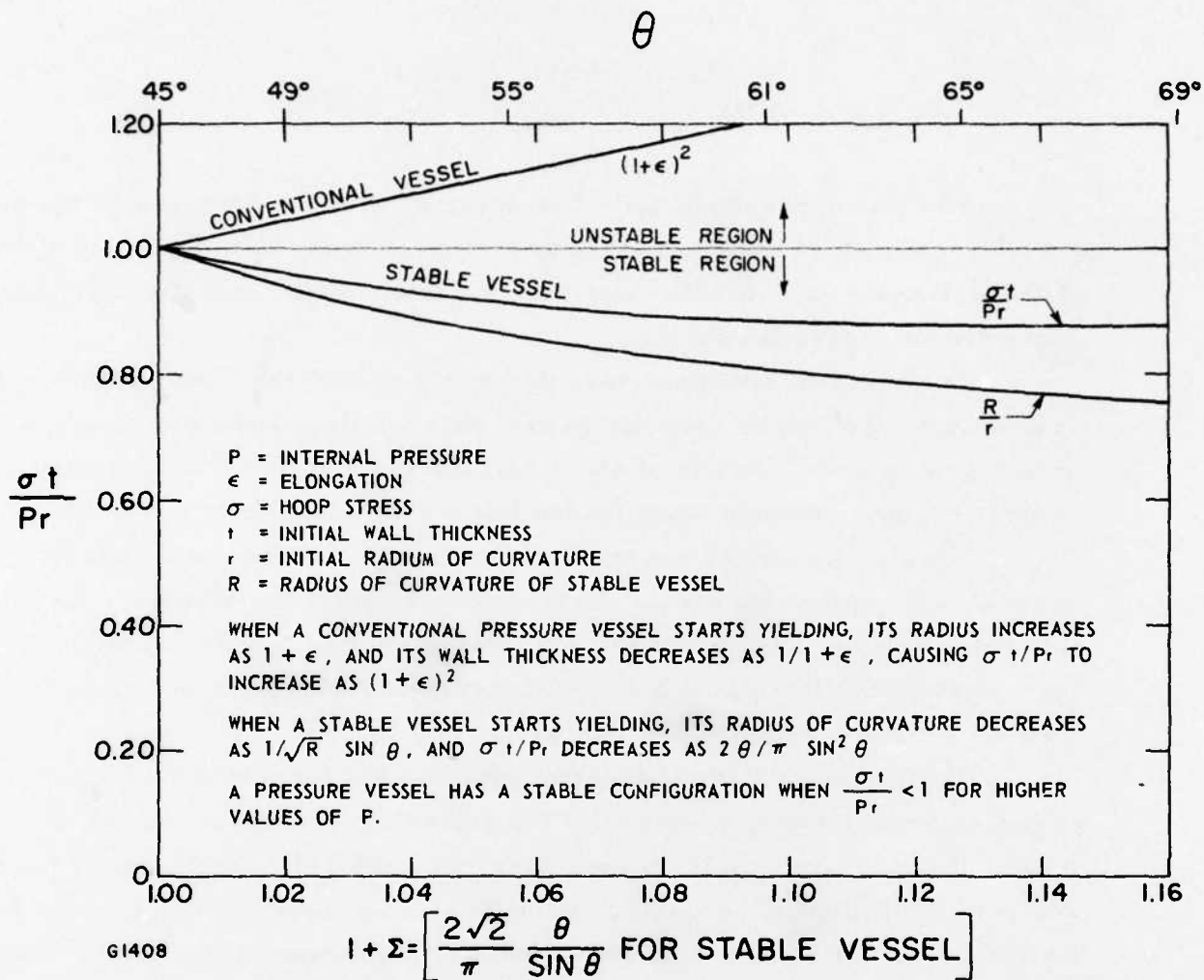


Fig. A1 Pressure Vessel Stability Criterion

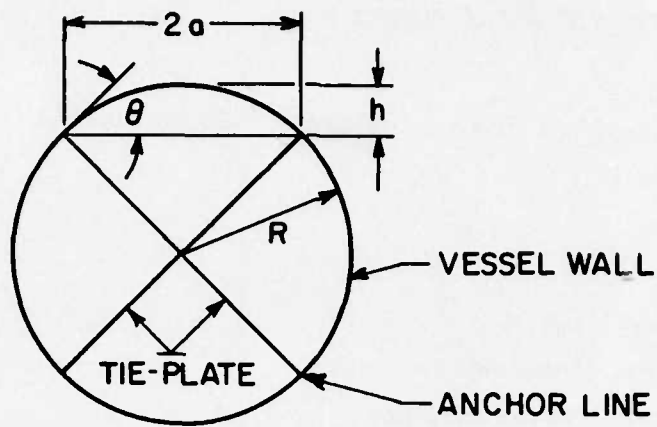


Fig. A2 Dimension Identification for Derivation of Tie-Plate Force Formulas

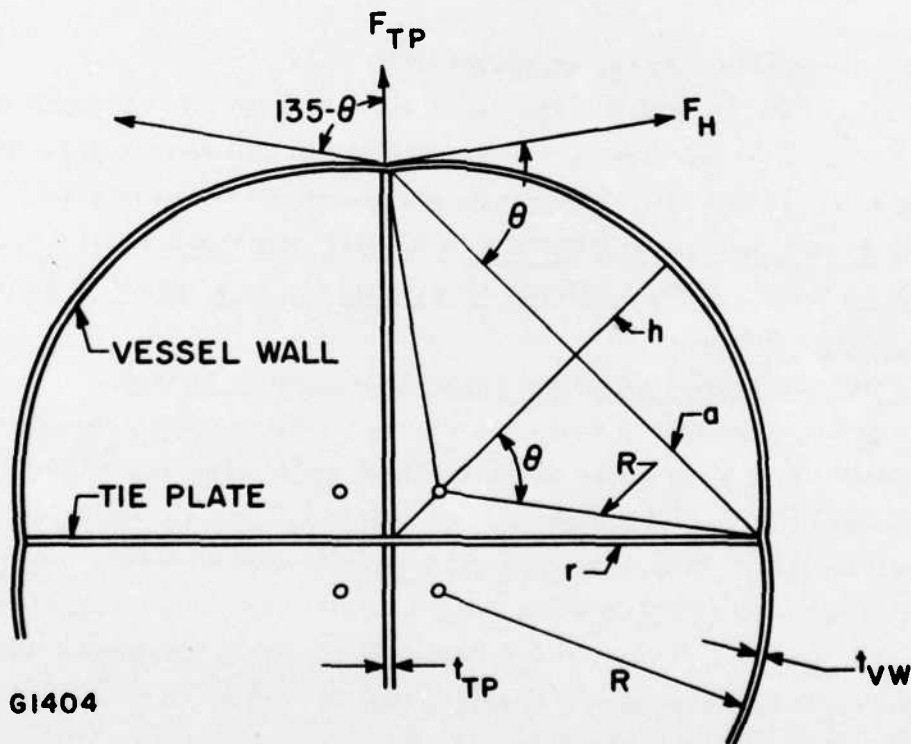


Fig. A3 Dimension Identification for Derivation of Tie-Plate and Vessel Wall Thickness, Weight and Volume

1.0 CYLINDRICAL STABLE VESSEL

1.1 Introduction

The hoop stress in a cylindrical pressure vessel is given by Rankine's formula:

$$\sigma = \frac{RP}{t}$$

where

σ = stress, psi

R = radius of curvature, inch

P = internal pressure, psi

t = wall thickness, inch

For safe design, the ASME pressure vessel code, Section VIII, 1974 edition, requires:

$$t = \frac{PR}{S - 0.5P}$$

where

S = membrane stress intensity limit, psi

S is typically given as 1/2 the specified minimum tensile strength for the wall material. A stable vessel on the other hand can have values for S, which are close to the ultimate tensile stress of the wall material.

An actual test on ALUMINUM 5052-H19 withstood 34, 100 cyclic loads from 0 to 90% of the ultimate tensile stress at a rate of 2 cycles per minute without failure.

1.2 Weight Comparison with Conventional Pressure Vessels

In order to render a cylindrical vessel stable, two crossed tie-plates are required. For a tie-plate thickness that equals the vessel wall thickness, the contribution to vessel weight for an infinitely long vessel is $2D/\pi D$ times vessel wall weight. The stable vessel weight is now $\frac{(2 + \pi)}{\pi} \times \frac{1/3}{0.9} = 1.637 \times 0.3704 = 0.606$ times the weight of a conventional vessel (zero corrosion). A stable vessel with a design that allows tie-plates with half the vessel wall thickness gives a weight that is $\frac{(1 + \pi)}{\pi} \times \frac{1/3}{0.9} = 0.488$ times the weight of a conventional vessel.

1.3 Safety Factor

The issue, that must be addressed is: What is the safety factor for a stable vessel that is loaded to 90 percent of the tensile strength?

The safety factor of the ASME pressure vessel code is based on the endurance limit and a corrosion allowance. Its value is between 3 and 4 and expresses the ratio of the load stress and the ultimate tensile stress. A safety factor for the stable pressure vessel based on this ratio does not do justice to the inherently safe construction of this vessel. It would be more appropriate to experimentally determine the endurance limit of stable pressure vessels and relate the conventional safety factor to the above stress ratio of the stable pressure with a conversion formula.

The tie-plates are conventionally stressed and must be designed with the conventional safety factor.

If we assume that the stable vessel wall loading to 90 percent of the ultimate tensile stress gives an infinite number of life cycles and constitutes the endurance limit, then the conversion formula for the wall safety factor can be expressed as a power function

$$\left[SF_{\text{Stable}} \right]^n = \left[\frac{\sigma_{\text{ultimate}}}{\sigma_{\text{wall load}}} \right]^n = SF_{\text{Conv.}} = 3$$

$$\left[\frac{1}{0.9} \right]^n = 3$$

$$n \approx 10$$

Hence

$$SF_{\text{Stable}}^{10} = SF_{\text{Conv.}}$$

And

$$SF_{\text{Stable}} = \left[SF_{\text{Conv.}} \right]^{0.0959} \approx SF_{\text{Conv.}}^{0.1}$$

1.4 Analysis

The following formulas apply in stable cylindrical vessel analysis:

$$\sigma = \frac{PR}{t} (1 + \epsilon) \tag{A-1}$$

$$R = \frac{a^2 + h^2}{2h} = \frac{r \times \sqrt{2}}{2 \sin \theta} \tag{A-2}$$

$$1 + \epsilon = \frac{R}{a} \arcsin \frac{a}{R} = \frac{\theta}{\sin \theta} \tag{A-3}$$

The following assumptions were made: When the vessel was constructed, all vessel walls were originally flat. After assembly, the walls are yielded into a desired curved shape by pressurization. It is desirable to have the tie-plates in tension, rather than compression. This requirement is satisfied for $\theta > 45^\circ$. In this case $1 + \epsilon = \frac{\pi}{2\sqrt{2}} = 1.11072$ and the

maximum elongation for the vessel wall material must exceed 11.072 percent in order to avoid rupture. Materials with a lower elongation limit can be used only if the walls are preformed as a cylindrical roll-up. The previous formulas are modified for this case as follows:

$$\sigma = \frac{PR}{t} (1 + \epsilon) \quad (\text{A-1a})$$

$$R = \frac{a^2 + h^2}{2h} = \frac{r\sqrt{2}}{2 \sin \theta} \quad (\text{A-2a})$$

$$1 + \epsilon = \frac{2\sqrt{2}}{\pi} \frac{R}{a} \arcsin \frac{a}{R} = \frac{2\sqrt{2}}{\pi} \frac{\theta}{\sin \theta} \quad (\text{A-3a})$$

1.4.1 Derivation of Formulas

As indicated above, it is desirable to keep the tie-plates in tension and $\theta > 45^\circ$. The force in the tie-plates is due to the hoop forces in the vessel walls, and can be expressed as follows:

$$\frac{F_{\text{tie-plate}}}{L} = Pr\sqrt{2} \frac{\theta \sin(\theta - 45)}{\sin^2 \theta}$$

where L is the vessel length that is being considered.

Derivation of the tie-plate force formula:

$$\begin{aligned} \frac{F_{\text{TP}}}{L} &= 2 \frac{F_H}{L} \cos(135 - \theta) \\ &= 2 \sigma_H t \sin(\theta - 45) \\ &= 2 PR (1 + \epsilon) \sin(\theta - 45) \\ &= 2 PR \frac{R}{a} \theta \sin(\theta - 45) \text{ or } 2 PR \frac{2\sqrt{2}}{\pi} \frac{R}{a} \theta \sin(\theta - 45) \\ &= 2 Pa \left[\frac{R}{a} \right]^2 \theta \sin(\theta - 45) \\ &= Pr \sqrt{2} \frac{\theta \sin(\theta - 45)}{\sin^2 \theta} \end{aligned}$$

1.4.2 Tie-Plate Thickness, Weight

The tie-plate thickness is obtained by allowing a safety factor of 3:

$$t_{TP} = \frac{\frac{F_{TP}}{L}}{\frac{\sigma}{3}} = \frac{Pr}{\sigma} 3\sqrt{2} \frac{\theta \sin(\theta - 45)}{\sin^2 \theta}$$

The tie-plate weight is:

$$W_{TP} = 4r t_{TP} L \rho = \frac{\rho Pr^2 L}{\sigma} 12\sqrt{2} \frac{\theta \sin(\theta - 45)}{\sin^2 \theta}$$

1.4.3 Vessel Wall Thickness Weight

The vessel wall thickness is obtained by allowing a stress load of 0.9σ for a wall that is made as a roll-up:

$$\begin{aligned} t_{VW} &= \frac{\frac{F_H}{L}}{0.9\sigma} (1 + \epsilon) = \frac{Pa}{0.9\sigma} \frac{R}{a} \frac{\theta}{\sin \theta} \frac{2\sqrt{2}}{\pi} \\ &= \frac{Pr 4 \theta}{1.8 \pi \sigma \sin^2 \theta} \end{aligned}$$

The vessel wall weight is:

$$\begin{aligned} W_{VW} &= 4t_{VW} R^2 \theta L \rho = \frac{4t r \sqrt{2} \theta L \rho}{\sin \theta} \\ &= \frac{8\sqrt{2} \rho Pr^2 L \theta^2}{0.9 \pi \sigma \sin^3 \theta} \end{aligned}$$

1.4.4 Vessel Weight

The total vessel weight, excluding the ends, becomes:

$$W_{total} = W_{TP} + W_{VW} =$$

$$\frac{\rho Pr^2 L \theta}{\sigma \sin^2 \theta} \left[12\sqrt{2} \sin(\theta - 45) + \frac{8\sqrt{2} \theta}{0.9 \pi \sin \theta} \right]$$

The optimum weight exists for a value of θ that minimizes W_{total} . In the above formula, this value is $\theta = 45^\circ$. The required tie-plate thickness is then $t = 0$. This defeats the intention of having the tie-plate provide the anchor points for the vessel wall membranes. Instead, we will introduce an optimal design philosophy.

1.4.5 Vessel Volume

The cross section, and therefore volume, increases as θ increases.

$$\begin{aligned}V &= AL = \left[(2a)^2 + 4 \frac{R^2}{2} (2\theta - \sin 2\theta) - 4rt_{TP} \right] L \\&= \left[2r^2 + 2a^2 \frac{R^2}{a^2} (2\theta - \sin 2\theta) - 4rt_{TP} \right] L \\&= \left[2r^2 + r^2 \frac{1}{\sin^2 \theta} (2\theta - \sin 2\theta) - 4rt_{TP} \right] L \\&= r^2 L \left[2 + \frac{2\theta}{\sin^2 \theta} - \frac{2}{\tan \theta} - 4 \frac{t_{TP}}{r} \right]\end{aligned}$$

1.5 Optimal Design Philosophy

The design of a stable pressure vessel can be summarized as follows. The material selection with given maximum elongation determines the burst value of θ . By requiring that the tie-plates reach the yield point at the burst pressure, the ratio of the thickness of the tie-plates and vessel wall are known. Safety factors are now imposed to express the safe operating pressures for the tie-plate and vessel wall in terms of θ . By equating one safe operating pressures the operating value of θ is calculated. The correct wall thickness can now be calculated from the required operating pressure for the vessel. The burst pressure follows.

1.6 Calculation Example of a Stable Pressure Vessel

Material selection:

titanium 6 Al 4V

$$\sigma_T = 165,000 \text{ psi}$$

$$\sigma_Y = 120,000 \text{ psi}$$

$$\epsilon = 10 \text{ percent}$$

The vessel wall is to be prefabricated as a roll-up, therefore:

$$1 + \epsilon = \frac{2\sqrt{2}}{\pi} \frac{\theta}{\sin \theta}$$

The maximum value of ϵ gives the burst value for θ of $61.55^\circ = 1.07425$ radian. The requirement $\sigma_{TP} = \sigma_Y = 120,000$ gives for the tie-plate thickness:

$$t_{TP} = \frac{Pr}{120,000} \sqrt{2} \frac{\theta}{\sin^2 \theta} \sin(\theta - 45)$$

The requirement $\sigma_{VW} = \sigma_T = 165,000$ gives for the vessel wall thickness:

$$t_{VW} = \frac{Pr}{165,000} \frac{2}{\pi} \frac{\Theta}{\sin^2 \Theta}$$

Hence:

$$t_{TP}/t_{VW} = \frac{\pi \sqrt{2} \times 165,000}{2 \times 120,000} \sin(61.55 - 45) = 0.870$$

The safety factor for the tie-plates is 3; $\sigma_{TP} = 55,000$ psi

The safety factor for the vessel wall is 0.9; $\sigma_{VW} = 148,500$ psi

Equating the safe operating pressures for the tie-plates and the vessel wall:

$$\frac{55,000 t_{TP}}{r\sqrt{2} \sin(\Theta - 45)} \frac{\sin^2 \Theta}{\Theta} = \frac{\pi}{2} \frac{148,500 t_{VW}}{r} \frac{\sin^2 \Theta}{\Theta}$$

$$\sin(\Theta - 45) = \frac{55,000}{148,500} \frac{t_{TP}}{t_{VW}} \frac{2}{\pi\sqrt{2}} = 0.1667 \times 0.870 = 0.145067$$

$$\Theta = 53.341^\circ = 0.93098 \text{ radian}$$

The desired vessel wall thickness for an operating pressure of 2000 psi and $r = 12$ inch

$$t_{VW} = \frac{2 Pr}{\pi} \frac{\Theta}{\sin^2 \Theta} = \frac{2 \times 2000 \times 12}{\pi \times 148,500} \frac{0.93098}{\sin^2 53.341} \\ = 0.149 \text{ inch}$$

The tie-plate thickness is

$$t_{TP} = 0.870 t_{VW} = 0.130 \text{ inch}$$

The burst pressure

$$P_{burst} = \frac{\pi}{2} \frac{165,000}{12} 0.149 \frac{\sin^2 61.55}{1.07425} = 2315 \text{ psi}$$

Note: The burst pressure is higher than one would expect from the factor 0.9 applied to the ultimate tensile strength for the vessel wall.

This is an inherent characteristic of the stable pressure vessel and results from the decreasing radius of curvature of the vessel wall when Θ increases.

1.6.1 Weights

The weight of the stable vessel can now be calculated with the previously developed formula (ends not included).

$$\begin{aligned}W_{\text{tot}} &= \frac{\rho Pr^2 L \Theta}{\sigma \sin^2 \Theta} \left[12\sqrt{2} \sin(\Theta - 45) + \frac{8\sqrt{2} \Theta}{1.8 \pi \sin \Theta} \right] \\&= \frac{0.1595 \times 2000 \times 12^2 \times 12 \times 0.93098}{165,000 \sin^2 53.341^\circ} \\&\quad \left[12\sqrt{2} \sin(53.341 - 45) + \frac{8\sqrt{2} \times 0.93098}{0.9 \pi \sin 53.341} \right] \\&= 4.833 \left[2.462 + 4.644 \right] = \underline{34.4} \text{ lbm/ft length}\end{aligned}$$

A conventional vessel in comparison will have the following weight:

$$\begin{aligned}W_{\text{conv}} &= \rho \pi D t L = \rho \pi D \frac{PR}{\sigma/3} L \\&= 0.1595 \times \pi \times 12 \times 2 \frac{2000 \times 12}{165,000/3} \times 12 = 63.0 \text{ lbm/ft}\end{aligned}$$

1.6.2 Volumes

The volume of the stable vessel is calculated with the previously developed formula (ends not included).

$$\begin{aligned}V_{\text{tot}} &= r^2 L \left[2 + \frac{2 \Theta}{\sin^2 \Theta} - \frac{2}{\tan \Theta} - 4 \frac{t_{\text{TP}}}{r} \right] \\&= 12^2 \times 12 \left[2 + \frac{2 \times 0.93098}{\sin^2 53.341} - \frac{2}{\tan 53.341} - 4 \frac{0.130}{12} \right] \\&= 1728 \times \left[2 + 2.893354 - 1.488529 - 0.0433333 \right] \\&= 1728 \times 3.3615 \text{ in}^3 = 3.3615 \text{ ft}^3\end{aligned}$$

A conventional vessel in comparison will have the following volume:

$$V_{\text{conv}} = \frac{\pi}{4} D^2 L = \pi r^2 L = 3.1416 \text{ ft}^3$$

1.6.3 Gas Storage Capacity

Assume that air is stored at 2000 psi and 300°K. The gas density, ρ , is:

$$\rho = \frac{P}{RT} = \frac{2000 \times 144}{53.4 \times 300 \times 1.8} = 9.9875 \frac{\text{lbm}}{\text{ft}^3}$$

The weight of the gas stored in the stable vessel is:

$$\rho V_{\text{tot}} = 9.9875 \times 3.3615 = 33.5730 \text{ lbm}$$

The gas storage capacity is:

$$\frac{\rho V_{\text{tot}}}{W_{\text{tot}}} = \frac{33.573}{34.4} = 0.976 \frac{\text{lb}_{\text{gas}}}{\text{lb}_{\text{tank}}}$$

For the conventional vessel it is:

$$\frac{\rho V_{\text{conv}}}{W_{\text{tot}}} = \frac{9.9875 \times 3.1416}{63.0} = \frac{31.3767}{63.0} = 0.498 \frac{\text{lb}_{\text{gas}}}{\text{lb}_{\text{tank}}}$$

1.6.4 Coefficient of Performance

The coefficient of performance (COP) of the stable vessel compared with the conventional vessel can be written as:

$$\text{COP} = \frac{V_{\text{tot}}}{V_{\text{conv}}} \frac{W_{\text{conv}}}{W_{\text{tot}}} = \left(\frac{3.3615}{3.1416} \right) \left(\frac{63.0}{34.4} \right) = 1.96$$

1.65 System Weight Multiplier

The multiplier for the stable vessel is:

$$M = \frac{\rho V_{\text{tot}} + W_{\text{tot}}}{\rho V_{\text{tot}}} = \frac{33.573 + 34.4}{33.573} = 2.02$$

For conventional pressure vessels:

$$M = \frac{31.3767 + 63}{31.3767} = 3.01$$

These numbers are optimistic, because they do not include contributions by the vessel ends, ports, pads, reinforcements, flanges and bolts.

2.0 OTHER CONFIGURATIONS

A spherical stable vessel can be constructed along the above guidelines, using tie-plates or tie-rods to provide stable anchor points. The end terminations of a cylindrical vessel will consist of half of a stable spherical vessel.

3.0 OTHER MATERIALS

Glass filament wound tanks have pressure vessel performance factors, $\frac{PV}{W}$, that are almost twice that for titanium 6 Al-4V. Low cycle fatigue appears to limit the usefulness of the filament wound tanks, however. It is hoped that the above construction approach will extend the useful range of the wound tanks.

ATE
LME